UNIVERSITY OF CALIFORNIA,
IRVINE

Accessible Fabrication Technique Leveraging Flow-Defined Heterogeneity for 3D Biomaterial Architectures

DISSERTATION

submitted in partial satisfaction of the requirements
for the degree of

DOCTOR OF PHILOSOPHY

in Biomedical Engineering

by

Alberto Ranier Escobar

Dissertation Committee:
Assistant Professor Peter Tseng, Chair
Professor Abraham Lee
Professor Michelle Khine

2024

DEDICATION

To branching paths & infinite possibilities

TABLE OF CONTENTS

LIST OF FIGURES

CHAPTER 3

ACKNOWLEDGEMENTS

To my wife, my parents, my siblings, and grandparents, from the bottom of my heart, I thank you for your love, your support, your guidance, and your patience. I am who I am and who I have become because of you.

To Dr. Peter Tseng, thank you for taking me in as one of the first members of your group. The experience of learning from you and alongside you as we both took steps towards new stages in life was invaluable. To the members of the Tseng Research Group, past and present, I hope our paths cross again someday. You have all deeply shaped my experience over the last seven years.

To my dissertation committee members, Dr. Abraham Lee and Dr. Michelle Khine, I thank you for sharing your experience and your wisdom. I would also like to thank Dr. William Tang and Dr. Lorenzo Valdevit for your direction and insight.

To Beth Harnick-Shapiro, thank you for teaching me, guiding me, and stopping me, with your candor and insight, when I would find myself spinning in place with no progress in sight. To Oladunni Adeyiga, thank you for molding my foundations as a researcher and helping me find my place in this field. To Neil Sahota, thank you for broadening my perspective and sharing your stories.

Portions of Chapters 1 and 2 of this dissertation are an adaptation of the material as it appears in "Fluidic infiltrative assembly of 3D hydrogel with heterogeneous composition and function" in Advanced Functional Materials, used with permission from Wiley-VCH GmbH. The coauthors listed in this publication are Somayeh Zanganeh, Jonathan Sullivan, Lei Li, Manik Dautta, Jaeho Lee, and Peter Tseng. Peter Tseng directed and supervised research which forms the basis for the dissertation.

Portions of Chapters 3 of this dissertation are an adaptation of the material as it appears in "Mechanically-directed assembly of nanostructured biopolymer with tunable anisotropy, hierarchy, and functionality" in Next Materials, used with permission from Elsevier Ltd (CC BY-NC-ND). The coauthors listed in this publication are Lei Li, Somayeh Zanganeh, Manik Dautta, M Mahmudul Hasan Sajeeb, Fan Ye, Jens Thomas Escobar, and Peter Tseng. Peter Tseng directed and supervised research which forms the basis for the dissertation.

VITA

Alberto Ranier Escobar

EDUCATION

Doctor of Philosophy (PhD) in Biomedical Engineering **2024**
University of California, Irvine *Irvine, California*

Master of Science (MS) in Biomedical Engineering **2021**
University of California, Irvine *Irvine, California*

Bachelor of Science (BS) in Bioengineering **2016**
University of California, Los Angeles *Los Angeles, California*

EXPERIENCE

Graduate Student Researcher **9/2017 – 6/2024**
University of California, Irvine Irvine, California

Teaching Assistant **9/2018 – 6/2024**
University of California, Irvine Irvine, California

In-Home Support Service Provider **12/2013 – 3/2021**
California Department of Social Services Los Angeles, California

Staff Research Associate I **1/2017 – 8/2017**
University of California, Los Angeles Los Angeles, California

Undergraduate Student Researcher **10/2015 – 12/2016**
University of California, Los Angeles Los Angeles, California

PUBLICATIONS

1. L. Li*, **A. R. Escobar***, S. Zanganeh, M. Dautta, M. M. H. Sajeeb, F. Ye, J. T. Escobar, P. Tseng, "Mechanically-directed assembly of nanostructured biopolymer with tunable anisotropy, hierarchy, and functionality," Next Materials, vol. 2, p. 100140, Jan. 2024. doi:10.1016/j.nxmate.2024.100140 (*These authors contributed equally to the work)
2. A. Hajiaghajani, P. Rwei, A. H. A. Zargari, **A. R. Escobar**, F. Kurdahi, M. Khine, P. Tseng, "Amphibious epidermal area networks for uninterrupted wireless data and Power

Transfer," Nature Communications, vol. 14, no. 1, Nov. 2023. doi:10.1038/s41467-023-43344-6

3. H. Qin, A. Hajiaghajani, **A. R. Escobar**, A. H. A. Zargari, F. Kuradhi, P. Tseng, "Laser-induced graphene-based smart textiles for wireless cross-body metrics," ACS Applied Nano Materials, vol. 6, no. 20, pp. 19158–19167, Oct. 2023. doi:10.1021/acsanm.3c03582
4. K. K. H. Dia, A. Hajiaghajani, **A. R. Escobar**, M. Dautta, P. Tseng, "Broadside-coupled split ring resonators as a model construct for passive wireless sensing," Advanced Sensor Research, vol. 2, no. 10, Apr. 2023. doi:10.1002/adsr.202300006
5. M. Dautta, A. Hajiaghajani, F. Ye, **A. R. Escobar**, A. Jimenez, K. K. H. Dia, P. Tseng, "Programmable multiwavelength radio frequency spectrometry of chemophysical environments through an adaptable network of flexible and environmentally responsive, passive wireless elements," Small Science, vol. 2, no. 6, Mar. 2022. doi:10.1002/smsc.202200013
6. M. Dautta, K. K. H. Dia, A. Hajiaghajani, **A. R. Escobar**, M. Alshetaiwi, P. Tseng, "Multiscale, nano- to Mesostructural Engineering of silk biopolymer-interlayer biosensors for continuous comonitoring of nutrients in food," Advanced Materials Technologies, vol. 7, no. 2, Aug. 2021. doi:10.1002/admt.202100666
7. **A. R. Escobar***, S. Zanganeh*, J. Sullivan, L. Li, M. Dautta, J. Lee, P. Tseng et al., "Fluidic infiltrative assembly of 3D hydrogel with heterogeneous composition and function," Advanced Functional Materials, vol. 31, no. 33, Jun. 2021. doi:10.1002/adfm.202103288 (*These authors contributed equally to the work)
8. O. B. Adeyiga, C. Murray, H. E. Muñoz, **A. Escobar**, D. Di Carlo, "Magnetic microparticle concentration and collection using a mechatronic magnetic ratcheting system," PLOS ONE, vol. 16, no. 2, Feb. 2021. doi:10.1371/journal.pone.0246124
9. L. Lin, M. Dautta, A. Hajiaghajani, **A. R. Escobar**, P. Tseng, M. Khine, "Paint-on Epidermal Electronics for on-demand sensors and Circuits," Advanced Electronic Materials, vol. 7, no. 1, Nov. 2020. doi:10.1002/aelm.202000765
10. M. Dautta, M. Alshetaiwi, **A. Escobar**, F. Torres, N. Bernardo, P. Tseng, "Multi-functional hydrogel-interlayer RF/NFC resonators as a versatile platform for passive and wireless biosensing," Advanced Electronic Materials, vol. 6, no. 4, Feb. 2020. doi:10.1002/aelm.201901311

11. A. Hajiaghajani, **A. R. Escobar**, M. Dautta, P. Tseng, “Selective manipulation and trapping of magnetically barcoded materials,” Advanced Materials Interfaces, vol. 6, no. 24, Nov. 2019. doi:10.1002/admi.201901312

ABSTRACT OF THE DISSERTATION

Accessible Fabrication Technique Leveraging Flow-Defined Heterogeneity for 3D Biomaterial Architectures

by

Alberto Ranier Escobar
Doctor of Philosophy in Biomedical Engineering
University of California, Irvine, 2024
Assistant Professor Peter Tseng, Chair

Regenerative medicine and tissue engineering leverage applied science and engineering approaches to provide solutions for restoring, replacing, and maintaining the function of impaired tissues and organs. In tissue engineering, tissue-like constructs are manufactured through the combination of cells, bioactive molecules, and biocompatible scaffolds to mimic natural tissues and restore tissue function. Designing an effective scaffold necessitates coordinated strategies that couple biomaterial selection with compatible fabrication techniques.

Current printability restrictions imposed on the pool of compatible biomaterials by advanced scaffold fabrication techniques potentially exclude ideal options for tissue-specific mimicry. The need for specialized fabrication equipment also serves as a “barrier to entry” in a field where a lack of sufficient funding is given as a common reason for failures in clinical translation. This dissertation presents the development of an accessible fabrication technique, leveraging coordinated injection molding strategies and indirect 3D printing, to produce 3D hydrogel constructs with programmable gradients in composition, architecture,

and function. Our approach, referred to as fluidic infiltrative assembly (FIA), capitalizes on the printability bypass of indirect 3D printing, flow-defined heterogeneity from coordinated injection molding strategies, and commercially-available equipment/products to facilitate ongoing efforts in tissue scaffold development. This work also discusses the integration of FIA with a post-processing technique for inducing structural anisotropy in biopolymer networks to generate multi-dimensional, anisotropic gradients in a programmable manner. Though subject to limitations imposed by sacrificial materials, this accessible and versatile technique offers an alternative, cost-effective platform for tissue-specific, scaffold development.

CHAPTER 1

Introduction

Regenerative medicine and tissue engineering leverage applied science and engineering approaches to provide solutions for restoring, replacing, and maintaining the function of impaired tissues and organs [1], [2]. Tissue engineering is a specific subset of regenerative medicine that focuses on tissue regeneration, replacement, or reconstruction through the fabrication and subsequent implantation of tissue-like constructs [2]. These constructs attempt to mimic natural tissues through the combination of cells, bioactive molecules, and biocompatible scaffolds [2], [3], [4], [5]. Together, these components form the tissue engineering "triad" and serve as the basis for the design of engineered tissues (Figure 1.1) [5], [6], [7].

There is intentional parity between the tissue engineering triad and the factors that determine a tissue's role in the body [8]. Tissues are broadly categorized by their morphology and function into four basic types: epithelial, muscle, nervous, and connective tissue [9]. These categories, while useful for simplifying tissue anatomy, do not comprehensively encompass all tissue types present within the body [9], [10], [11]. The structure and function of a tissue is dependent on its extracellular matrix (ECM) composition, cell type diversity, and the bioactive molecules present that facilitate cellular processes [12]. In the triad, biocompatible scaffolds host tissue-specific cell types and bioactive molecules

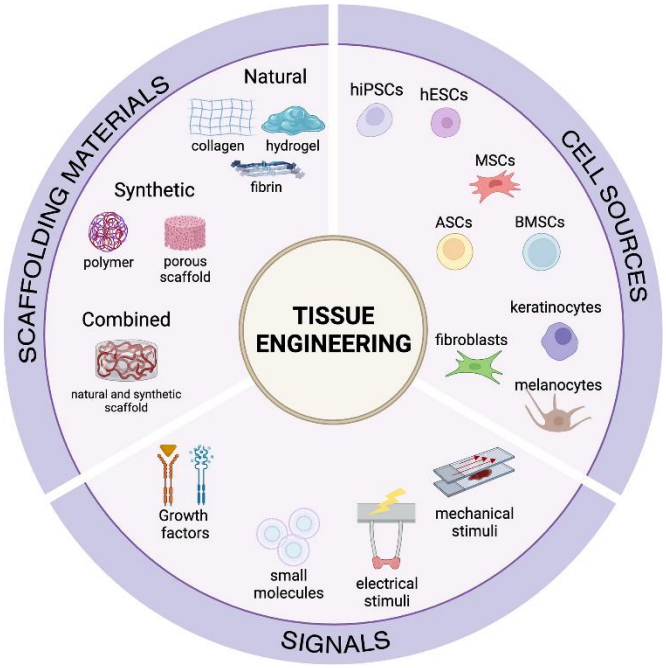

Figure 1.1 | The Tissue Engineering Triad. Schematic representation of the three components that compose the tissue engineering triad. Artificial tissue development must consider all three factors to function as an effective tissue mimic [7].

by serving as analogs to the ECM of a particular tissue and enabling equivalent tissue function [8].

The composition and structure of a scaffold determine the behavior of loaded cells which, in turn, enable tissue function. In tissues, cells regulate their behavior by communicating with their microenvironment via cell-to-cell contact, cell-to-ECM interactions, and paracrine signaling [13], [14], [15]. From a cellular perspective, the composition and structure of the local ECM controls their proximity to nearby cells, available sites for cell-to-ECM interaction, and the diffusion of signaling molecules. As ECM analogs, the material composition and architecture of tissue scaffolds determine available sites for cell interaction and access to those sites, respectively [16], [17].

Engineered tissue scaffolds need to satisfy fundamental and tissue-specific requirements to mimic the ECM and enable implantation, integration, and the restoration of tissue function [18]. Fundamentally, a scaffold should:

- Allow/improve cell attachment, proliferation and homing, differentiation, vascularization, diffusion, and waste removal
- Permit sufficient transport of gases, nutrients, and regulatory factors
- Avoid inciting an immune response

- Enable efficient and cost-effective manufacturing
- Allow for sterilization, easy handling in the operation theatre, and minimally-invasive implantation
- Facilitate host integration after implantation [6], [8], [18], [19]

Additional biological and mechanical requirements are dependent on the tissue of interest and could include characteristics such as high load-bearing capabilities or complex structural hierarchy as in the case of cartilage and bone [18], [19], [20]. Satisfaction of the above requirements necessitates scaffold design strategies that coordinate material selection with compatible fabrication techniques.

1.1 Biomaterials for Tissue Engineering

The materials employed in tissue scaffolds must be either bioinert, biocompatible, or bioactive [21], [22], [23]. Biomaterials are materials that can coexist and interact with physiological systems without inducing a significant immune response [24]. Almost all natural materials are biocomposites of polymeric networks that provide structure and ceramics that reinforce them [25]. The following sections will present common structural biomaterials employed in the fabrication of scaffolds for tissue engineering.

1.1.1 Polymers

All polymer scaffolds for tissue engineering are broadly classified as gels and become hydrogels under cell culture conditions. Gels are non-fluid polymer networks that are expanded throughout their volume by a fluid [26]. This definition includes both dry scaffolds (e.g. foams, sponges, aerogels) and wet scaffolds (e.g. hydrogels, alcogels, microgels)

irrespective of the method employed in their fabrication. Hydrogels are three-dimensional (3D) polymer networks of highly hydrophilic polymeric units, of natural and/or synthetic origin, expanded throughout their volume by water [26], [27], [28]. The ECM is considered a natural hydrogel expanded throughout its volume by interstitial fluid, a water-based biofluid similar in composition to blood [29], [30], [31]. Accordingly, all polymeric tissue scaffolds become hydrogels under cell culture conditions.

Polymers can be broadly classified as either biopolymeric or synthetic depending on their origin and production processes. There are conflicting uses of the term "biopolymer" in literature as it pertains to the classification of specific polymers [32], [33], [34]. For this dissertation, a biopolymer is defined as a natural or naturally-derived polymer produced via biological processes and readily obtained from living organisms. Natural biopolymers are proteins/polypeptides, polysaccharides, polynucleotides, and polyhydroxyalkanoates (PHAs) whereas naturally-derived biopolymers are natural biopolymers whose chemical backbone has undergone minor chemical modification to change its physiochemical properties [35], [36], [37]. Conversely, synthetic polymers refer to polymeric structures of organic or inorganic origin not included in the previous definition.

1.1.1.1 Biopolymers

Some of the most often used natural polymers in tissue scaffolds are commonly found in the animal ECM (Figure 1.2) [36]. Fundamentally, the ECM is a cell-derived network of biomaterials, comprised primarily of proteins and polysaccharides [38]. Collagen is a fibrous protein that constitutes approximately 30% of the ECM and is frequently incorporated into scaffolds due to their inherent biocompatibility, hydrophilicity, and flexibility [39], [40], [41].

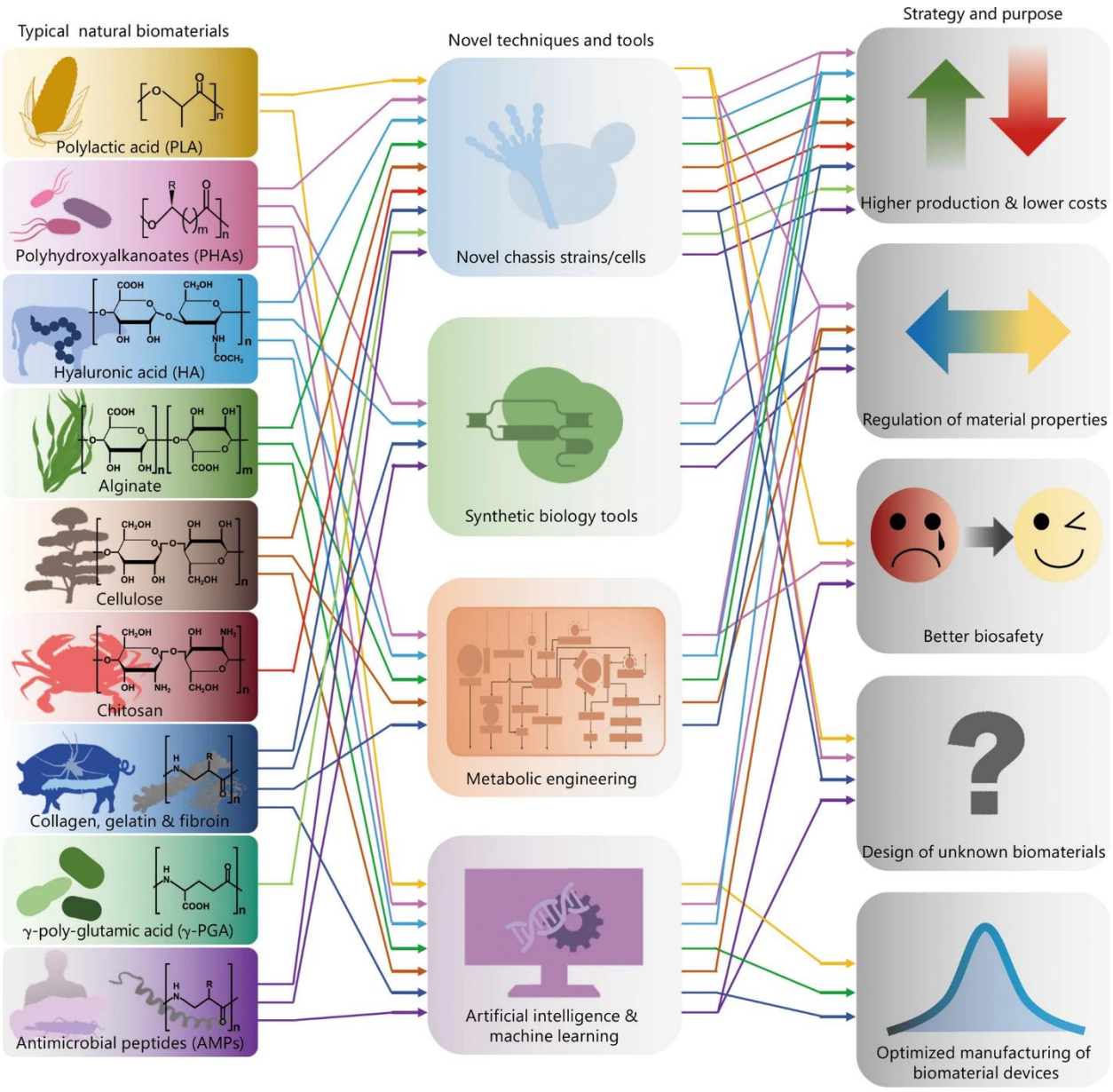

Figure 1.2 | Natural Biopolymers in Tissue Engineering. Correlational diagram of multiple strategies and purposes for biopolymers. The strategies presented allow would allow greater access and control to key tissue scaffold constituents [36].

Hyaluronic acid is an anionic glycosaminoglycan, a type of mucopolysaccharide commonly found alongside collagen in the connective tissues of the body, that helps support the structure of the ECM with excellent viscoelastic and hygroscopic properties [42], [43], [44].

Naturally-derived biopolymers can leverage their similarity to ECM components to function as constituents of tissue scaffolds. Among these, gelatin, silk fibroin, cellulose,

chitosan, and alginate are amongst the most used. Gelatin, a type I collagen derivative, is often used in scaffold designs as it retains many of collagen's advantages while being more readily available and cost-effective [45], [46], [47]. Silk fibroin is a protein-based biopolymer obtained from silk-producing arthropods boasting diverse processing options and tunable degradability [48], [49], [50]. Cellulose, the most abundant polysaccharide in nature, is a widely available and cost-effective biomaterial with high chemical modification potential whose various forms and derivatives provide numerous advantages to tissue scaffolds [32], [51], [52], [53], [54]. Chitin is the second most abundant natural polysaccharide and is readily obtained from the shells of crustaceans and cartilaginous fish tissues, but its poor solubility in almost all common solvents renders it incapable of directly acting as a structural component in scaffolds [33], [35]. Chitosan is a cationic, deacetylated derivative of chitin, classified as a mucopolysaccharide like hyaluronic acid, with improved solubility in common solvents, exceptional biocompatibility, and unique antibacterial properties [55], [56], [57]. Lastly, alginate is an anionic, mucopolysaccharide obtained from brown micro-algae that is readily available at low cost and exhibits multiple routes for chemical modification [58], [59], [60], [61].

1.1.1.2 Synthetic

Synthetic polymers are widely used in tissue engineering to compensate for common limitations associated with biopolymers [62]. Whereas biopolymers often exhibit poor mechanical strength and rapidly degrade *in vivo,* synthetic polymers have greater uniformity and tunability over their microstructure, degradation rate, and physicochemical properties [34], [62], [63]. They are also readily available, cost-effective biomaterial options that are

capable of being manufactured at a large scale [34]. Despite these advantages, many synthetic polymers lack the necessary sites for cell interaction that are critical for the success of a tissue scaffold [62], [64]. Effective scaffolds often incorporate both biopolymer and synthetic polymer constituents to compensate for their respective weaknesses. Commonly used synthetic polymers include members of the linear aliphatic polyester family for hard-tissue engineering (e.g. poly(lactic acid), poly(glycolic acid), poly(lactic-co-glycolic acid)) and poly(urethanes) for soft-tissue engineering [63].

1.1.2 Decellularized Extracellular Matrix

Decellularized ECM (dECM) can directly act as scaffolds for tissue engineering, offering exceptional biomimicry in exchange for control over their composition [65]. The direct use of autologous, allogeneic, or xenogeneic dECM scaffolds ensures that their constituents are biocompatible, bioactive, and bioresorbable as they had already been hosts to cells prior to decellularization [66], [67]. Lyophilized dECM can be further processed and reconstituted into bioinks, returning some control over scaffold composition and enabling the fabrication of custom architectures [65], [68], [69].

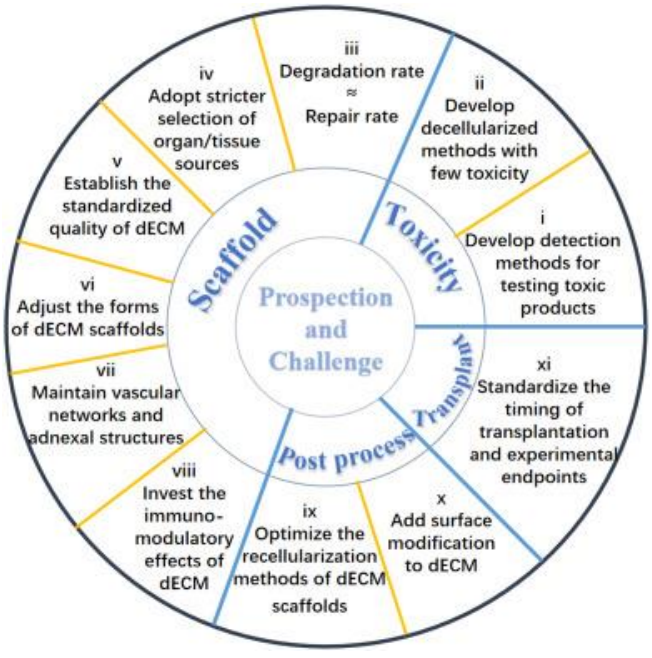

Figure 1.3 | Improving dECM Scaffolds. Graphic denoting various prospects and challenges associated with using dECM for tissue engineering. Despite these shortcomings, dECM scaffolds fulfill an important niche in artificial tissue development [67].

The removal of the ECM's native cellular components is critical to the use of the matrix as a scaffold as remaining components are likely to elicit an immune response after implantation [66]. Decellularization techniques attempt to completely remove cellular components without impairing the capabilities of the native ECM through physical, chemical, or enzymatic treatments [67]. These techniques can remove these components to a degree, but they inevitably damage the composition, structure, and properties of the ECM [66], [67]. Gentler decellularization techniques may preserve a greater percentage of ECM structure but may be unable to effectively remove enough cellular components to avoid inducing an immune response. Achieving equilibrium between ECM decellularization and its potential immunogenicity is critical to the success of dECM scaffolds in tissue engineering (Figure 1.3).

1.2 Scaffold Architecture and Fabrication Techniques

Scaffolds used in tissue engineering are typically 3D gels with highly interconnected pores tailored to the structural and functional needs of a tissue. Pore interconnectivity is a critical feature in tissue scaffolds as they allow cellular infiltration and facilitate nutrient exchange, waste removal, and gas transport [70], [71]. The average size of these pores is an essential parameter in scaffold design as the optimal pore size varies for different cell types and tissues [70], [71], [72]. For a given cell, larger pores equate to a decrease in the local surface area which can lead to disorganized cell attachment and a reduction in cell adhesion and migration speed. Conversely, smaller pore sizes may hinder cell migration and encourage the formation of a cell capsule around the scaffold, limiting nutrient/waste diffusion and leading to tissue necrosis [70]. Porosity and pore size are also inversely correlated with the

mechanical strength of a scaffold, highlighting the need to establish balance between the two parameters during fabrication [73].

Where scaffold porosity allows cellular access and infiltration, its surface chemistry and topography define how cells can interact with their microenvironment [70], [71]. Cell-scaffold interactions are mediated by specific cell surface receptors that recognize mucopolysaccharides and endogenous peptide sequences present in protein-based biopolymers and adsorbed proteins [74], [75], [76]. Protein-receptor recognition and protein adsorption are affected by the charge and hydrophilicity of a scaffold's constituents, the latter of which is further influenced by the surface roughness of the polymer network [70]. These properties can be customized by chemical modification (e.g. functionalization, plasma treatment) and/or conjugation with peptide-grafted ligands to induce cell attachment and scaffold colonization.

To restore or replace impaired tissues, scaffold design strategies must consider replicating gradients in composition, architecture, and, subsequently, physicochemical properties present within tissues and tissue interfaces (Figure 1.4) [77]. The ECM is a heterogeneous structure, hierarchically organized at the nano-, micro-, and macroscale, whose composition and architecture are unique for each tissue [29], [78], [79]. These tissue-specific variances regulate the distribution of bioactive molecules, drive spatially distinct cellular behavior, and facilitate tissue function [80]. Fabricating architectural gradients in scaffolds is a particularly challenging endeavor as it requires careful control over the porosity and anisotropy of biomaterial constituents over multiple length scales [20], [78], [81].

Polymeric biomaterials used in tissue scaffolds form complex nanoporous networks via physical and/or chemical crosslinking; however, these nanopores are significantly smaller

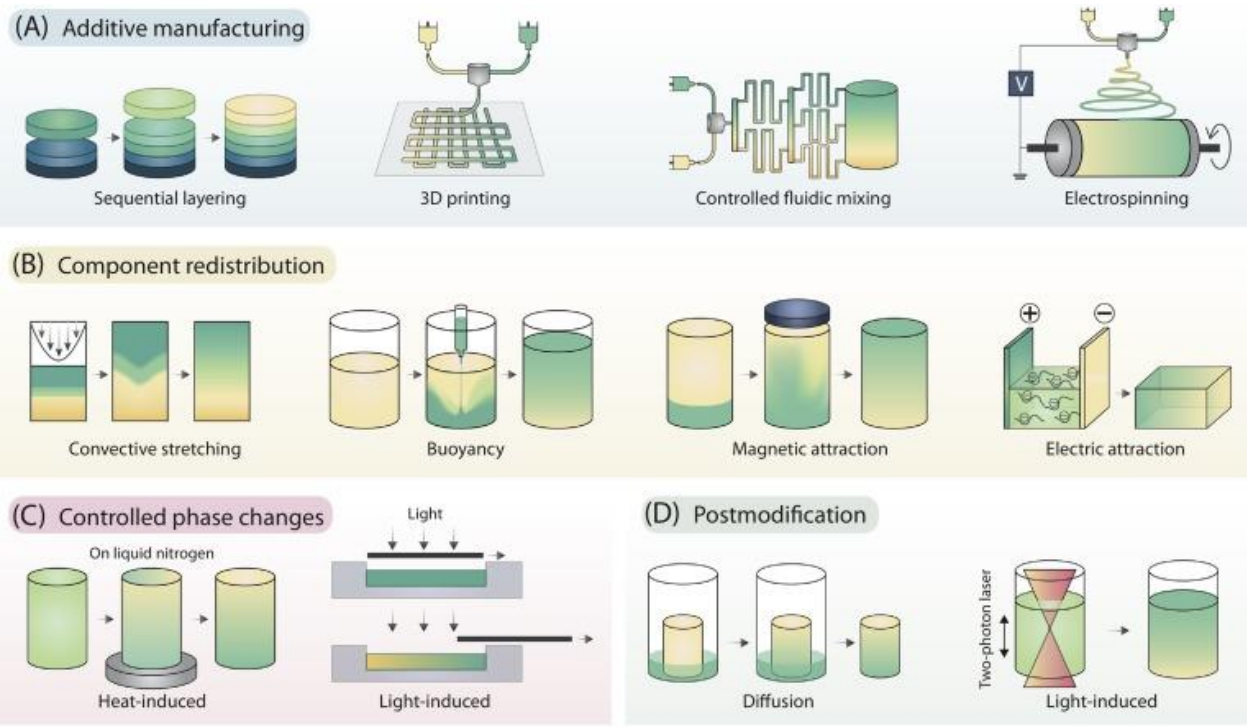

Figure 1.4 | Strategies for Fabricating Gradients. Achieving accurate biomimicry of natural tissues necessitates tissue scaffolds that have gradients in composition, architecture, and, subsequently, physicochemical properties [77].

than cells and do not allow cellular infiltration [70]. The following sections will present common fabrication techniques for porous scaffolds and comment on their ability to produce gradients in composition and/or architecture.

1.2.1 Porosity with Porogens

Conventional fabrication methods for porous scaffolds typically involve solvent casting or melting and the use of porogens to create pores with appropriate sizes and interconnectivity for cells and tissues of interest [82]. Porogens are sacrificial solid, liquid, or gaseous substances that generate pores and do not interfere with scaffold polymerization. Methods that employ solid porogens (e.g. salt, wax, gelatin microspheres) can be broadly classified under the term "particulate leaching" as they typically involve solidifying a

polymer/porogen mixture and subsequently leaching the porogen in an appropriate solvent [83], [84]. Thermally-induced phase separation refers to techniques where the temperature of a polymer solution, consisting of one or more solvents, is lowered below the freezing point of a particular solvent to induce phase separation and allow for solvent sublimation [84]. In these techniques, the sublimation of the frozen solvent creates a porous structure with good mechanical properties but irregular pores sizes [84], [85], [86]. Lastly, gas foaming creates gaseous bubbles within a polymer solution that, upon polymerization, leave behind defined pores with poor interconnectivity [83], [85]. These bubbles occur either when gas foaming agents in a polymer solution (e.g. effervescent salt) react with the surrounding solvent or when a high-to-low pressure change causes instability in dissolved gas, resulting in nucleation.

As non-interfering, sacrificial additives, porogens are suitable for integration with multi-material systems and can facilitate gradients in porosity; however, they often produce irregular or poorly interconnected pores and can leave behind toxic residues [77], [87]. Solvent casting is a simple fabrication method that allows for the concurrent polymerization of two or more biomaterials in miscible solvents [88]. Compositional gradients in these multi-material systems can be induced by exploiting physical differences between material constituents (e.g. density, size) or through externally applied fields on compatible biomaterials (e.g. electric, magnetic) [77]. Porosity gradients can also be created by the size-based redistribution of added porogens via centrifugal forces [89], [90]. Despite these advantages, conventional methods offer little control over the generated porosity and pore sizes due to poor porogen uniformity and variable dissolution mechanisms [87]. Additionally, certain porogens, particularly those employed in phase separation, exhibit

varying degrees of toxicity and can leave behind solvent residues that negatively impact cell viability [91].

1.2.2 Additive Manufacturing & 3D Printing

Whereas conventional methods are limited to solvent casting and melting for scaffold fabrication, additive manufacturing techniques fabricate porous structures, by design or by process, with great spatial control over structural constituents [92], [93]. Also known as 3D printing, these techniques refer to the layer-by-layer, additive process of creating 3D structures [94]. Pre-defined control at each layer allows for custom pore generation and architectural gradients that enable greater mimicry of a tissue's structure [92]. This control can be further enhanced by leveraging the inherent properties of biomaterial constituents; however, biomaterials available for printing are limited by their polymerization mechanisms and compatible 3D printing methods.

Broadly classified by their working principle (e.g. extrusion, drop-casting, photopolymerization) each 3D printing method presents distinct advantages and unique printability challenges for tissue scaffold fabrication [95], [96], [97], [98], [99]. Extrusion-based printing (EBP) methods are amongst the most used as they offer great printing speed, facilitate scalability, and can create tissue-like porous structures, but they offer limited resolution and necessitate the use of quick-polymerizing, shear-thinning solutions [100], [101], [102], [103], [104]. Droplet-based printing (DBP) offers greater resolution than EBP and can generate soft structures with locally controlled heterogeneity at the expense of mechanical strength and built-in porosity [105]. Power bed fusion (PBF) processes create complex, porous geometries without the need for additional support structures or porogens,

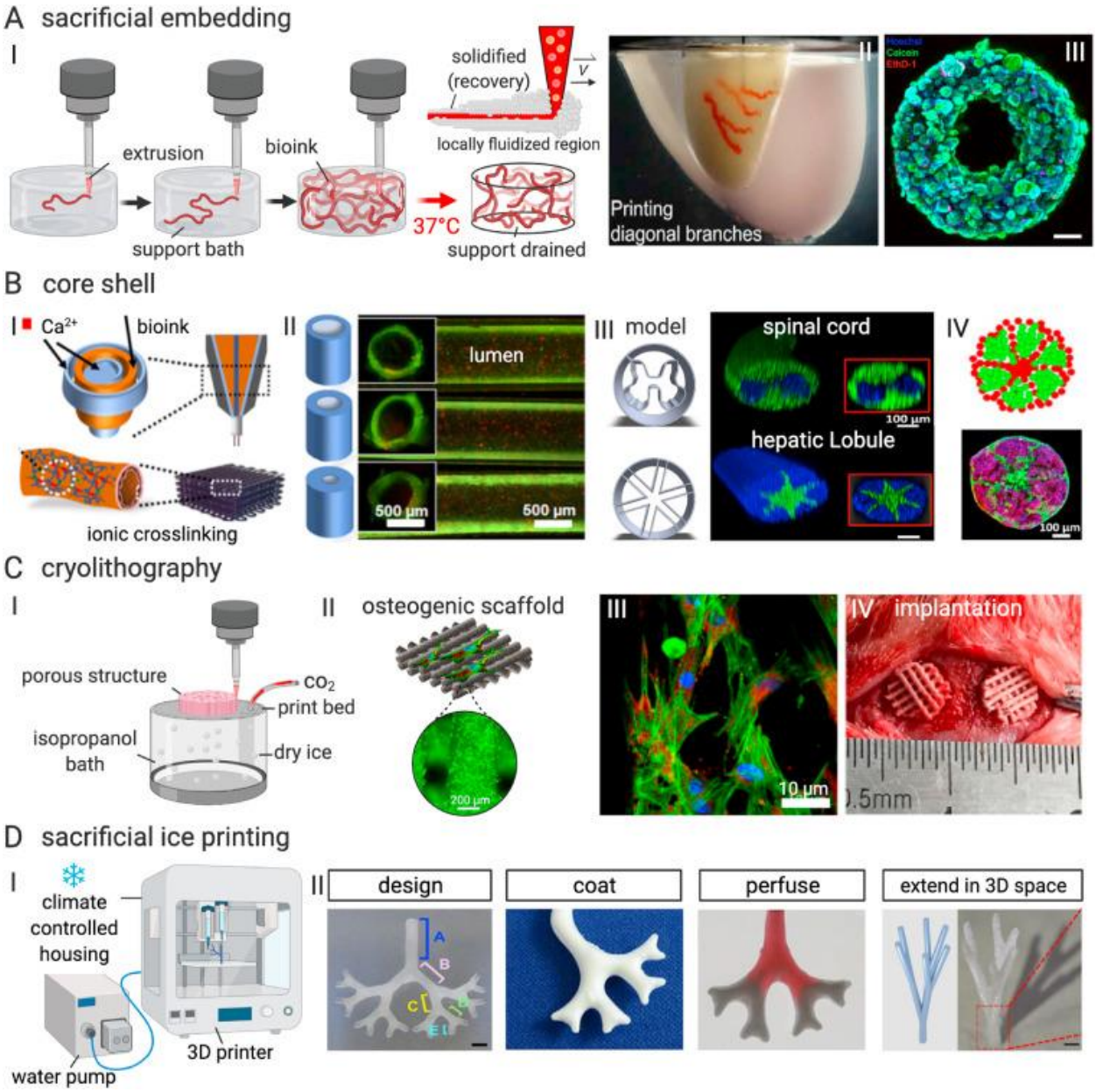

Figure 1.5 | 3D Heterogeneous Tissues via Multimodal Extrusion Bioprinting. Several advanced additive manufacturing techniques are modified or augmented forms of extrusion-based printing. Cells are common additions to these platforms and form "bioinks" for direct 3D printing of cell-laden scaffolds [93].

but their working principle (sintering/melting) significantly limits the availability of compatible biomaterials [83], [106], [107]. Light-based printing (LBP) offers the greatest resolution of the four method classifications and can create porous constructs like EBP, but resin constituents must have quick cure times, low viscosities, and must be directly photopolymerizable [108], [109], [110], [111], [112].

Multimodal, 3D printing systems allow for greater scaffold complexity and enable gradients in composition and architecture, but they also compound printability restrictions and limit tissue studies by increasing fabrication complexity [77]. These systems are classified as advanced 3D printing technologies and leverage multiple working principles to fabricate multi-material scaffolds with high resolution features [113]. EBP methods commonly serve as the basis for these systems as they are easy to scale, have less restrictive printability requirements, and are naturally compatible with other printing methods (Figure 1.5) [81], [93], [114]. DBP methods are easy to integrate into multimodal, EBP systems because their core working principles are identical, albeit with different mechanisms of material ejection, discrete drop-casting and continuous extrusion, respectively [115]. In particular, the continuous extrusion of a polymer solution through a nozzle induces shear stress that can align solubilized polymers and other biomaterials in the direction of stress and result in structural anisotropy, adding another layer to the structural hierarchy of a scaffold [77]. The combination of these modalities increases the likelihood of accurate tissue mimicry; however, they necessitate the use of specialized or custom equipment that may reduce access to these technologies and limit tissue studies necessary for clinical translation [116].

Indirect 3D printing is an alternative to direct 3D printing methods that eliminates the need to consider biomaterial printability in exchange for reduced control over the internal architectures [99], [116], [117], [118], [119], [120], [121]. 3D printed, sacrificial structures impart high resolution features on cast materials while retaining the ability to print with negative space [117], [118], [120], [122]. For scaffolds with complex internal structures, internal sacrificial features can be integrated into mold templates and subsequently

dissolved after biomaterial polymerization [116], [119]. This alternative method benefits from continual improvements in 3D printing technologies and bypasses a key limitation in tissue scaffold fabrication; however, additional research is needed regarding the biocompatibility and dissolution of available sacrificial materials [122].

1.3 Motivation & Scope of Dissertation

Current printability restrictions imposed on the pool of compatible biomaterials by advanced scaffold fabrication techniques potentially exclude ideal options for tissue-specific mimicry [123], [124]. The need for specialized fabrication equipment also serves as a "barrier to entry" in a field where a lack of sufficient funding is given as a common reason for failures in clinical translation [125], [126]. Indirect 3D printing is a viable alternative that bypasses printability restrictions and enables broader investigation into available scaffold formulations and tissue engineering strategies [123], [127], [128].

This dissertation presents the development of an accessible fabrication technique, leveraging coordinated injection molding strategies and indirect 3D printing, to produce 3D hydrogel constructs with defined gradients in composition and architecture. Briefly, commercially-available, stereolithography (SLA) 3D printers are used to print high-resolution, sacrificial molds from purchasable resin products. Solutions of natural, synthetic, and/or "smart" polymer constituents can be injected into molds as a homogenous solution for solvent casting or in a programmable manner to induce flow-defined heterogeneity with multiple material constituents. After gelation, an optional post processing step can be performed on hydrogels capable of additional, *in situ* polymerization that induces nanoscale, anisotropic gradients, defined by the mold architecture, that remain intact after mold

dissolution. Our approach, referred to as fluidic infiltrative assembly (FIA), capitalizes on the printability bypass of indirect 3D printing, flow-defined heterogeneity from coordinated injection molding strategies, and commercially-available equipment/products to facilitate ongoing efforts in tissue scaffold development.

The content structure of this dissertation is as follows. Chapter 1 has provided an overview of tissue engineering, with particular emphasis on tissue scaffold fabrication, and defined the motivation and scope for this dissertation. Chapter 2 will provide a detailed description of FIA, characterization of possible flow schemes for compositional and architectural gradients, and showcase multi-functional, multi-material hydrogel constructs. Chapter 3 will briefly describe structural gradients in natural tissues, summarize methods for inducing them *in vitro*, and report on extensions made to a post-processing method for inducing programmable, multi-directional anisotropy leveraging 3D printing and FIA. Chapter 4 will conclude this work by outlining current limitations of this technique, routes for possible improvement, and potential uses in multidisciplinary context.

Chapter 2

Fluidic Infiltrative Assembly of 3D Hydrogel with Heterogeneous Composition and Function

3D hydrogels have garnered significant attention across a variety of engineering disciplines for their potential applications in next-generation systems [95], [96], [129], [130], [131], [132], [133], [134], [135], [136]. The built-in hydrophilicity of hydrogels often imparts biocompatibility and sometimes biomimicry which, when coupled with tunable mechanical properties, make them prime material candidates for emerging systems in tissue engineering, soft robotics, or biosensing [97], [137], [138], [139]. There is tremendous diversity to the structure of hydrogels and their constituent components, which may be crosslinked through chemical or physical strategies, potentially including biomolecules and/or nanomaterials [27], [133], [140], [141], [142], [143]. Tunable control over the gelation and constituents of such gels enables these materials to have a large degree of programmability in behavior; such mutability lends a material versatility that is unseen in other biocompatible materials [27], [28], [95], [98], [132], [133], [144].

In alignment with their material diversity, many potential methods have been developed to print (or pattern) hydrogel, but no universally accessible technique exists that can be adapted/applied to machine a broad spectrum of existing hydrogels and modifiers in 3D. In addition, to date few of these strategies have demonstrated the robust capability to produce complex, free-standing, multi-material constructs that possess desired heterogeneity for next generation hydrogel structures/systems [109]. Indirect 3D printing

strategies can potentially address this limitation as they are compatible with a wide range of hydrogels that are gelled *in situ* which encompasses a large percentage of existing hydrogel synthesis protocols [110].

Here, we combine indirect 3D printing and coordinating injection molding strategies to create 3D hydrogels and bypass the printability constraints on material selection associated with direct 3D printing strategies [121], [137], [145], [146]. Sacrificial fluidic molds were 3D printed at micro-scale resolution with thin channel sidewalls (≈ 250 μm) using a commercially-available, SLA 3D printer and purchasable resin. Through defined inlets/outlets, these molds were filled with a selection of natural, synthetic, and/or "smart" hydrogel precursor solutions while being modified with large concentrations of nanomaterials or biomolecules. After complete gelation (via standard chemical or physical crosslinking techniques), the sacrificial molds were degraded in fluoroalcohol solution: this releases the hydrogel with minimal to no change in studied physical behaviors (as studied later). The SLA-enabled, high-resolution/thin-walled fluidic channels distinguish our approach from other sacrificial techniques, whose low-resolution molds are typically simply backfilled with hydrogel prepolymer. Furthermore, it allows for the direct fabrication of delicate fluidic inlets and channels that sculpt the hydrogel and readily degrade without harming its structure.

Programmable control over the infiltration of the hydrogel precursor solutions into various inlets allowed for the creation of multi-material, multi-functional hydrogels with flow-defined heterogeneity. This approach allows for a versatility that is typically inaccessible to direct printing: 1) printing process is highly accessible and achieved using commercially available 3D SLA printer and resin; 2) both basic and interpenetrating

networks of synthetic and biologically-derived polymers can be readily synthesized (crosslinked via either chemical or physical means); 3) allows generally unconstrained modification with nanomaterials and biomolecules; 4) enables facile generation of heterogeneous material with tunable gradients; and 5) unique architectures can be synthesized, driven via the engineering of fluidic operations in the 3D shell (particle sorting, mixing, and sheath flow demonstrated herein). The hydrogel structuring/gelation and primary sacrificial processes are both rapid and can potentially be completed within minutes. As proof of concept, we demonstrate a variety of complex, 3D multi-material hydrogel systems with programmable functions (motion/mechanics, temperature/light interactivity, gradient behavior) in 3D. We anticipate this strategy to be readily adaptable to a large variety of existing hydrogel formulations without additional engineering. Specifically, the prepolymer no longer needs to be adapted to the 3D printing technique; the polymer simply needs to be able to be capable of in-situ gelation and remain functional under short exposure to solvent (which many hydrogels are capable of), thus enabling a diverse set of protocols from existing literature.

2.1 Materials & Methods

The following sections list the materials and experimental methods used to conduct the research described in Sections 2.2 – 2.5.

2.1.1 Materials

Acrylamide (AAm), n-isopropylacrylamide (NIPAAm), methylene bisacrylamide (MBAAm), ammonium persulfate (APS), N,N,N',N'-tetramethylethylenediamine (TEMED), calcium carbonate ($CaCO_3$), D-(+)-gluconic acid δ-lactone (GDL), fluorescein o-acrylate (FOA), trisodium citrate dihydrate, gold (III) chloride trihydrate (HAuCl4), sodium chloride (NaCl), dimethyl sulfoxide (DMSO), and iron (III) chloride hexahydrate ($FeCl_3$) were purchased from Millipore Sigma. Isopropanol (IPA) and acetone (ACE) were purchased from Fisher Scientific. Sodium alginate (Na-ALG, viscosity 80 – 120 cp) was purchased from FUJIFILM Wako Pure Chemical Corporation, 1,1,1,3,3,3-hexafluoro-2-propanol (HFIP) from Matrix Scientific, rhodamine methacrylate (RHO) from Polysciences, Inc., ethanol (EtOH) from Gold Shield Distributors, and 3DM-ABS resin from 3DM Inc. All chemicals were purchased and used without further purification. All aqueous solutions were prepared using deionized water (DI) unless otherwise stated.

2.1.2 Methods

<u>Three-Dimensional (3D) Printing and Post-Processing</u>

3D Computer Aided Design (CAD) models of a fluidic mold were made in SolidWorks® (Dassault Systèmes) and output as a standard tessellation file (STL). Support structures were added manually in Meshmixer (Autodesk) to avoid auto-generating supports within the mold itself. The modified STL was oriented and duplicated in Autodesk Netfabb (Autodesk) with the build volume of the program matching the build volume of the 3D printer. The file was uploaded, sliced, and printed in a liquid crystal display stereolithography (LCD-SLA) 3D printer (Phrozen) with an XY-resolution of 47 μm and a user-defined Z-resolution.

After printing, the molds were removed from the build platform and placed in an IPA bath for 15 minutes. Resin remaining in the molds were removed by vigorous shaking in paper towels or forcing the resin out with an air gun. Molds with resin cured in the internal area were discarded. The molds were placed in a UV-curing box (Spierce Technologies) for 15 minutes, after which they were ready to use.

Preparation of Hydrogel Stock Solutions

Stock solutions of the hydrogel monomers were made in DI and stored at 4 °C until needed. *PAAm precursor*: 20% (w/w) AAm (10.16 g), 6% (w/w) MBAAm relative to AAm (0.6 g), 40 mL DI. *PNIPAAm precursor*: 20% (w/v) NIPAAm (8 g), 0.7% (w/v) MBAAm (0.28 g), 40 mL DI. ALG precursor: X% (w/v) Na-ALG, 40 mL DI. X refers to a value between 0.5 and 1.5 as these percentages were used. *PAAm-ALG precursor:* 15% (w/w) AAm (4.514 g), 1.875 % (w/w) Na-ALG (0.564 g), 0.35% (w/w) MBAAm relative to AAm (0.0158 g), 25 mL DI. Solutions containing Na-ALG were sonicated until the powders were completely dissolved.

Hydrogel Synthesis

PAAm Hydrogels: 10% (w/w) PAAm hydrogel: PAAm stock (500 µL), DI (470 µL), and TEMED (5 µL) were added to a microcentrifuge tube and mixed. 10% APS (25 µL) was added and quickly mixed into the solution via tube inversion. *10% (w/w) PAAm-co-FOA hydrogel*: PAAm stock (500 µL), DI (465 µL), TEMED (5 µL), and FOA solution (5 µL, 100 mg/mL in DMSO) were added to a microcentrifuge tube and mixed. 10% APS (25 µL) was added and quickly mixed into the solution via tube inversion. *10% (w/w) PAAm-co-RHO hydrogel*: PAAm stock (500 µL), DI (445 µL), TEMED (5 µL), DMSO (5 µL), and RHO solution (20 µL, 100 mg/mL in

DI) were added to a microcentrifuge tube and mixed. 10% APS (25 µL) was added and quickly mixed into the solution via tube inversion.

For a 10% (w/v) PNIPAAm hydrogel: PNIPAAm stock (500 µL), DI (455 µL), and TEMED (5 µL) were added to a microcentrifuge tube and mixed. 10% APS (40 µL) was added and quickly mixed into the solution via tube inversion. At room temperature, these volumes of TEMED and APS yield an initial gel within five minutes and were used upon mixing.

For a 1.5% (w/v) Ca-ALG hydrogel: Na-ALG stock (1 mL) was added to a microcentrifuge tube. To the tube, $CaCO_3$ (0.0045 g, 45 mM final concentration) and GDL (0.016 g, 90 mM final concentration) were added sequentially, mixing vigorously after each addition. The solution was used immediately upon mixing. At room temperature, these amounts of $CaCO_3$ and GDL take 24 hours to form a complete gel, but the viscosity of the solution begins to increase rapidly within 10 minutes as the initial gel begins to form.

For a 12.9% (w/w) PAAm/1.6% (w/w) ALG PAAm-co-Ca-ALG hydrogel: PAAm-ALG stock (2.58 mL), DI (282 µL), 50% glycerol (60 µL), and TEMED (0.3 µL) were added to a microcentrifuge tube and mixed by tube inversion. To the tube, $CaCO_3$ (0.0039 g) and GDL (0.0138 g) were added sequentially to initiate, mixing vigorously after each addition. Working quickly, 10% APS (75 µL) was added to the solution and mixed via tube inversion. The solution was used immediately.

For 13% (w/v) PNIPAAm/1% PAAm (w/v) PNIPAAm-co-PAAm hydrogel: PNIPAAm stock (650 µL), PAAm stock (50 µL), 50% glycerol (50 µL), ethanol (50 µL), DI (145 µL), and TEMED (5 µL) were added to a microcentrifuge tube and mixed. 10% APS (50 µL) was added and quickly mixed into the solution via tube inversion. At room temperature, these volumes of TEMED and APS yield an initial gel within five minutes and were used upon mixing.

All hydrogel solutions prior to gelation are referred to as precursor solutions.

Gold Nanoparticle (GNP) Synthesis

Gold nanoparticles were synthesized following an established protocol. Briefly, HAuCl4 (20 mL, 1.0 mM) was brought to a rolling boil in a flask on a stirring hot plate. To the rapidly stirred boiling solution, trisodium citrate dihydrate (2 mL, 1% in DI) was added to initiate nanoparticle formation through the reduction of the gold (III) in solution. Once the solution turned a deep red, it was removed from the hot plate and allowed to cool. An approximation of the GNP concentration was made by measuring the difference between an empty weighing boat and the weighing boat with an air-dried aliquot of the GNP solution then dividing by the volume of the aliquot.

Mold Preparation, Infiltration, and Degradation

UV-cured molds were filled with 100% EtOH followed by DI and a 10% Tween 20 (BioRad) solution. The molds were left with the Tween 20 solution for a minimum of one hour before being rinsed with DI and used immediately.

Prepped molds were filled with the hydrogel precursor solution of choice and allowed to gel completely before transferring into DI for 24 hours. The gel-containing molds were transferred to a conical tube with DI and placed in a heated water bath (PAAm/ALG/PAAm-ALG: 70 °C; PNIPAAm: 50 °C). A conical tube of an HFIP solution was also placed in the water bath to warm prior to degradation (PAAm/ALG/PAAm-ALG: 50% HFIP diluted with DI; PNIPAAm: 100% HFIP). Once heated, a mold was transferred to separate conical the along with enough HFIP solution to cover. Mold degradation was carefully supervised until the gel was mostly released as the degradation time varied depending on mold complexity. The tube was removed from the water bath and the HFIP solution was replaced with DI a minimum of three times to remove the gels from the HFIP environment and to remove remaining mold pieces. Over the course of 24 hours, the DI in the tube was exchanged with clean DI minimum of three times to leech any remaining HFIP from the solution. After 24 hours, the 3D gel was ready to use.

Print Resolution and Hydrogel Fidelity

Two-and-a-half dimensional (2.5D) molds with cubic indentations of variable side length were made to test the accuracy of the 3D printer against the intended CAD design and the fidelity of PAAm hydrogels against the printed mold. The indentation side lengths varied between 200 μm and 1000 μm at 200 μm intervals. To better visualize the print resolution and hydrogel fidelity, a 3D, sacrificial, “donut” mold, designed to produce 16 equally spaced, circular ridges on the gel donut’s surface, was printed. The ridges were 500 μm in width and were 22.5° apart.

Gel Functionality After Solvent Treatment

PAAm, PNIPAAm, and Ca-ALG gels were qualitatively gauged for retained functionality (mechanical strength, thermosensitivity, secondary crosslinking respectively) following degradation and DI equilibration.

PAAm hydrogel: A square pyramid-like, tubular mold was filled with PAAm precursor, allowed to gel and equilibrate in DI, and was degraded according to the PAAm-specific, mold degradation protocol. The resulting gel was equilibrated in DI before being pressed with a finger.

PNIPAAm hydrogel: A cube-like, tubular mold was filled with PNIPAAm precursor, allowed to gel and equilibrate in DI, and was degraded according to the PNIPAAm-specific, mold degradation protocol. The resulting gel was equilibrated in DI before being heated past the lower critical solution temperature (LCST) of PNIPAAm in a water bath.

Ca-ALG hydrogel: A sphere-like, tubular mold was filled with ALG precursor, allowed to gel and equilibrate in DI, and was degraded according to the ALG-specific, mold degradation protocol. The resulting gel was equilibrated in DI before undergoing secondary crosslinking by a multivalent cation (Fe^{3+}) of a higher alginic affinity than Ca^{2+}.

Fluidic Operations in 2.5D

A simple 2.5D, Y-shaped mold was made to characterize different methods of mold infiltration and their resulting hydrogels using the technique.

Co-flow: PAAm-co-FOA precursor and PAAm-co-RHO precursor solutions were simultaneously infiltrated into the mold at equivalent flow rates and gelled completely after the flows inside the mold stabilized.

Sequential: PAAm-co-FOA precursor was infiltrated into one inlet of the mold at a defined flow rate until the mold was filled with solution. A known volume of PAAm-co-RHO precursor was infiltrated into the other inlet of the mold at the same flow rate after the flow of the PAAm-co-FOA was stopped. Once the volume had fully entered the mold, the solution gelled completely. The volumes of PAAm-co-RHO were varied to create different sized regions of PAAm-co-RHO in the final gel.

Consecutive: PAAm-co-FOA precursor was infiltrated into one inlet of the mold at a defined flow rate until the mold was filled with solution. A known volume of PAAm-co-RHO precursor was infiltrated into the other inlet of the mold at the same flow rate immediately after the flow of the PAAm-co-FOA was stopped. A known volume of PAAm-co-FOA precursor was infiltrated into the same inlet as PAAm-co-RHO to push the PAAm-co-RHO precursor deeper into the mold and encase the PAAm-co-RHO in PAAm-co-FOA. Once the volume had fully entered the mold, the solution gelled completely. The volumes of PAAm-co-RHO were varied to create different sized regions of PAAm-co-RHO in the final gel.

Diffusion: PAAm-co-FOA precursor was infiltrated into one inlet of the mold at a defined flow rate until the mold was filled with solution. A known volume of PAAm-co-RHO precursor was

added to the other inlet of the mold and mixed using a micropipette (Eppendorf) for 0 s, 3 s, and 6 s, respectively, after which the solution gelled completely.

Microfluidic-Inspired Operations

2.5D molds of a microfluidic herringbone mixer and gravity separator were 3D printed to gauge the compatibility of this technique with microfluidic operations.

Mixer: PAAm-co-FOA precursor and PAAm-co-RHO precursor were co-infiltrated into a 2.5D, pseudo-microfluidic mixer with dual herringbone-shaped protrusions on the top and bottom of the mold at equivalent flow rates (< 0.5 mL/min) and allowed to gel completely after the flows stabilized. The experiment was repeated in a mold without the herringbone-like protrusions to obtain control samples.

Particle Separator: PAAm precursor doped with blue polyethylene microspheres (47 – 53 μm) was infiltrated into a 2.5D mold containing an array of square-pyramidal indentations on the bottom of the mold. Precursor flow was allowed to stabilize before letting the solution gel completely.

Dynamic Mechanical Analysis (DMA)

PAAm, Ca-ALG, and PAAm-co-Ca-ALG type IV dumbbells conforming to the American Standards for Testing and Materials (ASTM) International standards for tensile testing were made by casting precursor solutions in 3D printed molds of the dumbbell structure. Stress/strain curves for each hydrogel were obtained using a DMA Q800 (TA Instruments)

equipped with a tensile clamp and set with a strain rate of 0.2 mm/min. The following hydrogel compositions were tested: 5% (w/w) PAAm, 7.5% (w/w) PAAm, and 10% (w/w) PAAm; 0.5% (w/v) ALG, 1% (w/v) ALG, and 1.5% (w/v) ALG; 10%/0.5% PAM-co-Ca-ALG. For each hydrogel composition, a subset of the gels was subjected to a 50% HFIP solution diluted in DI for 11 minutes before being allowed to equilibrate in DI for 24 hours. After DI equilibration, these solvent-treated gels were tested alongside their control counterparts. All tensile experiments were taken to failure.

Thermally-Induced Water Loss in Thermo-Sensitive Hydrogel

10% (w/v) PNIPAAm blocks (10 mm x 10 mm x 4 mm) were made in polydimethylsiloxane (PDMS) molds and placed in a DI bath set to temperatures between 25 °C and 50 °C with 5 °C steps to quantify the water loss percentage at each temperature. The blocks spent 10 minutes equilibrating at each temperature before measuring the mass of each block using a NewClassic ME Analytical Balance (Mettler Toledo™). The blocks were returned to the water bath, the temperature was increased, and the cycle repeated until the final measurements at 50 °C were taken. Two subsets (n = 6 each) of the tested blocks were subjected to 100% HFIP for four and eight minutes respectively before being retested for their water loss percentage.

Hydrogel Transparency

The transparencies of hydrogel samples (L: 2 cm; W: 2 cm; H: 2 mm) made of PAAm, Ca-ALG, and PNIPAAm were characterized before and after solvent exposure. A small circuit comprised of a linear DC voltage regulator, a 9-volt (V) battery, and a white light emitting

diode (LED) was made to provide a consistent light source for the experiment. The samples were placed in a semi-dark chamber on a glass slide a minimal distance (touching) away from the LED with another glass slide placed on top to reduce light reflection and scattering. The light illuminance passing through the hydrogels were measured using a REED R8140 LED Light Meter (REED Instruments) and analyzed in MATLAB (MathWorks®).

Functionality Gradients

2.5D molds designed around a 20 mm x 4 mm x 2 mm bar-like space were 3D-printed to characterize simple gradients in stiffness, material constituency, dopant concentration, and chemical moiety concentration created from the collision of opposing inflows.

Stiffness: Opposing flows of 10% PAAm precursor and 5% PAAm precursor (stiff and soft respectively) were infiltrated into modified molds with dumbbell-like grips and hemispherical indentations resulting in dumbbell like hydrogels with hemispherical protrusions down the length of the gel. The gels were placed in a 3D printed stretching fixture and imaged under a microscope in an unstretched state and a stretched state. The displacement between the hemispherical protrusions before and after stretching were calculated in ImageJ (ImageJ) and plotted using MATLAB.

Material: Opposing flows of 10% PAAm precursor and 13%/1% PNIPAAm-co-PAAm precursor were infiltrated into the 2.5D molds and allowed to gel completely. The gels were placed between two glass slides with spacers on each end and submerged in a water bath

above 40 °C. Images taken with a digital single-lens reflex (DSLR) camera (Nikon D3400, Nikon) were quantified for changes in gray value in ImageJ.

Dopant Concentration: Opposing flows of 10% PAAm precursor and 10% PAAm with GNP precursor were infiltrated into the 2.5D molds and allowed to gel completely. Images taken under a binocular microscope (AMScope™), with a DSLR camera and a microscope camera adapter (AMScope), were quantified for changes in gray value in ImageJ.

Chemical Moiety: Opposing flows of 10% PAAm-co-FOA precursor and 10% PAAm-co-RHO precursor were infiltrated into the 2.5D molds and allowed to gel completely. Images taken with a fluorescent microscope (Olympus BX-53, Olympus) were quantified for changes in intensity in ImageJ.

Hydrogel Functionality in 3D

3D fluidic molds were 3D printed to showcase hydrogel creations made using a combination of the infiltration methods and gradient schemes established in this work.

Table: A four-legged table with a geometric flower design on the top, inlets above each leg, and an outlet in the center was 3D printed to highlight stiffness variance within a single structure and 3.5% PAAm precursor was infiltrated into two legs to represent “soft legs” and, before the “soft legs” gelled, 10% PAAm precursor was infiltrated into the other two of the legs as “stiff legs” and the table-top before gelling completely.

Octet-Truss Lattice: An octet lattice mold comprised of seven repeating octet units and two tensile "grips" was carefully infiltrated with PAAm-co-Ca-ALG precursor and allowed to gel completely before removal of the mold.

Flower: A flower mold with an inlet from the top, an inlet from the bottom, and outlets on each "petal" was made to create an environmentally responsive, hydrogel flower. PAAm-co-FOA precursor was infiltrated from the top at a flow rate (0.3 mL/min) twice that of the PAAm-co-RHO precursor flowing in from the bottom inlet (0.15 mL/min). After the flow within the mold stabilized, the solution gelled completely prior to mold removal.

Egg: An egg mold with a large inlet encasing a smaller inlet within it was made to create an egg-shaped hydrogel with an encapsulated, GNP center. 10% PAAm precursor was infiltrated from the larger inlet until approximately 1/3 of the egg was filled. A known volume of GNP-doped 10% PAAm precursor was then co-infiltrated alongside the PAAm precursor at an equivalent flow rate until the flow of this solution stopped. The flow of the PAAm precursor continued until the GNP-doped PAAm region within the mold was fully encapsulated in PAAm. After this occurred, the solution within the egg gelled completely prior to mold removal.

Infrared Thermography

A JANIS VPF-800 vacuum chamber (Lake Shore Cryotronics) was utilized for housing the sampled, and an Edwards T-station 75 turbopump was used to maintain a vacuum level below 10-5 Torr (high vacuum range) for each sample measurement. The samples were

positioned in the vacuum changer with a custom polydimethylsiloxane (PDMS) container and loosely wrapped with an IR-transparent low-density polyethylene (LDPE) film. The sample was imaged with an IR camera (FLIR A655sc with a 25 μm pixel resolution macro-lens, FLIR) through the vacuum chamber's ZnSe window. Laser-heating was applied to the center of the samples for 20 minutes with a 125 mW, 532 nm laser (Big Lasers). Variations in pixel temperature across the sample were normalized by subtracting the laser off-state temperature distribution from the laser on-state distribution.

2.2 Fluidic Sculpting and Release of 3D Hydrogel

The infiltrative assembly process studied herein can be generally simplified into three main steps: 1) 3D-printing of the fluidic mold; 2) infiltration with a hydrogel precursor solution and in-situ gelation; followed by 3) release of the hydrogel by dissolution of the encompassing mold (Figure 2.1a, b). Steps (1) and (3) are primarily responsible for determining the efficacy of the hydrogel sculpting process while step (2) gives users the ability to impart multifunctional attributes to their final construct through the modulation of precursor solutions infiltrated into inlets defined in the mold. A detailed description of the process can be found in the methods of this paper.

In step (1), the effective print resolution of the 3D printer and the fidelity of the hydrogel material to its printed shape determine the resolution of the resultant material. In published research, SLA printers can readily print complex geometries down to nano-scale resolution and we focused on such platforms to synthesize our molds [147], [148], [149]. This enables significantly finer structural features (and enables smooth or rounded walls) than those achievable in wax or sugar printing in existing hydrogel sacrificial templating

studies [116], [117], [118], [119], [120], [121]. Furthermore, by using SLA to design thin, yet sturdy, mold walls, we can reduce the sacrificial material needed, mitigate potential hydrogel damage from the mold dissolution, and expedite the dissolution process. In this research we utilized a low-cost, commercially available 3D printer (Phrozen), alongside a commercially available resin (3DM-ABS) to print our molds. Factors such as the properties of the printing resin, the printing parameters, and the orientation of the mold while printing can cause the dimensions of the mold (and subsequently the hydrogel) to differ from the intended design (Figure 2.2). Commercially available, low-cost SLA printers can print at a putative resolution of down below 50 µm, however in practice it is difficult to generate structural features at these sizes. For our

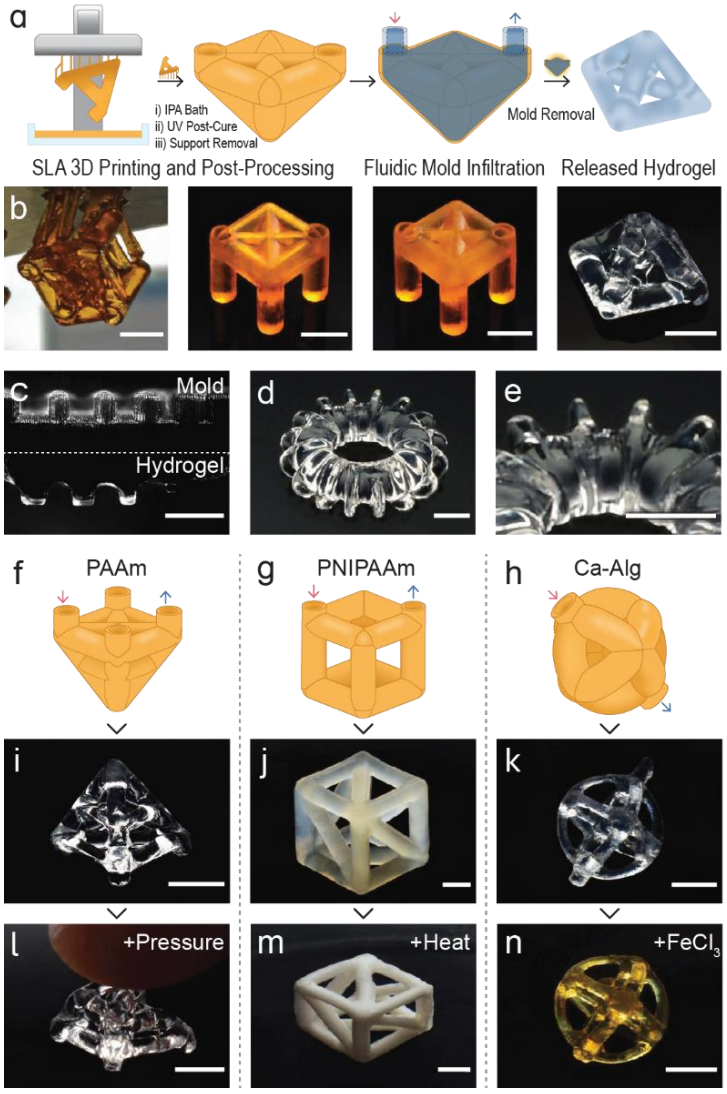

Figure 2.1 | Fluidic Infiltrative Assembly of 3D Hydrogel. a, b. General schematic of the infiltrative assembly process and corresponding images. A sacrificial, fluidic mold is 3D-printed and post-processed prior to fluidic infiltration with a select hydrogel precursor. The mold is dissolved in a gel-dependent manner and the resulting gel is left in DI to recover. **c.** Mold indentations and corresponding hydrogel protrusions for linewidths between 100 - 500 µm. (Scale Bar = 1 mm) **d, e.** Hydrogel donut with 500 µm ridges and a close-up of the ridges. **f, i, l.** Square-pyramid mold schematic and resulting PAAm hydrogel withstanding pressure. **g, j, m.** Cubic mold schematic and resulting PNIPAAm hydrogel exhibiting thermosensitivity. **h, k, n.** Spherical mold schematic and resulting colored Ca-ALG hydrogel after secondary crosslinking with $FeCl_3$. All scale bars are 3 mm unless otherwise stated.

low-cost setup we printed well-defined ridge-openings down to 200 µm; however, more weakly defined openings could be achieved down towards 150 µm. The fidelity of the hydrogel precursor to the mold also affects the final synthesized material as the precursor solution, depending on its surface tension, can trap air within the small, enclosed areas of a mold rendering a particular feature absent or malformed on the hydrogel (Figure 2.1c). We studied several techniques to eliminate this issue, primarily involving pretreatment of the mold with low surface tension solutions (mixed with surfactant or solvent) prior to infiltration of the prepolymer. Proper characterization of a 3D printer's effective resolution, the resin, and the properties of a hydrogel precursor solution are necessary to obtain a high-quality, 3D hydrogel (Figure 2.1d, e).

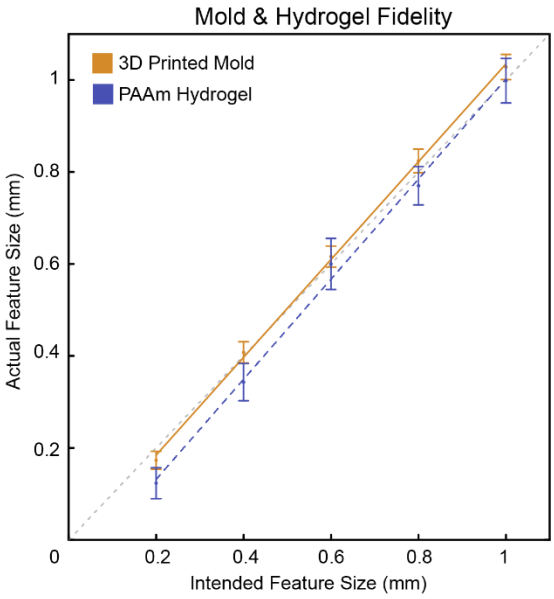

Figure 2.2 | Mold and Hydrogel Fidelity. Mold and hydrogel fidelity relative to the intended design. The orange line is for the mold and the blue line is for the hydrogel. Error bars are standard deviation (n = 5).

Step (3) is critical in determining whether the process is viable for a particular application as the cured SLA resin must be dissolvable and the hydrogel must survive the degradation. In this publication we focused on a commercial ABS (acrylonitrile butadiene styrene)-like resin. Most SLA resins are robust against solvent attack; however, we surmised that the ABS-like resin could be more easily degraded in solvent (ABS printed from extrusion printers can be etched in acetone). We tested ethanol (EtOH), isopropanol (IPA), acetone (ACE), and 1,1,1,3,3,3-hexafluoro-2-propanol (HFIP) as potential water-miscible solvents for the printed material. Results of the testing revealed that HFIP was the only solvent capable

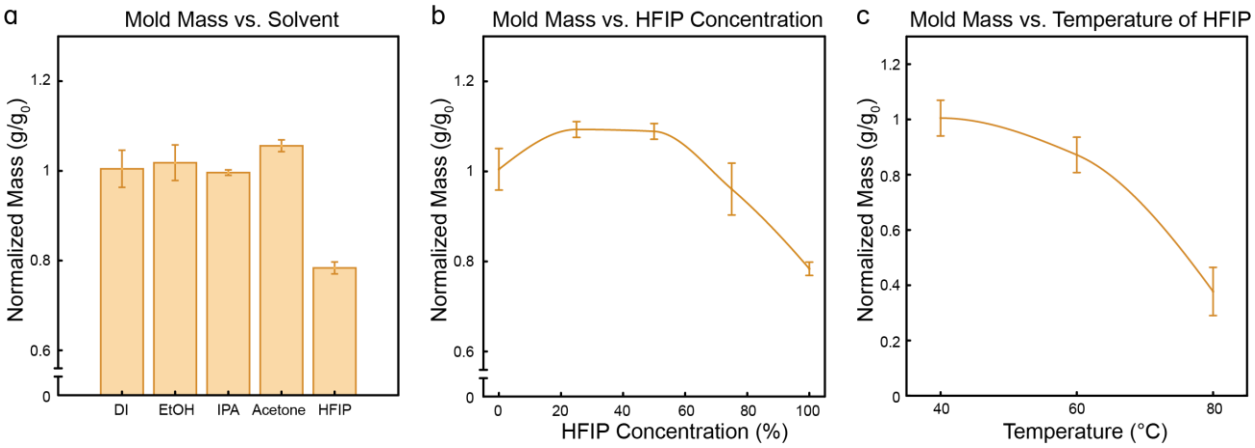

Figure 2.3 | Dissolution Behavior of Cured Resin. a. Effects of different solvents on small cubes of cured resin over one hour. HFIP is the only solvent that dissolves the resin (n = 6). **b.** Effects of HFIP concentration on small cubes of cured resin over one hour. Concentrations between 50% and 100% affect the resin the most (n = 6). **c.** Effects of temperature on rate of mold dissolution in 50% HFIP over 15 minutes. Higher temperatures yield quicker mold dissolution (n = 6). Error bars are

of dissolving the cured resin (Figure 2.3a, b). HFIP is used in lieu of water during the synthesis of some hydrogels and, due to its polarity and water miscibility, is compatible with a variety of polymerized hydrogel [150], [151], [152]. Subsequent testing of the survivability and behavior of polyacrylamide (PAAm), poly(n-isopropylacrylamide) (PNIPAAm), and calcium alginate (Ca-ALG) hydrogels was performed to determine an optimum degradation scheme for three types of hydrogels that represented natural and synthetic sources, different crosslinking mechanisms, and unique functionalities (Figure 2.4a, b).

Optimization of the degradation process on a hydrogel-specific basis allows for the creation of small, 3D hydrogel structures that retain their unique functionality and reflect the resolution of the SLA printer (Figure 2.1f–n). Degradation schemes were developed to minimize the time hydrogels spent in the solvent and the concentration of HFIP, while maximizing the rate of mold degradation as excessive time spent in high concentrations of HFIP led to the gel becoming more brittle and potentially broken as the resin shell deformed and degraded. We found that by increasing the temperature of the degradation reaction, we could minimize the concentration of the HFIP and the solvent exposure time while achieving

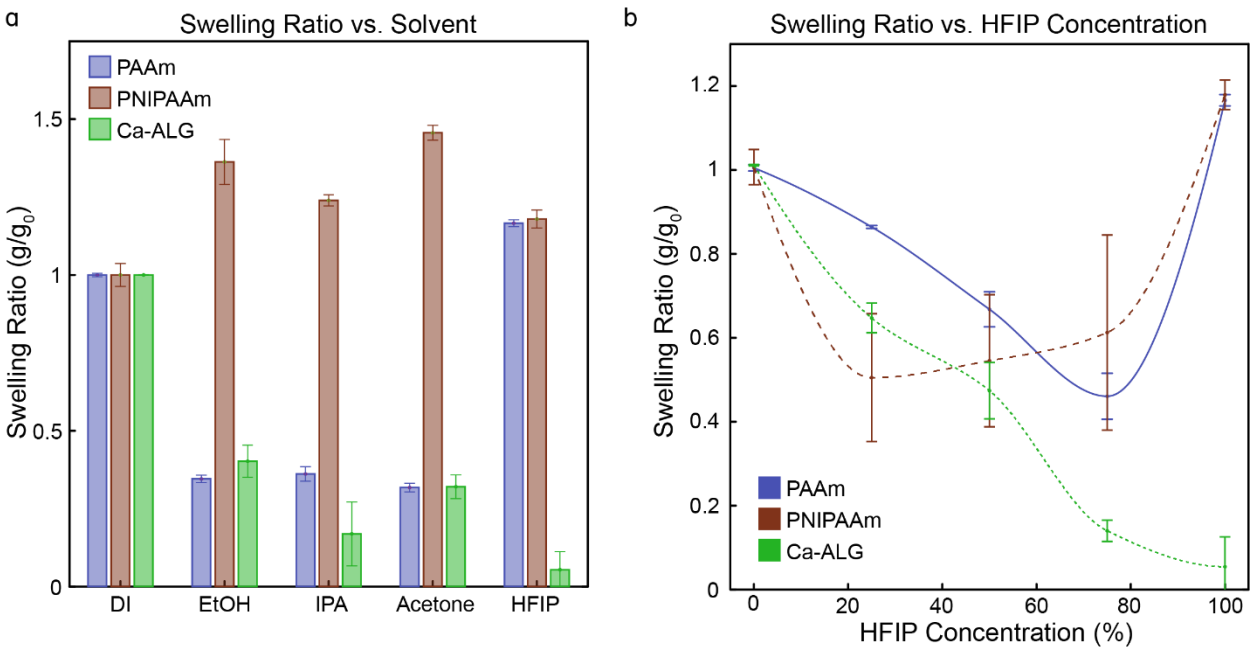

Figure 2.4 | Hydrogel Behavior in Solvent. a. Effects of different solvents on PAAm, PNIPAAM, and Ca-ALG hydrogels. Primary focus is on HFIP as that was the only solvent that dissolved the resin (n = 3) **b.** Effects of HFIP concentration on hydrogel behavior. Minimal effects on swelling behavior of the hydrogels are ideal for these applications (n = 3) (PAAm/PNIPAAm: 50 – 100% HFIP; Ca-ALG: 50% HFIP). Error bars are standard deviation

a satisfactory mold degradation rate (Figure 2.3c). For PAAm and Ca-ALG hydrogels, the degradation process was performed at a temperature of 70 °C in 50% HFIP (determined empirically to provide a good degradation rate without exceeding the boiling point of the HFIP mixture). For PNIPAAm hydrogels, 100% HFIP at 50 °C was used since an HFIP/water mixture yielded large, reversible structural changes in PNIPAAm. This is likely due to co-nonsolvency effects, and can impede the dissolution process and cause the hydrogel to deviate from the expected 3D shape [153]. Due to the more volatile nature of PNIPAAm (which swells and contracts aggressively depending on environment), these gels sometimes require additional tweezer-assisted mold-bit removal after initial solvent treatment. The more brittle behavior of hydrogel in HFIP could be improved by introduction of glycerol to the precursor solution, which acts both as a plasticizer and substitutes for water molecules that enhances hydrogel performance during its short-term exposure to solvent. In the future,

alternative SLA resins that degrade in milder conditions (such as alkaline water solutions) could improve the versatility of this approach.

2.3 Infiltrative Assembly of Hydrogel with Gradient Composition

The infiltration step of the process allows for the creation of heterogeneous hydrogel constructs. This occurs through control of infiltrated precursor solutions alongside their gelation rate. Inlet flow rates, infiltrated volumes, and flow stabilization time can be programmed to modify the local characteristics of the final hydrogel. Additionally, controlling the magnitude of inlet flow rates and the bulk gelation rate of the hydrogel precursor solutions (through crosslinker concentration) enables control over the gradient interfaces that occur between different sections of hydrogel. Slower flow rates encourage near laminar flows that can yield more defined interfacial boundaries, whereas faster flow rates encourage turbulent flows that can stimulate the formation of interfacial gradients. Inversely, slower bulk gelation rates translate to longer time frames over which diffusion can occur between

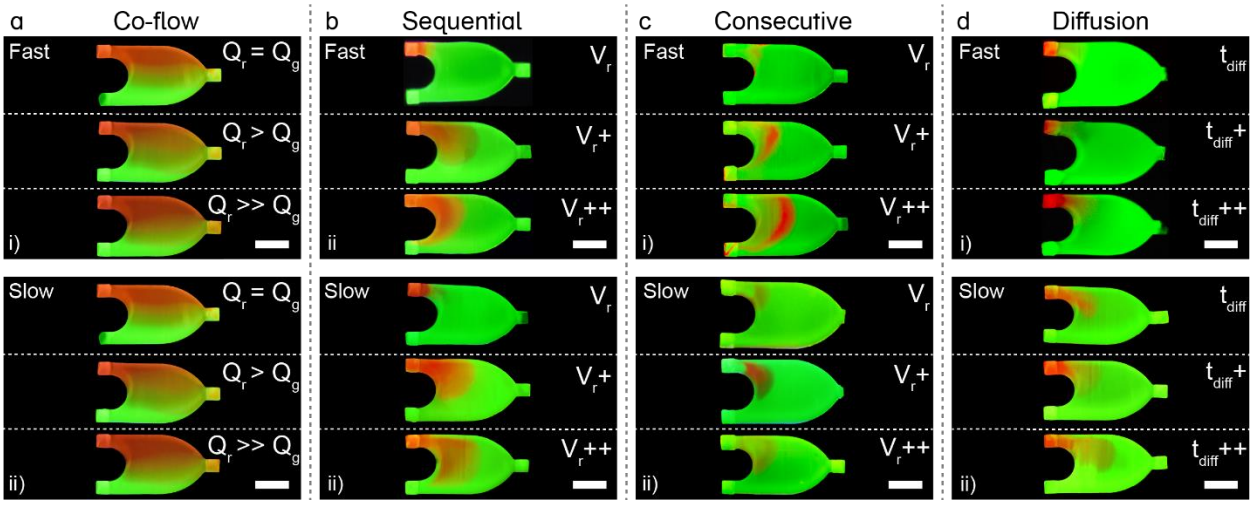

Figure 2.5 | Effects of Gelation Rate on Graduated Interfaces. Hydrogels made of regions of PAAm-co-FOA and PAAm-co-RHO following four methods of infiltration. Varied inlet flow rates, infiltrated volumes, and diffusion time. ai – di. Made to gel quickly after infiltration. aii – dii. Made to gel slowly after infiltration. (Scale Bars = 3 mm)

separate regions (facilitating gradient formation), while faster gelation rates reduce such time frames and encourage more defined boundaries between regions (Figure 2.5a–d). Furthermore, control over the infiltrated volumes yields regions of varying size that add further complexity to the final gel structures.

Simple 3D printed fluidic molds with two inlets and one outlet were used to characterize how four basic methods of fluidic infiltration (co-flow, sequential flow, consecutive flow, and diffusion) can be modulated to yield structurally-complex 3D hydrogels (Figure 2.6ai–di). In this simplified scenario, we studied how the infiltration of two precursor solutions (one modified with fluorescein-modified and the other with rhodamine-modified monomer) could be uniquely coordinated. When flowing two precursor solutions at the same time through a mold (co-flow), differences in inlet flow rates yielded hydrogel regions of different sizes within a single gel (Figure 2.6aii). Sequential flow through alternate inlets could be used to modulate the shape and size of a secondary region within a main hydrogel (Figure 2.6bii). Here the second infiltrated precursor displaces a portion of the initially infiltrated precursor, the volume of which controls the size of the new region. Consecutive flow operates in a manner like sequential flow, however, occurs through the same inlet. This enables the creation of multiple, secondary hydrogel regions within a primary hydrogel (Figure 2.6cii). The size and shape of these regions are defined by the infiltrated volumes and inlet flow rates, respectively. Lastly, diffuse regions of another precursor solution can be incorporated into a gel via passive or active diffusion (Figure 2.6dii). For such experiments, the equalization of precursor solution densities improved the reliability of the final synthesized material.

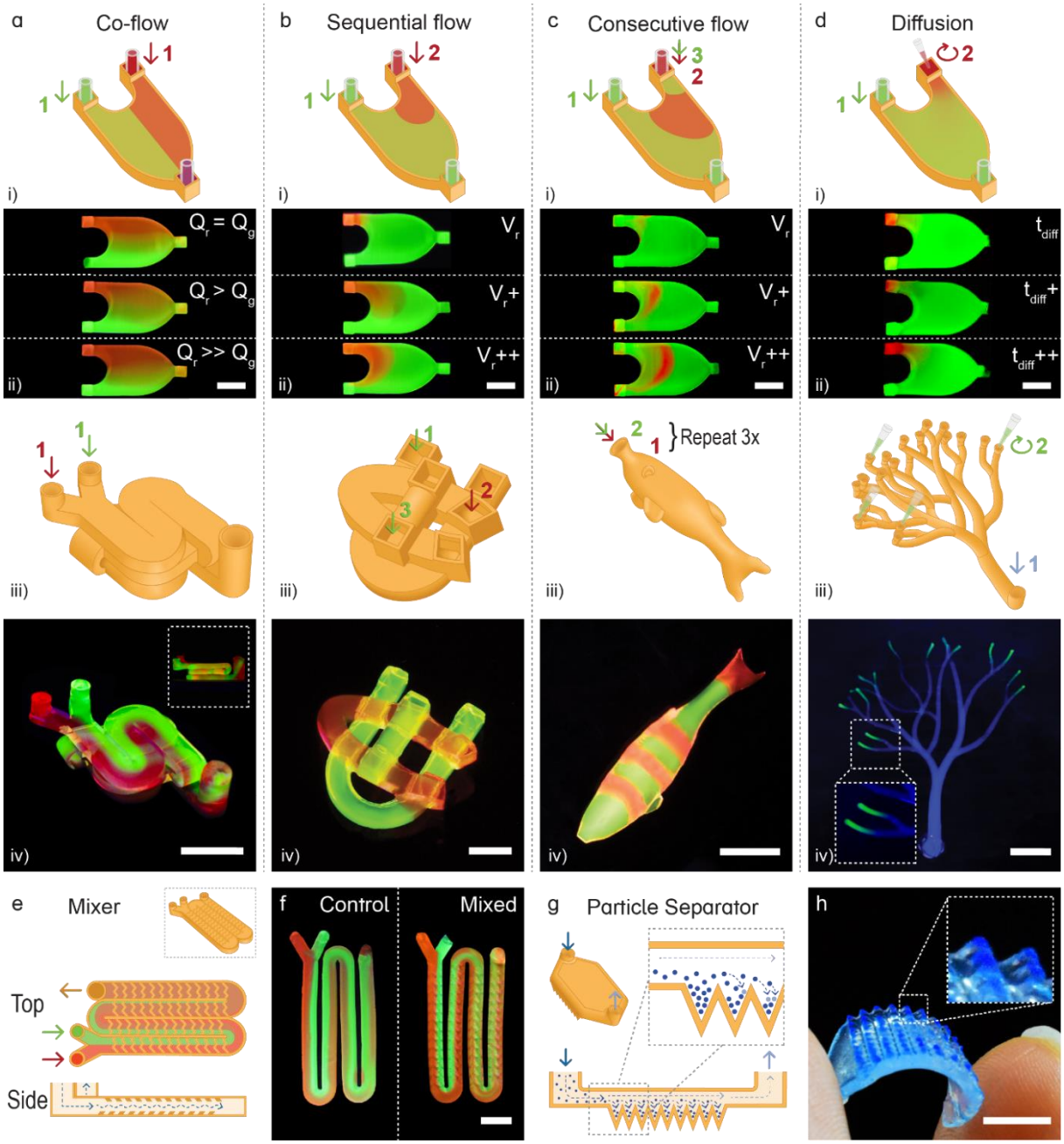

Figure 2.6 | Programmable Fluidic Encoding of Hydrogel Composition. ai – di. Schematics of the four infiltration methods characterized in the study. **aii – dii.** Images corresponding to the four studied infiltration methods with varying inlet flow rates, infiltrated volumes, and diffusion time, respectively. **aiii – diiv.** Schematics of sample 3D hydrogels showcasing the infiltration methods and corresponding hydrogels. The gels showcased are dubbed 3-layer serpentine, UCI, fish, and capillary, respectively) **e, f.** Microfluidic-inspired mixer mold schematic and resulting hydrogels from control and mixed structures. **g, h.** Particle separator mold schematic and resulting hydrogel exhibiting stiff microparticle-tipped needle array. All scale bars are 3 mm unless otherwise stated.

These infiltration and fluidic manipulation strategies can be readily applied to create 3D hydrogels with localized structural and functional characteristics. Examples of such

structures are shown in Figure 2.6aiii–diii with fluorescent PAAm-co-FOA and PAAm-co-RHO as the gel constituents. An alternating, three-layer serpentine structure was made to highlight co-flow-mediated generation of a hydrogel with dual regions of fluorescent polymer that traverse the entire length of the mold (Figure 2.6aiii–iv). PAAm-co-FOA precursor solution and PAAm-co-RHO precursor were infiltrated at equal flow rates (0.3 mL min−1) to maintain approximately the same space within the molds. The resultant gel maintained separate regions of PAAm-co-FOA and PAAm-co-RHO with slight diffusion throughout the winding 3D interface within the material. To highlight sequential flow generation, a multilayer UCI mold was made where the U and the I were made out of PAAm-co-FOA and the C was made out of PAAm-co-RHO (Figure 2.6biii–iv). To make this gel, the U was first filled in with PAAm-co-FOA precursor, then the C was filled in with PAAm-co-RHO precursor before the U fully gelled, and, lastly, the I was filled with PAAm-co-FOA precursor before the C fully gelled. Slight diffusion between the U, C, and I sections of the mold clearly indicate that the resulting structure is a single gel rather than three gelled on top of each other.

To illustrate consecutive flow generation, a fish mold with a single inlet/outlet was 3D printed with the intent of creating a striped hydrogel fish (Figure 2.6ciii–iv). Using a micropipette, alternating aliquots of PAAm-co-FOA and PAAm-co-RHO precursor solutions were gently infiltrated into the mold until the mold was filled. We chose to approximate the thickness of the layers visually, leveraging the distinct colors of the precursor solutions and the transparency of the mold to our advantage. Lastly, to show how diffusion could be used to add complexity to a 3D hydrogel, a capillary-like mold with a large inlet and several 3D interleaving, vessel-like branched outlets was made (Figure 2.6diii, iv). The mold was first

fully infiltrated with a PAAm precursor solution before small aliquots of PAAm-co-FOA were added to each outlet and allowed to diffuse into the vessel tips. The aliquot volumes added to the outlets were dependent on their height from their support because vessels above others in height experienced gravity-mediated diffusion that reduced the amount of PAAm-co-FOA needed to achieve the same diffusion as lower vessels.

Microfluidic operators can also be built-in to the sacrificial 3D-printed shell to further facilitate control over the resultant hydrogel. As a demonstration of this, two molds inspired

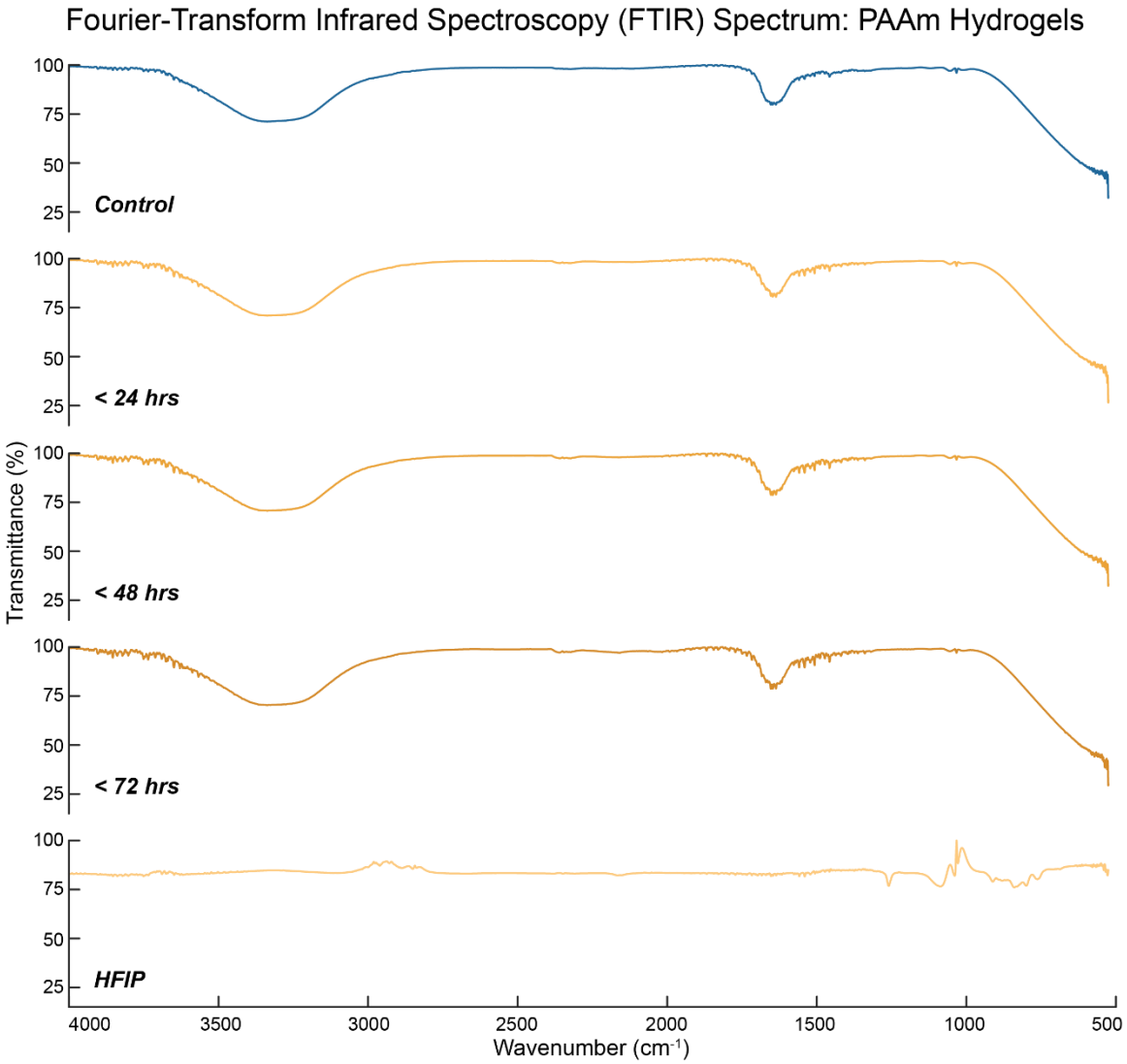

Figure 2.7 | FTIR Spectrum of PAAm Hydrogels. FTIR Spectrum of PAAm hydrogels after being subjected to the dissolution protocol. Presented are the spectra for control gels, treated gels after less than 24 hours in DI, treated gels after 48 hours in DI, treated gels after less than 72 hours in DI, and pure HFIP for comparison.

by microfluidic operations (a mixer and a gravity separator) were developed. The mixer mold was inspired by a staggered herringbone mixer and has dual herringbone shaped protrusions on the top and bottom of the molds inner surface down the length of the mold to facilitate mixing between PAAm-co-FOA and PAAm-co-RHO (Figure 2.6e) [154]. Control and mixer-integrated molds were co-infiltrated with fluorescing precursor solutions and allowed to gel. Control molds yielded materials with highly distinct fluorescent regions, whereas mixer-integrated molds generated more intermixed constructs, particularly at the middle and end of the channel (Figure 2.6f). The separator mold was inspired by microfluidic gravity separators and synthesizes a 3D needle-like array with square pyramidal indentations on the bottom. This structure allowed for the sedimentation of stiff blue polystyrene microspheres from a PAAm precursor solution (Figure 2.6g) [155]. When the mold was removed, the bulk of the resulting gel remained clear, but the tips of the square pyramid array were bright blue, demonstrating that the mold was successful in separating the microspheres from the precursor solution to form a hydrogel with stiff needle-like tips (Figure 2.6h).

2.4 Hydrogels with Programmable Heterogeneity in Function

Hydrogel structural and functional properties following HFIP treatment were investigated to assess the impact of the sacrificial release step on hydrogel performance. We first investigated the residual presence of HFIP in PAAm hydrogels by obtaining Fourier-transform infrared spectroscopy (FTIR) spectra of gels that had been exposed to HFIP and allowed to remain in DI for some time after exposure. The spectra indicates that there is no residual HFIP remaining in the PAAm hydrogels (Figure S2,7a, b). Tensile tests were performed on Type IV “dog bone” hydrogel specimens of PAAm, Ca-ALG, and an

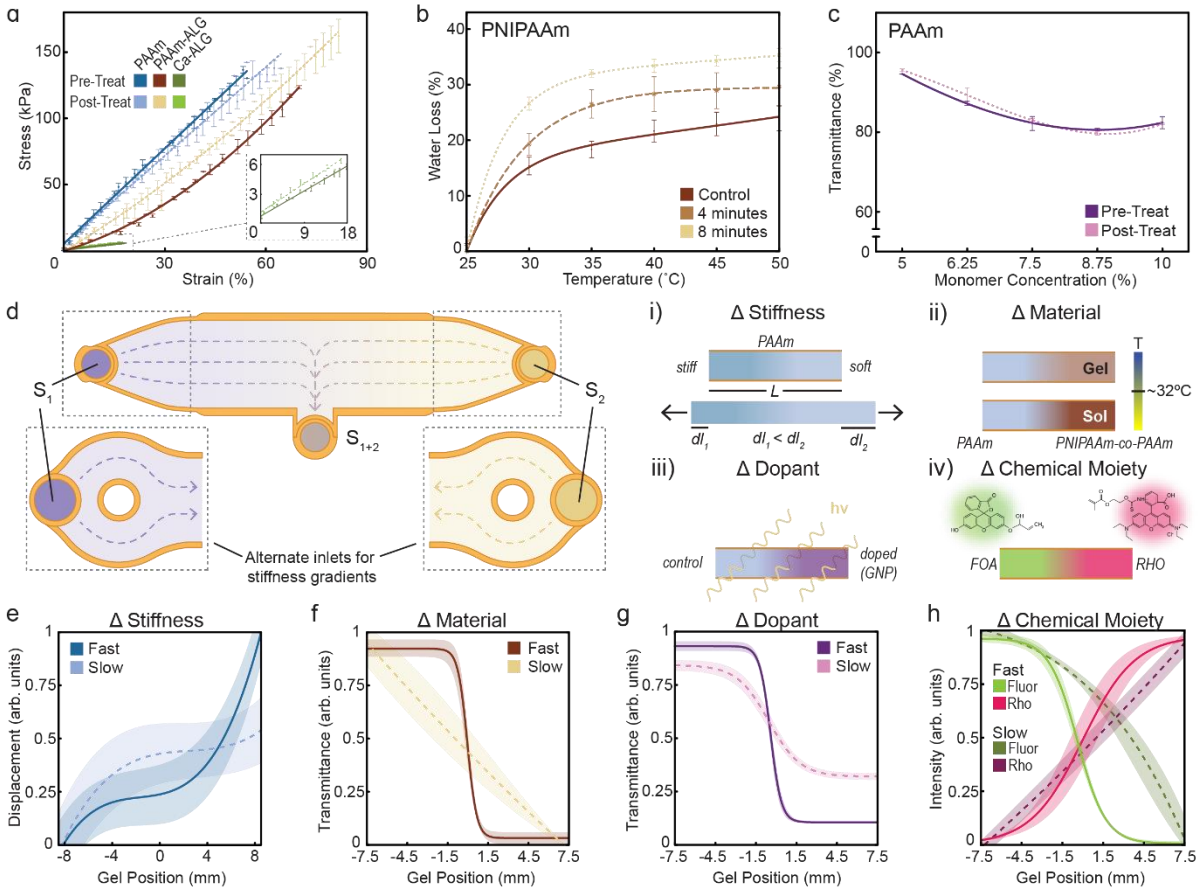

Figure 2.8 | Hydrogel with Programmable Heterogeneity in Behavior. a. Stress vs. Strain graph showing the difference in tensile behavior of a hydrogel before and after exposure to the hydrogel-specific dissolution protocols (n = 4). b. PNIPAAm contraction in response to higher temperatures after subjecting to set HFIP exposure times. Greater water loss % due to temperature was associated with increasing solvent exposure (n = 3). c. Transparency of PAAm hydrogels before and after exposure to its dissolution protocol (n = 3). di – div. Schematic of a bar-based fluidic mold with interchangeable inlets for creating gradients in stiffness, material constituency, modifier concentration, and chemical moiety. e – h. Quantification of hydrogel gradients at slow and fast gelation rates. Error bars and shaded regions represent standard deviation.

interpenetrating polymer network (IPN) of PAAm and Ca-ALG (PAAm-ALG) subjected to the conditions of the mold removal step in accordance with ASTM Standard D638-14 to assess the effect of HFIP on mechanical behavior [156]. No significant differences in the stress/strain behavior of the hydrogels were found as they exhibited nearly the same behavior before and after solvent exposure (Figure 2.8a; Figure 2.9a, b). Thermosensitive PNIPAAm hydrogels were also subjected to these conditions to evaluate whether HFIP impacted the "smart," swelling behavior of the gels to temperature. Longer exposure to the

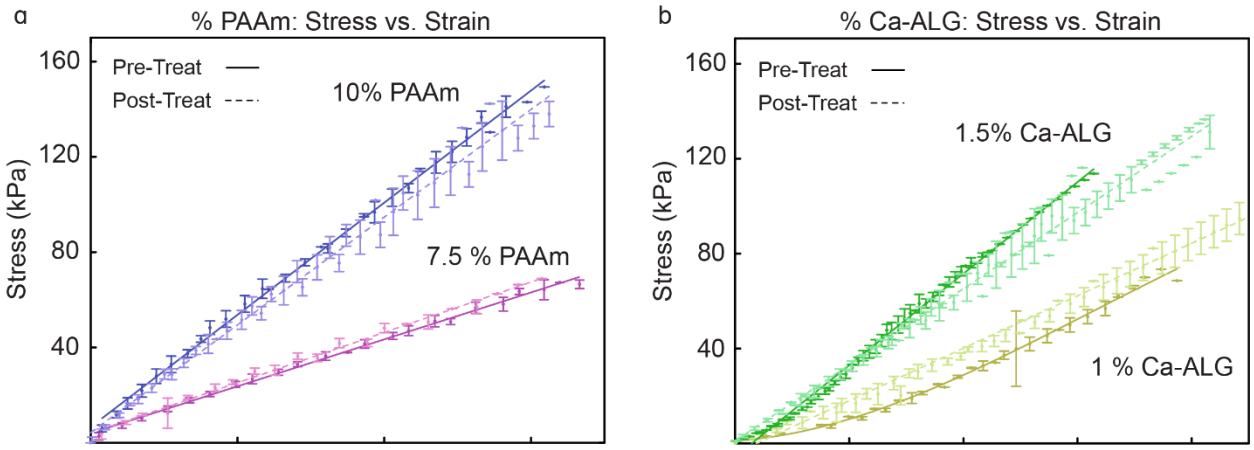

Figure 2.9 | Tensile Behavior of PAAm and Ca-ALG at Different Monomer Concentrations. a. Tensile behavior of two concentrations of PAAm hydrogel before and after HFIP exposure (n = 4). b. Tensile behavior of two concentrations of Ca-ALG hydrogel before and after HFIP exposure (n = 4). Error bars represent standard deviation.

solvent increased PNIPAAm sensitivity to thermal stimuli, as they exhibited greater water loss percentages to temperature in proportion with the time spent in solvent (Figure 2.8b). The mechanism behind this phenomenon warrants further investigation, but we suspect the HFIP treatment primes the material for subsequent structural transformations (the solvent itself contracts the hydrogel). Lastly, PAAm, Ca-ALG, and PNIPAAm hydrogels were tested for changes in their opacity that could potentially be introduced under mold removal conditions. The opacity of the hydrogels remained unchanged following solvent exposure (Figure 2.8c; Figure 2.10a–c). These results are further supported by scanning electron microscopy (SEM) images of PAAm and Ca-ALG hydrogels depicting minimal to no differences between gels that had been exposed to HFIP and gels that had not (Figures 2.11a, b).

A primary advantage of this technique is the ability to induce flow-defined heterogeneity within a 3D structure through a combination of geometric design, tuned infiltration, and control over material constituents. To highlight this, bar-like molds with two inlets at opposite ends and a centrally located outlet were 3D printed to create gels with gradients in stiffness, monomer constituency, modifier concentration, and chemical moiety

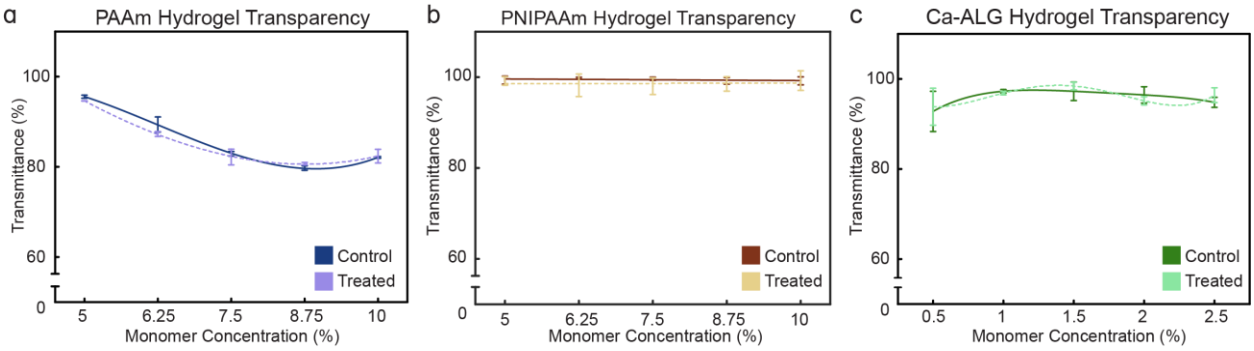

Figure 2.10 | Optical properties of PAAm, PNIPAAm, and Ca-ALG hydrogels. Optical properties of hydrogels at different monomer concentrations before and after solvent exposure. a. PAAm hydrogels (n = 3). b. PNIPAAm hydrogels (n = 3). c. Ca-ALG hydrogels (n = 3). Error bars represent standard deviation.

(Figure 2.8di–iv). While the latter three gradients utilized a simple bar-like mold for their structures, the stiffness gradient mold was modified to include dumbbell-like inlets and an array of hemispherical indentations spaced evenly across the length of the mold for displacement quantification (Figure 2.12). We further tested whether these gradient materials could be modulated by simple control of gelation rate.

For the stiffness gradient, the dumbbell-like inlets on the modified mold became hydrogel grips for a 3D sculpted stretching fixture. This was infiltrated with 5% and 10% PAAm precursor solutions. Hemispherical protrusions were built-in along the length of the mold to enable quantification of local structural displacement under strain. Such integrated

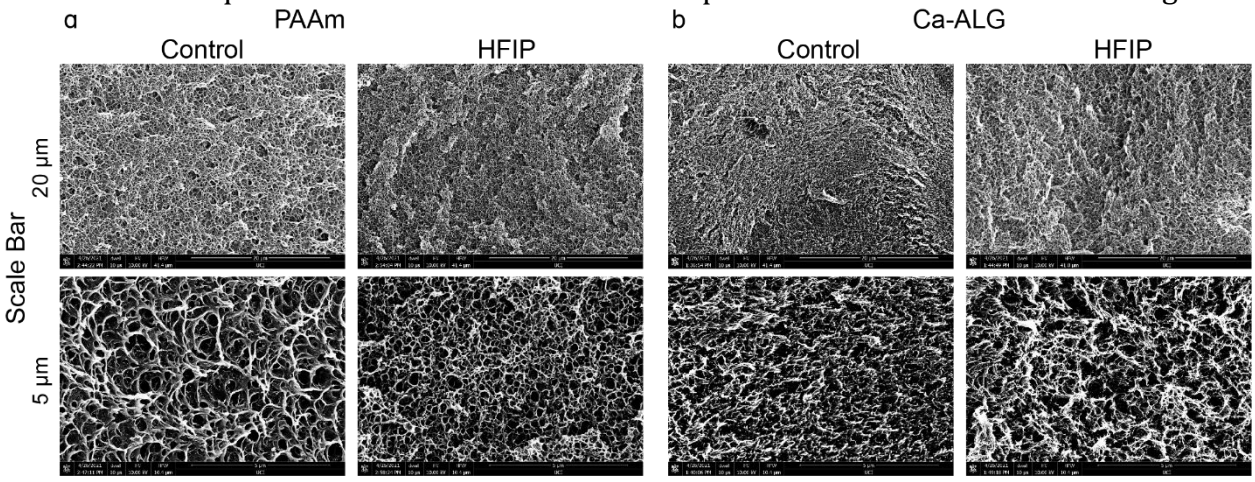

Figure 2.11 | SEM Images of PAAm and Ca-ALG Hydrogels. PAAm and Ca-ALG hydrogels subjected to the dissolution protocol were imaged with an FEI Magellan 400 SEM at 5,000x and 20,000x. a. PAAm hydrogels at 5,000x and 20,000x. b. Ca-ALG hydrogels at 5,000x and 20,000x.

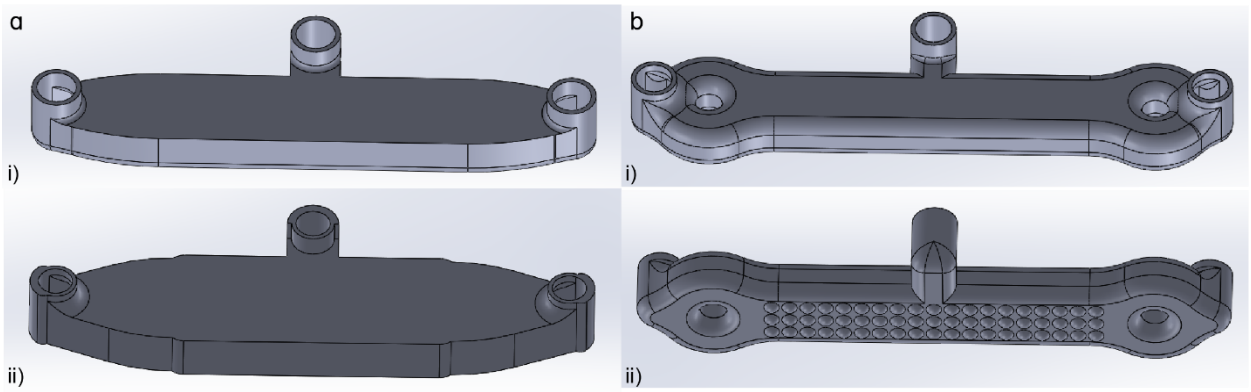

Figure 2.12 | CAD Designs of Gradient Molds. ai – ii. Bar molds used for material, dopant, and chemical moiety gradients in hydrogels. bi – ii. Bar mold with grips and dome-like indentations for creation of stiffness gradient hydrogels.

design is a powerful advantage of this technique, which allows materials to be synthesized on a whim to fit experimental needs (Figure 2.13). These hydrogels were set on the fixture and imaged in stretched and unstretched states, where the stretching distance remained constant. All resulting hydrogels exhibited low displacement near the stiffer end of the gel (10% PAAm) and high displacement near the softer end of the gel (5% PAAm) with a point of inflection occurring at the center of the gels (gel position 0 mm). The resultant stiffness gradient varied with the gelation rate (Figure 2.8e). Hydrogels with a faster gelation rate (Fast) exhibited a large differential in displacements (and highly varying stiffness) between the two sides of the gel. “Slow” gels with a reduced gelation rate exhibited a much smaller differential in displacement and more even stiffness across the structure. Here, the slower gelation rate allowed more time for diffusion of monomer from high to low concentration regions, thus leading to a more uniform material.

Material gradient gels were composed of co-infiltrated solutions of PAAm and PNIPAAm-co-PAAm respectively. Resultant structures were placed in a water bath above the lower critical solution temperature (LCST) of PNIPAAm to induce a sol-gel transition in PNIPAAm-co-PAAm within the hydrogel. This is accompanied by a change in the opacity of

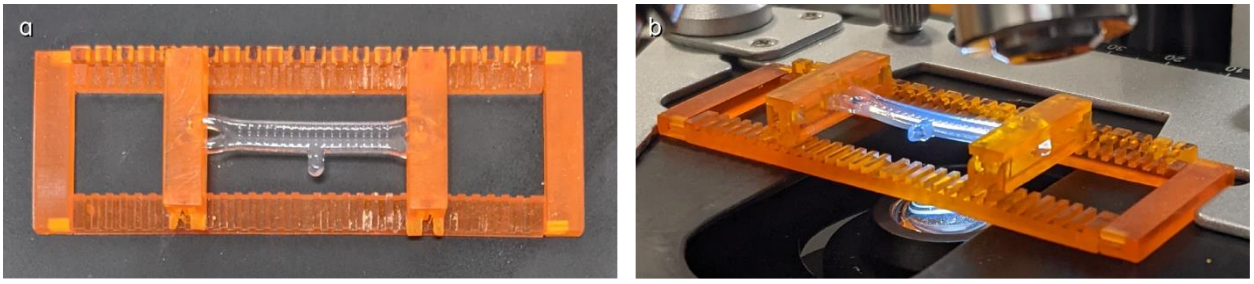

Figure 2.13 | Fixture for Applying Controlled Stretch to Stiffness Gradient Hydrogel. a. Top view of stretched PAAm gel. b. Isometric view of fixture and gel on a binocular microscope.

the hydrogel (Figure 2.14) [157], [158]. PAAm hydrogel is not inherently thermosensitive and local regions will turn opaque in correlation with the local PNIPAM concentration. Gradients of PNIPAAm-co-PAAm were quantified through measurement of the transmittance of light across the gel. All resulting hydrogels exhibited decreasing light transmittance closer to the PNIPAAm-co-PAAm side of the gel (Figure 2.8f). Hydrogels with a faster gelation rate (Fast) followed sigmoidal behavior with high light transmittance closer to the PAAm side of the gel, a narrow, gradated region between the two materials, and a consistently low light transmittance closer to the PNIPAAm-co-PAAm side. Gels with a slower gelation rate (Slow) also exhibited the same decline in transmittance from the PAAm side to the PNIPAAm-co-PAAm side but rather than following sigmoidal behavior the decline was more linear as the material gradient spanned the length of the gel due to more diffusion of NIPAM monomer.

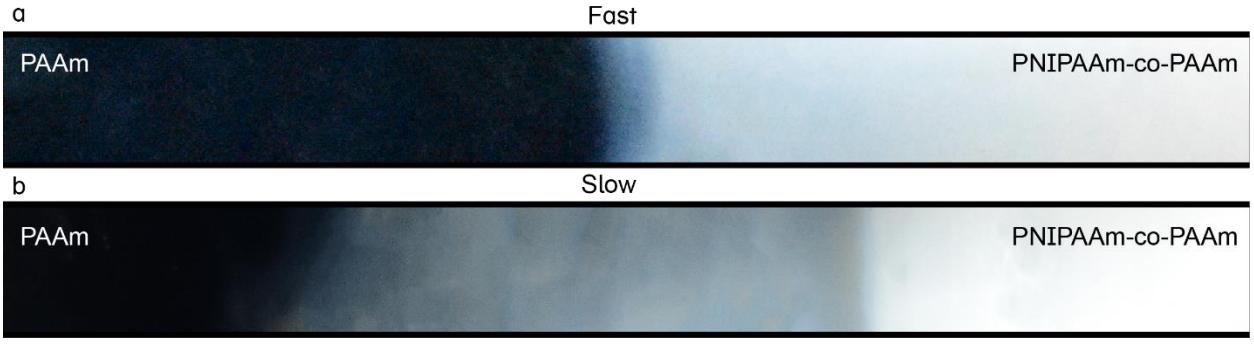

Figure 2.14 | Differences in Transparency for Fast and Slow Gelling Material Gradient Hydrogel. a. Fast gelation. b. Slow gelation

Nanomaterial-modified gradient gels were composed of unmodified and gold nanoparticle (GNP) modified precursor solutions. Resultant gels were imaged to quantify nanoparticle-induced red-purple coloration within the hydrogel. As expected, hydrogels had whiter/clearer coloration closer to the unmodified side of the gel, while the purple GNP in the modified side of the gel absorbed/scattered light (Figure 2.8g). Hydrogels with a faster gelation rate (Fast) exhibited sigmoidal behavior with clear coloration on the unmodified side, a narrow, graduated region between, and darker coloration on the modified side. Gels with a slower gelation rate (Slow) also exhibited sigmoidal behavior, however the maximum and minimum coloration on the unmodified and modified sides respectively dropped as greater diffusion of the GNPs resulted in a more gradual gradient across the gel.

Lastly, we tested hydrogels with gradients of chemical moieties, in this case, two solutions modified with fluorescein and rhodamine, respectively. Fluorescent images of the chemical-moiety gradient hydrogels were taken and quantified based on the fluorescent intensity across the length of the gels. Similar with previous graded gels, a faster gelation rate (Fast) exhibited sigmoidal behavior with a smaller window between the top and bottom plateaus that results from reduced diffusion time for the fluorophores. A slower gelation rate resulted in greater diffusion of the fluorophores to the opposing sides and a somewhat more linear change in fluorescent intensity of the hydrogel across its length.

2.5 Synthesis of 3D Hydrogel Systems

Through proper material selection and creative infiltration, unique multi-material structures with region-specific functionality can be easily built. As demonstration, four 3D structures were synthesized that represent the structural tunability, synergy between

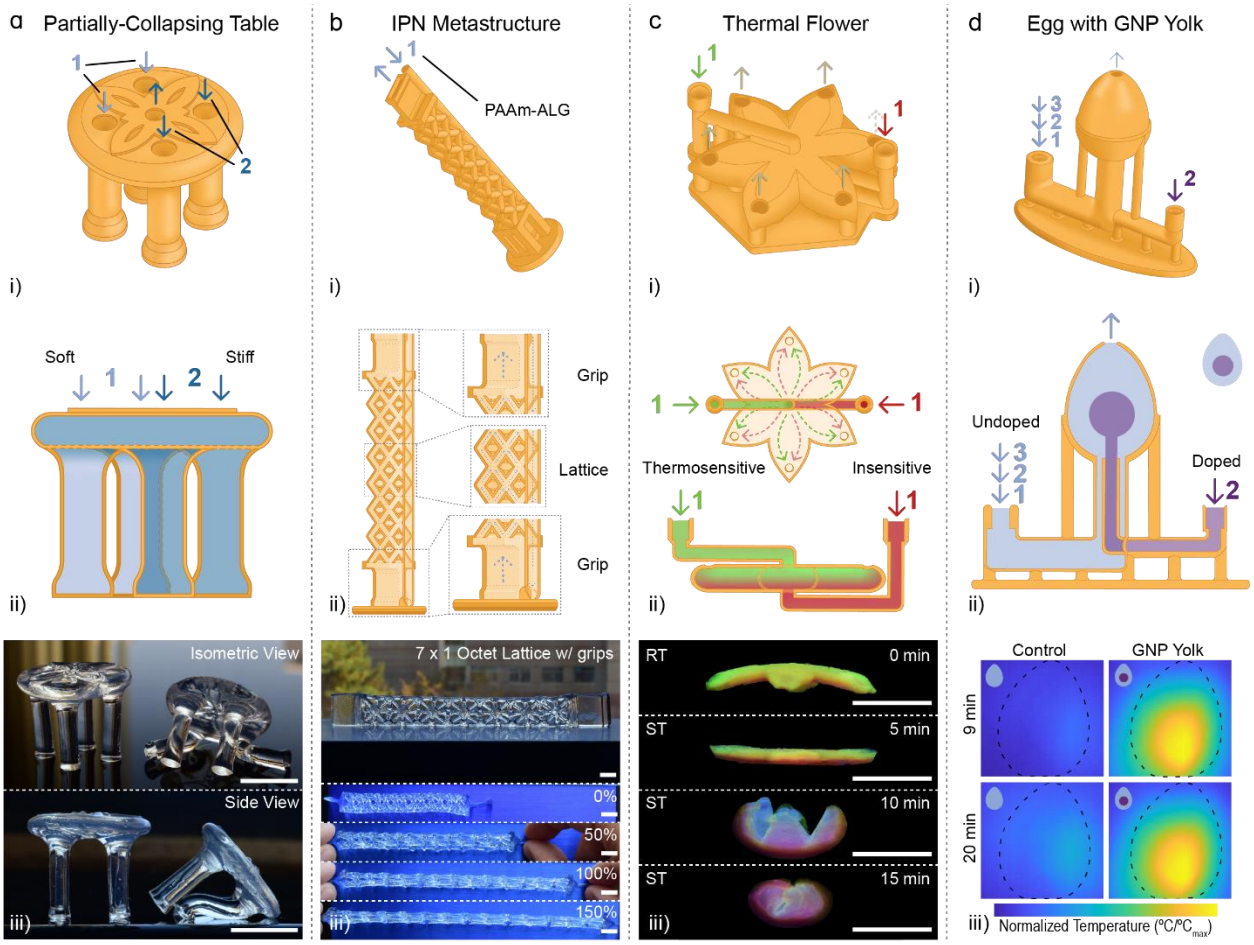

Figure 2.15 | Infiltrative Assembly of Hydrogel with Programmable Form and Function in 3D. a. Partially collapsing table mold schematic and resulting control and gradient hydrogel with two soft table legs. Demonstrates facile control over the material properties of a free-standing hydrogel. bi – biii. Octet-truss lattice mold and resulting interpenetrating network hydrogel. ci – ciii. Thermal flower mold schematic and resulting fluorescent bilayer hydrogel with a gradient in temperature-responsive function. di – diii. Egg schematic and resulting hydrogel with a core "yolk" of gold nanoparticles. Driven via sheath flow, this enables the rapid and facile synthesis of 3D encapsulated functionality through engineering flow and function within user-defined molds. High surface temperature of the egg upon green laser illumination indicates the high interior temperature emanating from the center GNP of the egg. All scale bars are 5 mm unless otherwise stated.

material choice and geometric constraint, and multimaterial functionality that can be achieved via this process (Figure 2.15ai–di). Our first structure is an ornate, gradient stiffness table. This structure contained inlets above those legs, a central outlet, and a sub-millimeter flower flourish was designed above the table to highlight structural tunability (Figure 2.15ai). The table was designed with ease of infiltration in mind, as the location of the inlets above the legs allowed for modulation of the material composition of each leg

independently. In this case, 3.5% PAAm precursor solution (soft material) was infiltrated into two of the table legs using a micropipette, before the other legs were filled with 10% PAAm (stiff material) (Figure 2.15aii). Before any leg had completely gelled, the tabletop was gently filled with more 10% PAAm precursor to connect the four legs together. The resulting gel was a table with two legs that buckled under its own weight and caused the table to partially collapse towards its soft legs (Figure 2.15aiii). This simple-to-make construct highlights how fluidic infiltration and material selection enables straightforward and rapid region-specific tuning of a complex, 3D hydrogel.

An octet-truss lattice mold consisting of seven repeating units in series and tensile grips on each end was designed and printed to demonstrate the synergy that can be achieved between material choice and the structural control offered by this approach (Figure 2.15bi). The octet-truss lattice is the most common form of stretching-dominated, mechanical metastructure used for engineering applications as it functions as a light-weight energy absorption structure with ideal linear scaling of mechanical properties [159], [160], [161], [162], [163], [164]. The mold was designed with a long inlet that spanned the length of the lattice to allow for infiltration from the bottom of the mold to eliminate bubbles, as bubbles translated to structural defects in the gel (Figure 2.15bii). We chose to infiltrate PAAm-ALG as this hydrogel exhibits excellent biocompatibility and unique mechanical properties [165], [166], [167], [168], [169]. Such IPN gels are difficult to synthesize using traditional 3D-printing techniques and can capitalize on the structural advantage of the octet-truss lattice. As a proof of concept, a basic PAAm-ALG formulation was sculpted into a high fidelity, octet-truss lattice with the ability to stretch to two times its original length if taken to failure (Figure 2.15biii).

A flower-like mold was fabricated to highlight environmental-responsiveness of 3D multimaterial constructs. This mold consisted of two inlets entering above and below the central point (flowing red, fluorescent PAAm and green, fluorescent PNIPAM-co-PAAm respectively), and six petals with outlets on their tips. This forms a fluorescing, thermo-responsive hydrogel bilayer with a graduated interfacial boundary (Figure 2.15ci) that can be synthesized in-situ. Note that such fluorescent structures are difficult to synthesize using direct laser printing due to bleaching in UV light. Thermo-responsive hydrogel bilayers incorporating PNIPAAm as its thermosensitive element have been previously reported in literature and are generated by either forming one layer on top of another after complete gelation of the former or by adhering two layers together using an adhesive [170], [171], [172], [173], [174]. These bilayers are often employed as actuators in solutions that bend as the temperature exceeds the LCST of PNIPAAm. The PNIPAAm-co-PAAm-co-RHO precursor had a lower density than the PAAm-co-FOA precursor so we designed the mold such that the less dense precursor could enter from above and the denser precursor could enter from below (Figure 2.15cii). The resulting gel was a green and red hydrogel bilayer that closes like a flower when exposed to temperatures exceeding the top layers LCST, and additionally possessed a graduated interfacial boundary linking the two materials together (Figure 2.15ciii). By modifying the inlet flow rates of the precursors, we changed the thickness of the layers and modulated the contractile behavior of the resulting gel to our specification. Gels with greater complexity and functionality could be easily fabricated by modifying the mold geometry, the precursors, or the infiltration strategy.

The final structure was a simple egg synthesized using sheath flow. Opposing inlets, small and large, were designed to meet below the egg portion of the mold where the small

inlet would enter the large inlet and form a 3D sheath co-flow structure (Figure 2.15di). This infiltration strategy allows for precursor of the small inlet to be surrounded by the precursor entering from the large inlet as the solutions fill the egg mold and exit through an outlet at the top. By controlling the inlet flow rates and the inflow times, the resulting egg could have a hydrogel encapsulated within another hydrogel, a "yolk", with a diffuse gradient between them (Figure 2.15dii). Initially, PAAm precursor was infiltrated into the mold without the GNP-modified PAAm precursor to form the top portion of the egg. Once a bottom third of the egg mold had been filled, we began infiltrating a known volume of GNP-modified PAAm precursor without stopping the flow of the PAAm precursor. After the volume had been fully infiltrated, we waited a few seconds to cut off the GNP-modified PAAm precursor from the inlet with PAAm precursor before stopping the infiltration. The resulting hydrogel was a high-fidelity egg with a GNP "yolk" that induced a local temperature gradient when subjected to a laser stimulus (Figure 2.15diii). When exposed to a 125 mW, 532 nm, hand-held laser (Big Lasers) for 20 min, the egg experienced significant temperature increase in the GNP "yolk," which results in heating at the surface of the hydrogel of that can be quantified via infrared thermography. While not directly quantified, we expect the core of the hydrogel to be significantly hotter than this measured surface.

2.6 Concluding Remarks

The combination of sacrificial hydrogel templating with coordinated injection molding strategies presented here enables the facile synthesis of unique, soft multi-hydrogel architectures and offers a significant advance from the state-of-the-art in this field in sacrificial hydrogel molding. These synthesized architectures possess: 1) comparatively

high-resolution, high-aspect ratio beams, and fine curvilinear surfaces; 2) finely controlled materials of gradient composition engineered at micrometer length-scales; and 3) unique heterostructures through the direct programming of microfluidic flow driven via mixing, sheath, and particle separating flows induced during material formation. This versatile approach should be directly compatible with any SLA-based 3D printer enabling the fabrication of architectures with nanoscale features dependent on the printer's resolution. Our approach draws a direct technological thread between stereolithography, microfluidics, and aqueous-assembled materials—each enormous fields in their own right. We believe our approach can integrate technological advances in each of these fields to achieve next-generation heterogeneous material-systems with characteristics approaching or exceeding natural counterparts.

CHAPTER 3

Mechanically-directed assembly of nanostructured biopolymer with tunable anisotropy, hierarchy, and functionality

Anisotropy is a common architectural feature in tissues that works in conjunction with their distinct compositions to facilitate tissue-specific function [175], [176]. Complex anisotropic gradients originate from the hierarchical, nano-to-macroscale organization of tissue constituents and impart direction-dependent properties [115], [176], [177]. As examples, skeletal, myocardial, and intestinal smooth muscles contract in distinct patterns to facilitate movement, pump blood, and move food, respectively [178], [179], [180]. These distinct contraction patterns are derived from key differences in anisotropic orientation present within each muscle's structural hierarchy [20]. Skeletal muscle is organized in uniaxially aligned constituents at three distinct organizational levels, whereas myocardial and intestinal smooth muscle are more intricately arranged into multilayer lamellae with distinct orientations in plate-like or tube-like arrangements, respectively [20], [178], [179], [180], [181], [182].

Common methods for introducing structural anisotropy in tissue scaffolds yield unidirectional alignment with little control over nanoscale architectures [20]. These methods typically involve the direct or indirect application of a directional force to orient biomaterial constituents during or after gelation. Directional freeze-casting is a form of thermally-induced phase separation that establishes a thermal gradient while a polymer solution is being frozen, resulting in unidirectional ice crystal growth and aligned pore

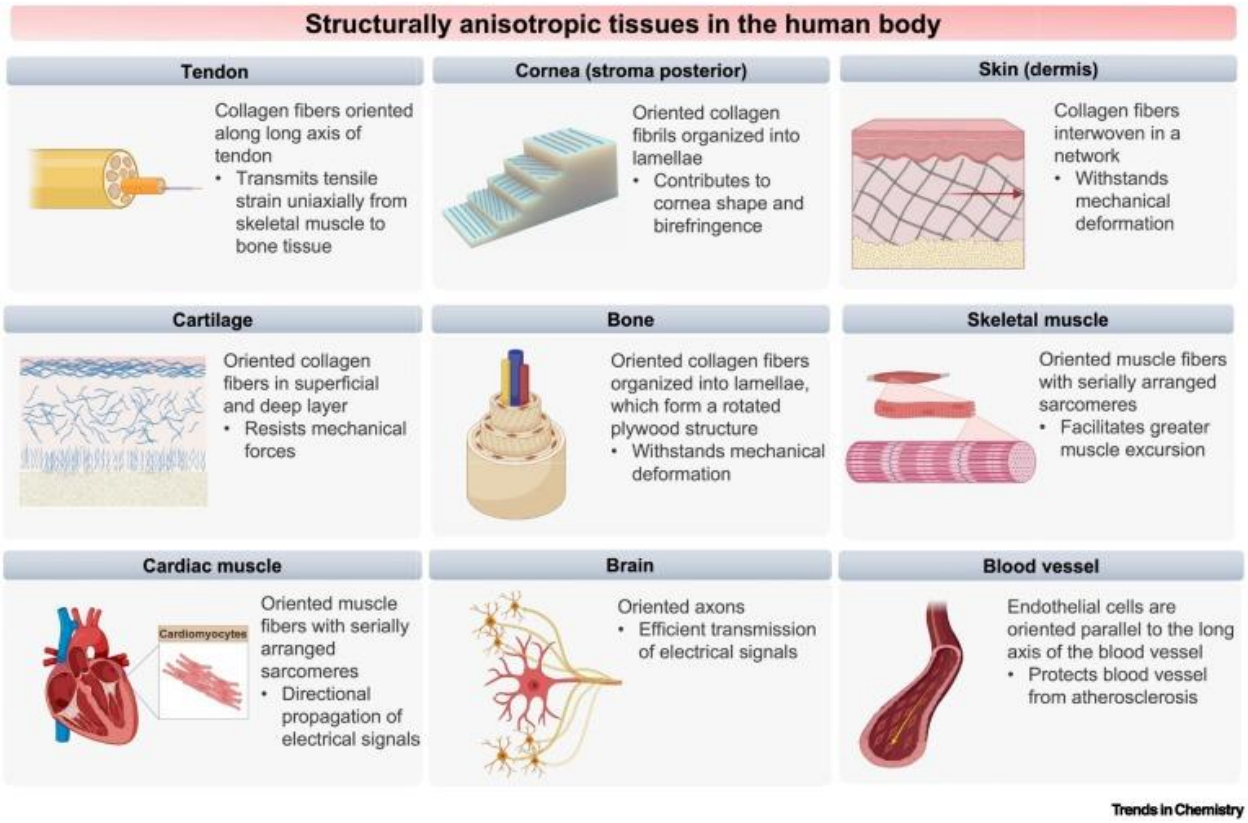

Figure 3.1 | Complex Anisotropic Gradients in Tissues. Schematic detailing various anisotropic tissues and how the anisotropy facilitates tissue function. Extending existing fabrication techniques to produce these anisotropic gradients is key to replicating anisotropic tissue function [115].

formation after subsequent freeze-drying [183], [184], [185], [186], [187]. As noted in Chapter 1, externally applied fields (e.g. electric, magnetic, acoustic) can orient polymers and/or additives in solution during solvent casting, leveraging the inherent material properties of the constituents to yield structural anisotropy [89], [90]. Shear stress can induce polymer alignment during extrusion-based printing and enable greater control over scaffold architectures via additive manufacturing strategies (Figure 3.1) [115], [176], [188]. Stress can also be applied after scaffold formation by the direct or indirect application of strain and can be locked in their orientation by additional crosslinking [189], [190].

Few methods exist to induce two-dimensional (2D) or three-dimensional (3D) structural anisotropy in scaffolds that can also produce complex structures and apply to a wide range of biomaterials [191]. Bidirectional freeze-casting and directed ion diffusion have

been shown to produce lamellar and tubular anisotropic gradients, respectively, but they have only been shown to produce simple structures [191], [192]. Stereolithography (SLA) is a high-resolution form of light-based 3D printing that possesses excellent control when printing down to microscale features but becomes limited towards the nanoscale [193], [194], [195]. Furthermore, such 3D-printed structures are often miniature replicas of macroscale structural networks (as seen in architectural constructs) and are not directly reminiscent of natural materials. It is necessary to address these limitations to achieve greater biomimicry of complex tissue architectures in a manner that accommodates research endeavors and eventual clinical translation.

Here, we perform considerable extensions on a bio-inspired technique, termed mechanically-directed assembly (MDA), that uses tunable mechanical strains to control the anisotropy (and corresponding properties) of 2D molded polymers [141], [196], [197]. MDA produces porous, hierarchical materials with structural control at nano-to-macro length scales that can extend into 3D through material buckling. Two concurrent approaches were taken to improve the accessibility and usability of the technique and expand its capabilities towards the fabrication of 3D constructs. The first approach utilizes 3D printing to synthesize new quasi-3D, prepolymer molds—a significant advancement from the 2D-patterned molds previously utilized. Additionally, 3D printing improves the technique's scalability, reduces production time and cost, and enables access to 3D structuring capabilities. While we had previously only demonstrated the technique on silk fibroin, here we find that our technique readily adapts to other physically-crosslinked polymers (alginate and cellulose respectively). Specifically, the modulation of a simple solvent treatment step can tune the nanostructure of biopolymers, further impacting material characteristics. Lastly, we find that introduced

nanowires can be permanently forced into alignment within our processed materials, enabling the inclusion and tuning of additional material properties. Our second approach explores the combination of MDA, as a post-processing step, with fluidic infiltrative assembly (FIA) to fully extend this technique into the 3D space. Here, the sacrificial, fluidic molds employed in FIA act in place of previously 2D/quasi-3D prepolymer molds to constrain polymerized hydrogels and induce solvent-mediated anisotropy. After dissolution, the resulting architectures exhibit clear nanostructural alignment, programmed by the geometric constraints of the mold geometry. Taken together, these versatile approaches enable the synthesis of hierarchical biomaterial constructs, with tunable nanostructure and function, that are more reminiscent of natural tissues.

3.1 Materials & Methods

The following sections list the materials and experimental methods used to conduct the research described in Sections 3.2 and 3.3.

3.1.1 Materials

Cellulose, tetrabutylammonium fluoride (TBAF), dimethyl sulfoxide (DMSO), toluene, calcium carbonate ($CaCO_3$), and D-(+)-gluconic acid δ-lactone (GDL) were purchased from Millipore Sigma. Isopropanol (IPA) was purchased from Fisher Scientific, sodium alginate (Na-ALG), viscosity 80 – 120 cp) from FUJIFILM Wake Pure Chemical Corporation, 1,1,1,3,3,3-hexafluoro-2-propanol (HFIP) from Matrix Scientific, 3DM-ABS resin from 3DM Inc., and ethanol (EtOH) was purchased from Gold Shield Distributors. All chemicals were

purchased and used without further purification. All aqueous solutions were prepared using deionized water (DI) unless otherwise stated.

3.1.2 Methods

Hydrogel Synthesis

For a 0.5% - 2% (w/v) Ca-ALG hydrogel: A 1 mL aliquot of a 0.5% – 2% Na-ALG stock solution in DI was added to a microcentrifuge tube. To the tube, $CaCO_3$ (0.0045 g, 45 mM final concentration) and GDL (0.016 g, 90 mM final concentration) were added sequentially, mixing vigorously after each addition. The solution was used immediately upon mixing. At room temperature, these amounts of $CaCO_3$ and GDL take 24 hours to form a complete gel.

For 0.5% - 2% (w/v) cellulose hydrogel: 0.15 g of TBAF and 0.05 – 0.2 g of cellulose were added in sequence into 10 mL DMSO. The solution was stirred until all the cellulose dissolved into solution. At room temperature, the cellulose hydrogel takes 12 hours to form a solid-state gel.

3D Printing and Post-Processing

A 3D part for eventual soft lithography was modelled in SolidWorks®, outputted as a standard tessellation file (STL), and modified by Autodesk Netfabb. The file was uploaded, sliced, and printed in a liquid crystal display stereolithography (LCD-SLA) 3D printer (Phrozen). After printing, the 3D parts were removed from the build platform and placed in an IPA bath for 15 minutes. The parts were then irradiated with UV-light for 15 minutes, after which they were ready to use.

Soft Lithography

Master molds for soft lithography were made by adhering 3D-printed parts to a petri dish using a cyanoacrylate super glue. The adherent parts were then coated in a thin layer of 5% (w/v) polystyrene in toluene and allowed to dry completely. A 10:1 mixture of polydimethylsiloxane (PDMS) base and crosslinker (Sylgard 184; Krayden) was poured into the petri dish and placed in a desiccator to remove small bubbles. The PDMS-filled petri dish was then placed in an 80 ℃ oven for one hour to allow for complete curing of the silicone polymer. After fully curing, the PDMS mold was carefully extracted from the petri dish and stored for later use.

Mechanical-Directed Assembly

Hydrogel precursor solution was infiltrated into prefabricated, PDMS molds with small columns of PDMS to serve as "anchors" and allowed to gel completely. The resulting gels were treated with an initial concentration of EtOH (30, 50 or 100%) for 24 hours to induce gel contraction and nanofibrillar alignment in the direction of the anchor-defined strain. The gels were then transferred into 100% EtOH for 3 days to remove all the water remaining in the gel network. To convert hydrogel samples into aerogels, the samples were dried in a critical point dryer (Leica EM CPD300) to preserve the structure of the nanofibrillar networks.

Fluidic Infiltrative & Mechanically-Directed Assembly

0.5% alginate solution (0003 g/mL, 30 mM $CaCO_3$) was infiltrated into sacrificial fluidic molds and allowed to gel completely. The resulting gels were initially treated with 25% EtOH for 24 hours to induce gel contraction and nanofibrillar alignment in accordance with the mold geometry. The molds were dissolved in accordance with the protocol described in Section 2.1 and the resulting gels were placed in either DI to recover or 100% EtOH to prepare the samples for optional critical point drying. To obtain 3D aerogel samples, fully contracted, 3D hydrogels were dried in a critical point dryer (Leica EM CPD300) to preserve the structure of the complex nanofibrillar networks.

COMSOL Simulations

Mechanical simulations were performed utilizing COMSOL Multiphysics version 5.6 including two-dimensional and three-dimensional solid mechanics with the application of line or area translation at nodes of mechanical tension. The hydrogel analog was set as an elastic material with properties as follows:

- Young's Modulus = 1.5 MPa
- Poisson's Ratio = 0.11
- Density = 1.0 kg/m3

For the studies, the bottom plane of the geometry was fixed and a prescribed displacement was applied in the directions of the anchors. The prescribed displacements for the beam studies were 0.3 cm, 0.5 cm, and 0.7 cm and the displacement for the pyramid studies was 1.0 cm.

Percent Contraction Measurements

The percent contraction of cellulose and alginate hydrogels was quantified by measuring the width of hydrogel beams at the midpoint between the anchors, before and after solvent exposure, using the following equation:

$$Contraction\ (\%) = \frac{(Contracted\ Width)}{(Original\ Width)} \times 100$$

Polarization Microscopy

Brightfield images of hydrogel and aerogel samples were taken between two 2-inch linear polarizers (400 – 700 nm; Thorlabs Inc.) on a compound microscope (AmScope). The polarizers were rotated independently to block incident light and reveal the birefringence of the samples. A Nikon D3400 digital single-lens reflex (DSLR) camera with an attached AmScope camera adapter was utilized to capture the sample images through the eyepiece of the microscope. The birefringent color patterns present in the samples were analyzed using a Michel-Levy chart, which correlates the exhibited colors (retardation) with quantified differences in indices of refraction using the following equation:

$$Birefringence = \frac{Light\ Retardation}{Sample\ Thickness}$$

Birefringence data was analyzed using a Michel-Levy chart, which correlates exhibited colors with quantified differences in indices of refraction.

Dynamic Mechanical Analysis (DMA)

Alginate and cellulose type IV dumbbells conforming to the American Standards for Testing and Materials (ASTM) International standards were made following the casting and directed-

mechanical assembly method outlined within this paper. Stress/strain curves for the hydrogels and aerogels were obtained using a DMA Q800 (TA Instruments) equipped with a tensile clamp and set with a strain rate of 3 %/min.

Infrared Thermography

We utilized the same testing facility and methods described in Section 2.1.2 to obtain Fourier Transform Infrared (FTIR) spectra for alginate and cellulose hydrogels.

Scanning Electron Microscopy

Scanning electron microscopy (SEM) was performed using an FEI Magellan 400 XHR Scanning Electron Microscope (Field Electron and Ion Company). Aerogel samples were mounted onto SEM-compatible stubs using conductive adhesive tape. The samples were then sputter-coated with a thin layer of iridium to enhance conductivity and minimize charging effects during imaging. Once coated, the samples were transferred to the microscope's vacuum chamber and secured to the stage. During imaging, the SEM was operated in high-vacuum mode to maintain optimal imaging conditions and prevent contamination of the electron column. Image acquisition and processing were carried out using integrated software, enabling real-time adjustments to focus, magnification, and contrast.

Resistance Measurements

Silver nanowire-doped, alginate aerogels were placed on square copper sheets attached to plastic coverslips and covered in a gallium-indium eutectic to maximize contact between the

material and the metal. The resistance between the two copper sheets were measured using a multimeter (DM03B Digital Multimeter, TACKLIFE).

Conductivity Measurements

The previously measured resistance of silver nanowire-doped, alginate aerogels were used in the following equation along with the cross-sectional areas of isotropic and anisotropic samples to determine the conductivity of the samples.

$$Conductivity\ (\sigma) = \frac{length}{Resistance * Cross - Sectional\ Area}$$

Nanowire Angle Quantification

Brightfield images of nickel nanowire-doped, alginate hydrogels were subjected to a Hough Transform in Python. The total number of available angles from the generated output lines (-180° to 180°) were reduced by taking their absolute value and subtracting 90° from angles greater than 90°. The reduced angles were binned into nine categories in 10° increments (from 0° to 90°) and summed to quantify the total lines within a 10° bin. The resulting data was presented as a radial histogram.

3.2 Quasi-3D Anisotropy via Mechanically-Directed Assembly

Mechanically-directed assembly involves several material processing stages that combine to yield hierarchical materials with multiple degrees of tunability in porosity, anisotropy, and shape. Generalized steps include: 1) Creation of an open-faced, microfluidic silicone mold containing embedded mechanical structural features, 2) Infiltration of

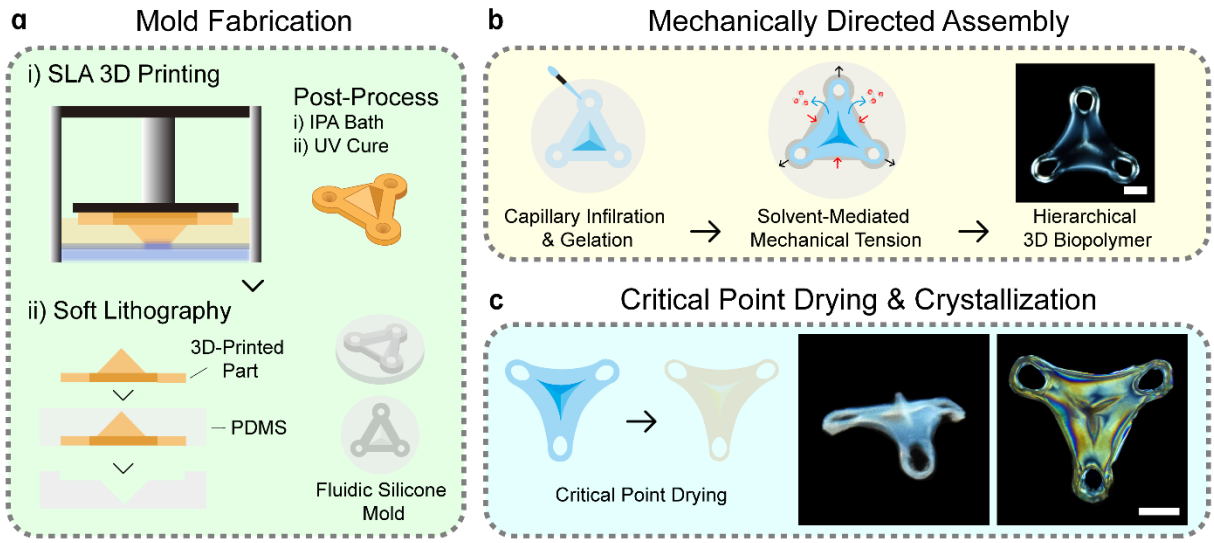

Figure 3.2 | Schematics Describing the Fabrication of Hierarchical Hydrogel/Aerogel Structure. a) i. 3D mold fabrication SLA based 3D printing and post processing. ii. Soft lithography using the 3D printed, 3D molds as the master and PDMS as material for the negative molds. b) Schematic of the directed mechanical assembly for cellulose and alginate hydrogels/aerogels. c) Depiction of the optional critical point drying step, the resulting aerogel, and the birefringence the process unlocks. (Scale Bars = 3 mm)

hydrogel prepolymer solution (solvent, polymer units, crosslink mediator, nanomaterials) followed by polymerization, 3) Controlled hydrogel contraction, which elicits tunable mechanical stimuli on the polymer, and 4) Completion of physical cross-linking and optional critical point drying. Anchor points defined during the molding step induce well-defined mechanical forces on polymers, ultimately leading to nanostructural anisotropy within resultant materials. This strategy enables tunable synthesis of hierarchical materials through the engineering of mold, anchor point geometry, and solvent immersion treatment (Figure 3.2).

For this approach, we study several important expansions to this technique. The first is the use of SLA 3D printing to form high-resolution master molds (Figure 3.2a). These are used to demold our open-faced silicone (polydimethylsiloxane, PDMS) microfluidic channels. The use of 3D printing allows materials with 3D facets to be produced (an example includes the pyramidal structure in Figure 3.2). Furthermore, this allows mechanical strain to pattern

and distribute in 3D. This manipulation of nanoscale anisotropy in three dimensions is a new layer of control to our technique. SLA printers exhibit the highest resolution of 3D printing modalities (in addition to smoother surfaces) and are used herein. We utilized a low-cost, SLA 3D printer (Phrozen, Taiwan) for master mold fabrication. This printer possesses a maximum resolution of 47 μm in the x- and y-directions and 10 μm in the z-direction. The 3D-printed mold is spun-coat with polystyrene to facilitate PDMS polymerization and subsequent demolding. This polystyrene layer is critical in preventing the polymerization inhibition that often occurs on the surface of an SLA product [146], [148], [198], [199]. While polymers can be synthesized directly in 3D-printed structures, we found PDMS to be a preferable biopolymer molding material because synthesized biopolymers separate more readily from silicone.

We expanded MDA to two additional physically-crosslinked biopolymers (cellulose or alginate, respectively). As noted in Chapter 1, cellulose is the most abundant organic material on our planet, and great effort has been placed in the regeneration of functional, synthetic cellulose materials [200], [201]. Natural cellulose is organized into a series of crystalline and amorphous domains that physically crosslink into anisotropic fibers. Alginate, like cellulose, is a polysaccharide that physically crosslinks through chelation of carboxylic acid groups by di- or trivalent ions. We found both polymers to readily adapt to our technique. Cellulose or alginate prepolymer solutions are infiltrated into our silicones molds and allowed to cross-link into solid gels. For cellulose, hydrogels were formed by adding cellulose powder to a mixture of dimethyl sulfoxide (DMSO) and tetrabutylammonium fluoride (TBAF). These are initially gelled in a DMSO atmosphere to minimize evaporation from our small fluidic channels. For alginate, we used a protocol that enables in-situ polymerization of the material

through slow dissociation of calcium carbonate ($CaCO_3$) mediated by an acid [202], [203]. Alginate is commonly crosslinked by direct immersion of prepolymer solutions in calcium chloride [204], [205], [206], [207]. While this crosslinking approach works with our technique, we found this generated unwanted stress in the polymer due to lack of homogeneity during gelation. We first dissolved sodium alginate alongside calcium carbonate in water, followed by addition of gluconic acid to control the release of calcium into the alginate prepolymer. After infiltration of alginate prepolymer solution into our fluidic molds, the molds were placed in a humidity chamber and the alginate allowed to gel.

3.2.1 Tuning Biopolymer Nanostructural Anisotropy

Nanostructural anisotropy is engineered throughout our molded polymers through the introduction of controlled mechanical strains that propagate throughout materials. Important to this process are anchorages defined during molding. These pin the polymer so that it cannot deflect at these fixed locations during the introduction of mechanical strain (Figure 3.2b). Anisotropy within materials is sometimes created by stretching, this generates tensile stresses that can elongate and align fibers. While this approach could potentially be applied to molded polymers, such tensile stress is difficult to apply beyond a single dimension or for structures of scaling complexity. As an alternative, one key strategy we introduced in our previous study on silk biopolymer was the utilization of controlled treatments of our molded biopolymer within a polar solvent mixture (ethanol-water) [141]. Such treatments induced uniform material contractions that occurred irrespective of structural complexity. This then led to engineered tensile strain via anchorage points defined

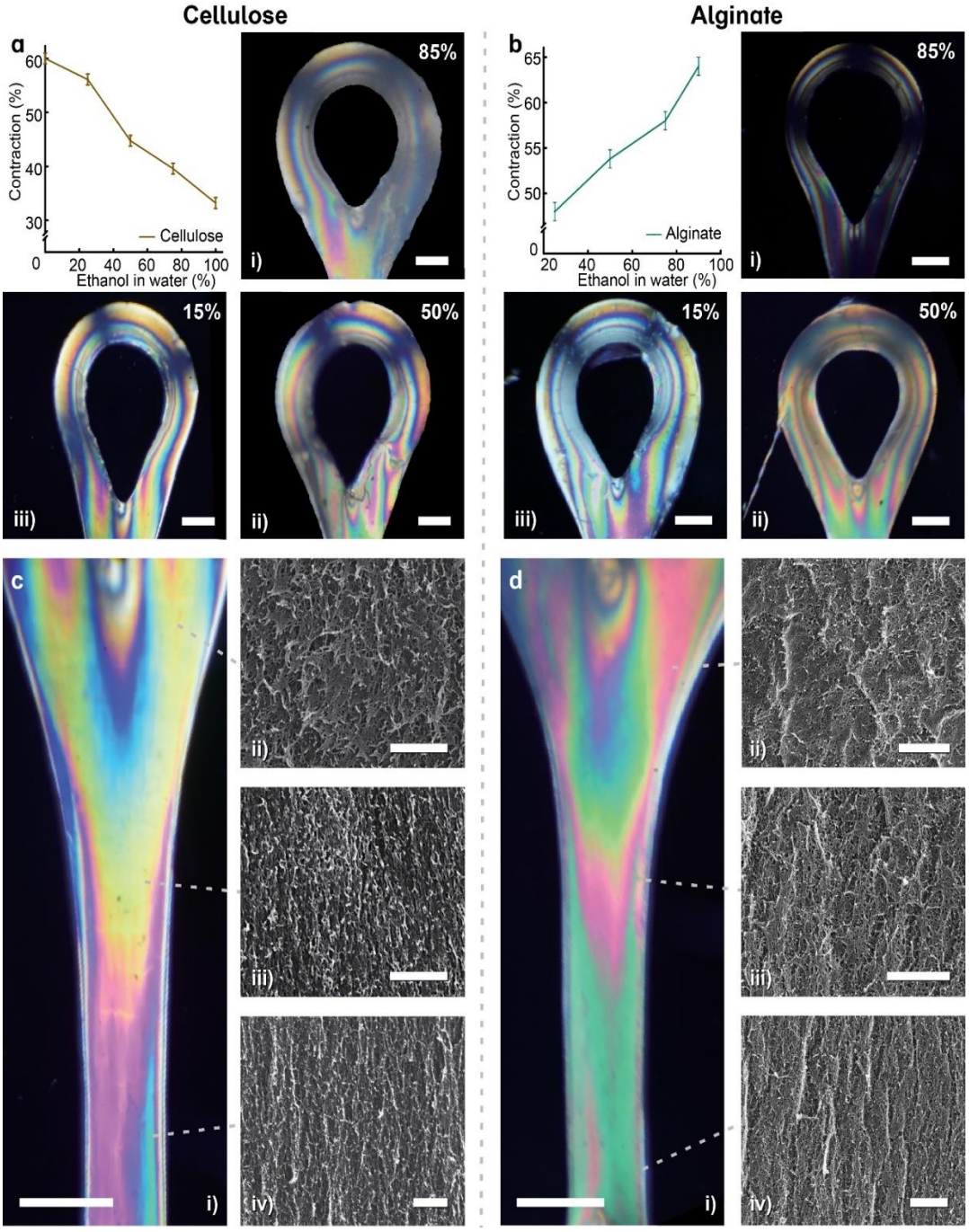

Figure 3.3 Birefringence and Contractile Properties of 2D Alginate and Cellulose Hydrogels. a) Contractile properties of alginate hydrogels when subjected to varying ethanol percentages. i–iii) Representative images of the birefringence of alginate hydrogels at 15%, 50%, and 85% ethanol in water. b) Quantification of contractile properties of alginate hydrogels when subjected to varying ethanol percentages. i–iii) Representative images of the birefringence of alginate hydrogels at 15%, 50%, and 85% ethanol in water. c) i. Birefringence of a cellulose hydrogel. ii –iv. SEM images of the nanofibrillar structure of the corresponding cellulose aerogel at various points along the gel. d) Birefringence of an alginate hydrogel. ii –iv. SEM images of the nanofibrillar structure of the corresponding alginate aerogel at various points along the gel. (Birefringence Scale Bars = 500 μm; SEM Scale Bars = 1 μm)

during molding. Herein we investigate how simple polar solvent treatments can be applied

to cellulose or alginate to tune the contraction of these biopolymers. We broadly expect this approach to work for any water-based polymer, as subjecting such polymers to a weaker polarity solvent (such as ethanol) will induce polymer-chain organization/assembly.

We studied the effect of polar solvent treatments on the final contraction of biopolymers cellulose or alginate (Figure 3.3a, b). In these experiments, materials were first exposed to a specific treatment of polar solvent ranging from 15 % to 85 % in water (24 h), before being exchanged in 100 % ethanol for final material preparation. Here, we are most interested in the final contraction of the material after final exchange in the 100 % ethanol. Cellulose behaved similarly to our previous studies on silk biopolymer in that extended treatment in lower concentrations of ethanol (followed by final exchange in 100 % ethanol) resulted in greater final material contraction (Figure 3.3a). Alginate experienced the opposite effect, where a higher final material contraction was achieved by extended treatment in a higher concentration of ethanol (Figure 3.3b). We interpret this response as resulting from the partial folding of the alginate chains, which become more pronounced from rapid treatment in high ethanol concentrations [208]. We have found that hydrogels at this point (formed by exchanging polymers back into water) permanently exhibit minor birefringence

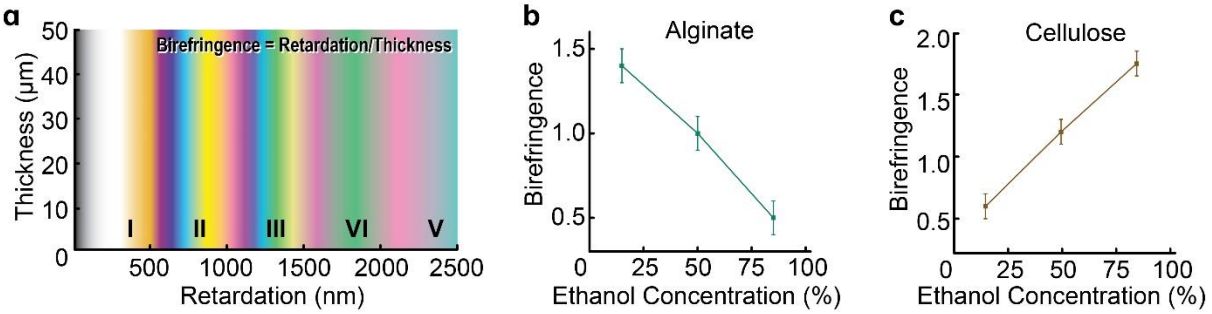

Figure 3.4 | Quantification of Birefringence for Alginate and Cellulose Aerogels. a) Representation of a Michel-Levy chart used in the analysis of sample birefringence. b) Birefringence of alginate aerogels near the anchors as related to the initial concentration of ethanol used in the mechanically directed assembly process. c) Birefringence of cellulose aerogels near the anchors as related to the initial concentration of ethanol used in the mechanically directed assembly process.

indicative of anisotropy within the material (Figure 3.4). This is in addition to strain-dependent mechanical properties to be discussed later. This nanostructural anisotropy is permanent—we attribute the stability of this reorganization to the continued physical crosslinking of polymer chains as these processes typically occur over several days [209].

While this process can end here to create anisotropic hydrogels, we can perform an optional critical point drying (CPD) step to convert our hydrogels into aerogels. This carefully controlled dehydration process preserves the morphology of the material nanostructure. Accompanying this step is the appearance of vibrant birefringent patterns that were previously obscured by the surrounding water medium (Figure 3.2c). Under polarization microscopy, anisotropic samples exhibit colorful birefringent patterns that can be cross-referenced with the Michel-Levy Interference chart [210]. This denotes greater differences in the indices of refraction along perpendicular planes (and is indicative of higher orders of material anisotropy) [211], [212]. The birefringence of synthesized aerogel structures (with anchored beams) subjected to various solvent treatments are shown in Figure 3.3c and d. Molded biopolymers that were subjected to higher contraction-driving solvent treatments exhibit more intense, higher order birefringent patterns. The Michel-Levy chart is further used to characterize the anisotropy generated by our solvent treatments on cellulose or alginate. In addition, patterns of birefringence within synthesized structures map along patterns of strain created during our processes. Within an anchored beam, the largest induced strains occur at the center of the construct (halfway between anchor points), with weaker strain close to the anchorages. Corresponding to this, birefringence of constructs follows directly along these patterns of stress/strain, with higher order birefringence at the

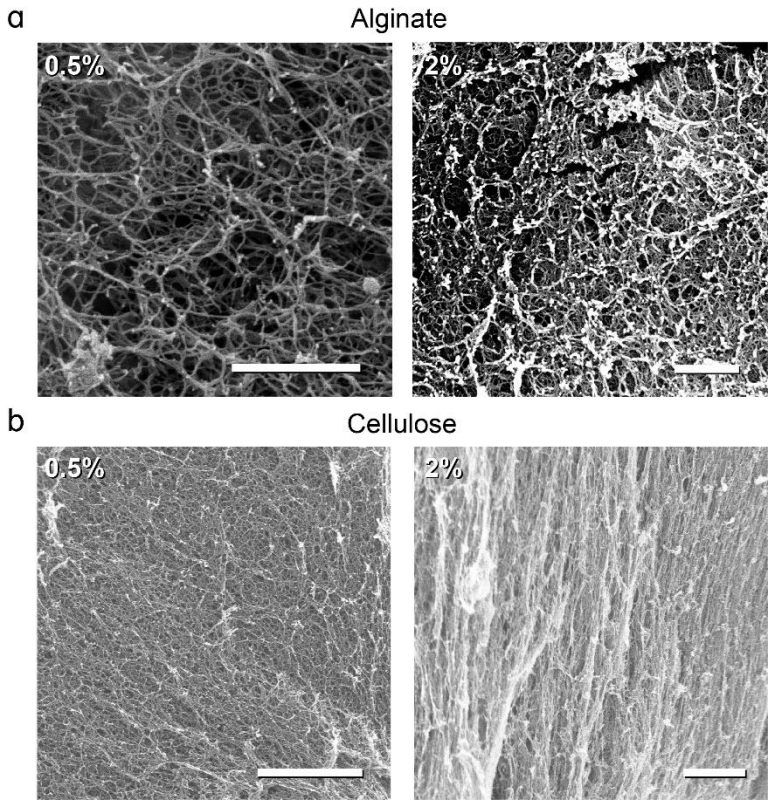

Figure 3.5 | Alginate and Cellulose Morphology. Scanning electron microscopy (SEM) images of a) 0.5% and 2% alginate hydrogels (Scale Bar = 500 nm) and b) 0.5% and 2% cellulose hydrogels (Scale Bar = 3 um).

center of the beam and weaker close to the anchor points. This coordination occurs with all our studied biopolymers (silk, cellulose, alginate).

The origin of this birefringence can be further assessed via scanning electron microscopy (Figure 3.3cii-iv, dii-iv). The SEM images further validate the nanostructural alignment of the materials, mapping to observed birefringence intensity. The middle portion of the gel experiences the highest strain and correspondingly appears the most structurally aligned in SEM images. We further found that nanostructure can be additionally controlled by modulating the initial percentage of cellulose or alginate in the prepolymer solution. This tunes the density of synthesized biopolymers, which exhibit structural and birefringence changes in accordance with differing porosities (Figures 3.5 & 3.6).

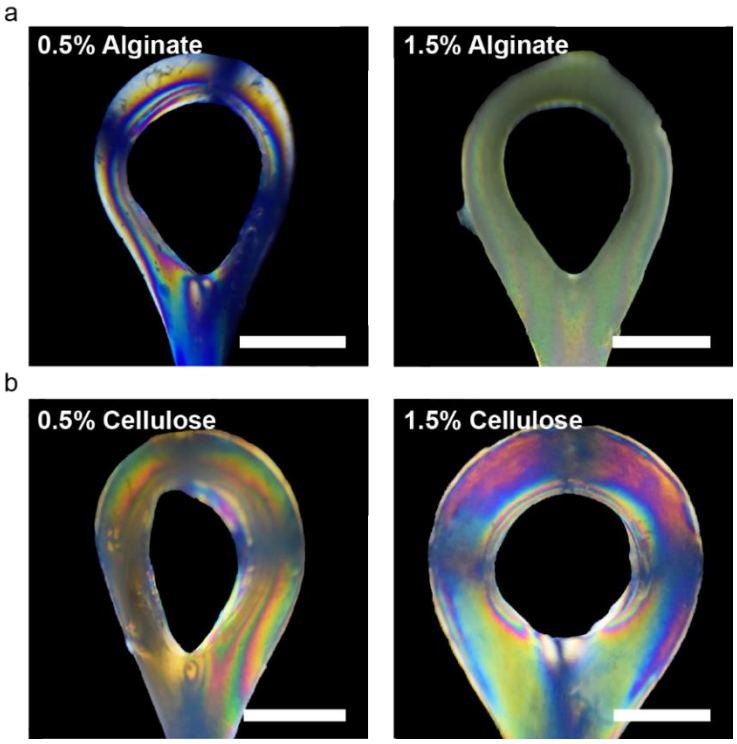

Figure 3.6 | Birefringence of Varying Biopolymer Concentration. Birefringence of a) 0.5% and 1.5% alginate aerogels and b) 0.5% and 1.5% cellulose aerogels under equivalent contraction parameters. (Scale Bar = 1 mm)

Leveraging the multidimensionality of our improved technique, we additionally extended our molding technique to create nanostructured, 3D pyramidal constructs. This structure is bounded by anchor points in 2D that, upon molded polymer contraction, propagate 3D strains throughout the depth of the final biopolymer construct (Figure 3.7a, b). Patterns of birefringence in final synthesized materials agreed with stress/strain simulations completed in COMSOL (Figure 3.7a) and demonstrate that patterns of anisotropy were encoded in 3D (Fig 3.7aiii). Structural anisotropy was further validated using SEM, which showcases nanofibril alignment matching simulation and sample birefringence (Figure 3.7c, d). Our combination of predictive modeling, facile fabrication processes, and precise strain control may enable the creation of a variety of tunable hierarchical biopolymers with 3D features.

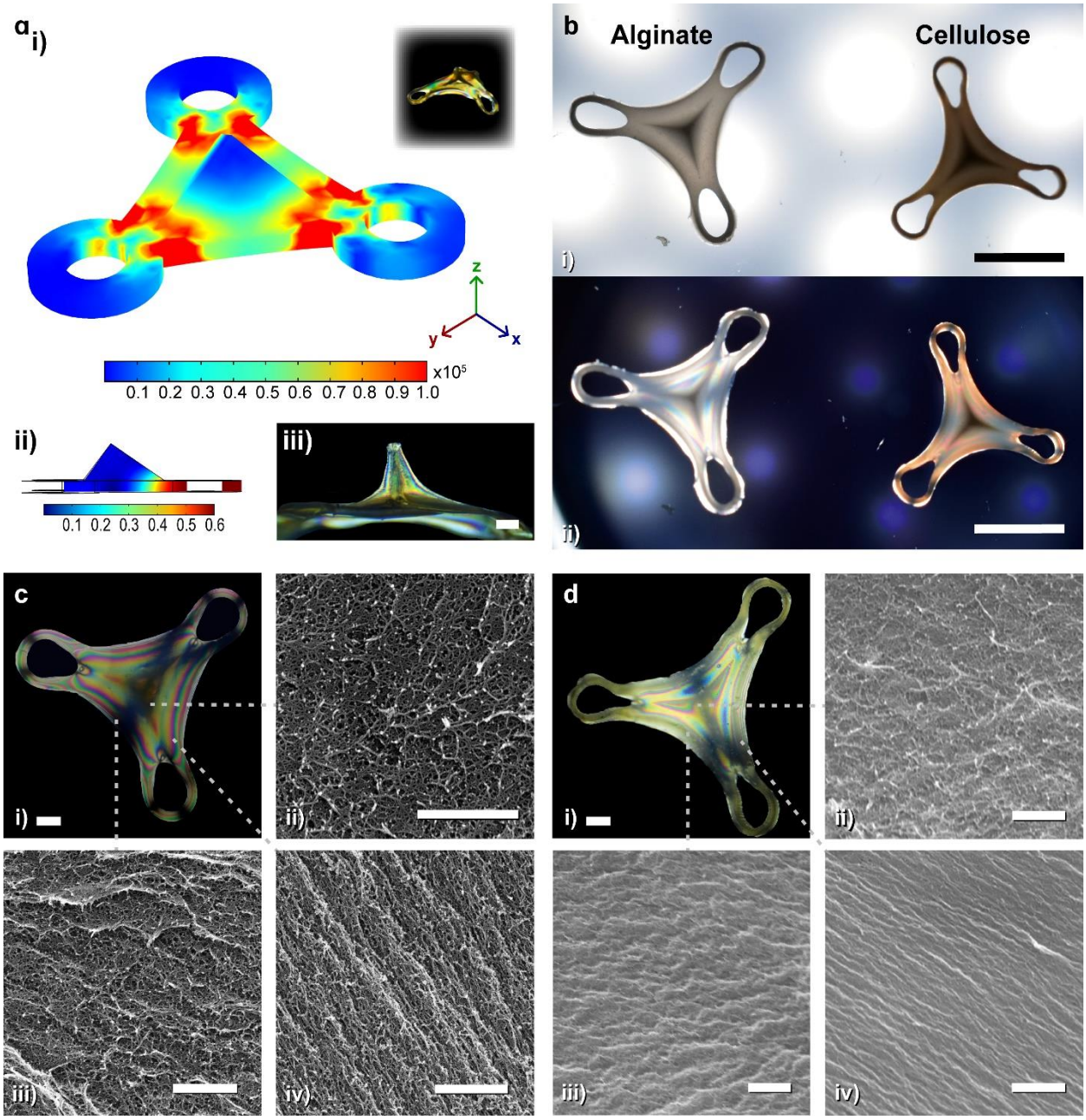

Figure 3.7 | Birefringence and Nanofibrillar Alignment of Alginate and Cellulose Hydrogels. a) i) Three-dimensional strain simulation of a 3D structured hydrogel anchored with silicone rods presented alongside an isometric-view of the corresponding aerogel birefringence. ii) Side-view of the 3D structured hydrogel. iii) Side-view of the aerogel birefringence. (Scale Bar = 1mm) b) i) Top-down view of 3D structured alginate and cellulose aerogels without linear polarization of light. ii) Birefringence of 3D structured alginate and cellulose aerogels (Scale Bars = 5 mm). c) i) Top-down birefringence of an alginate aerogel (Scale Bar = 1 mm). ii –iv) Representative SEM images of the nanofibrillar alignment within the gel corresponding to areas of higher order birefringence. d) i) Top-down birefringence of a cellulose aerogel (Scale Bar = 1 mm). ii –iv) Representative SEM images of the nanofibrillar alignment within the gel corresponding to areas of higher order birefringence. (SEM Scale bars = 1 μm)

3.2.2 Functional Nanofibrillar Structures

Lastly, we studied how various physical properties of synthesized materials could be modified through our process. We found that cellulose and alginate hydrogels and aerogels exhibited strain-dependent increases in elastic modulus (Figure 3.8a, b). All hydrogels and aerogels also generally exhibited improvements in toughness due to our process. One caveat is specifically the aligned cellulose hydrogel, whose strain-to-break was lower than their unaligned counterparts. These aligned cellulose hydrogels thus exhibited lower overall toughness despite possessing higher Young's modulus.

As such improvements in mechanical behavior are to be expected with our process, we additionally attempted to control the electronic/magnetic properties of our materials via the introduction of anisotropic nanomaterials. Anisotropic nanomaterials, such as nanowires, are subjected to directional torques during the introduction of tensile stresses. It is known that conductivity of nanowire-doped materials modulate as they are strained and nanowires orient along strain direction [213]. We sought to study whether our process could permanently affix such nanomaterials along encoded directionalities, allowing us to further tune the functionalities of our nanostructured materials (Figure 3.8c). We specifically designed constructs with two separate sections, one that is aligned and another that is not, to ensure that each section experiences the same contraction conditions. When subjected to our technique, silver nanowires (doped in the alginate prepolymer solution at 20 g/L) aligned in the direction of strain along with the nanostructure of the alginate gels (Figure 3.8d, e). The alignment of magnetic nickel nanowires could also be manipulated with our technique, offering an alternative to traditional alignment approaches that typically require

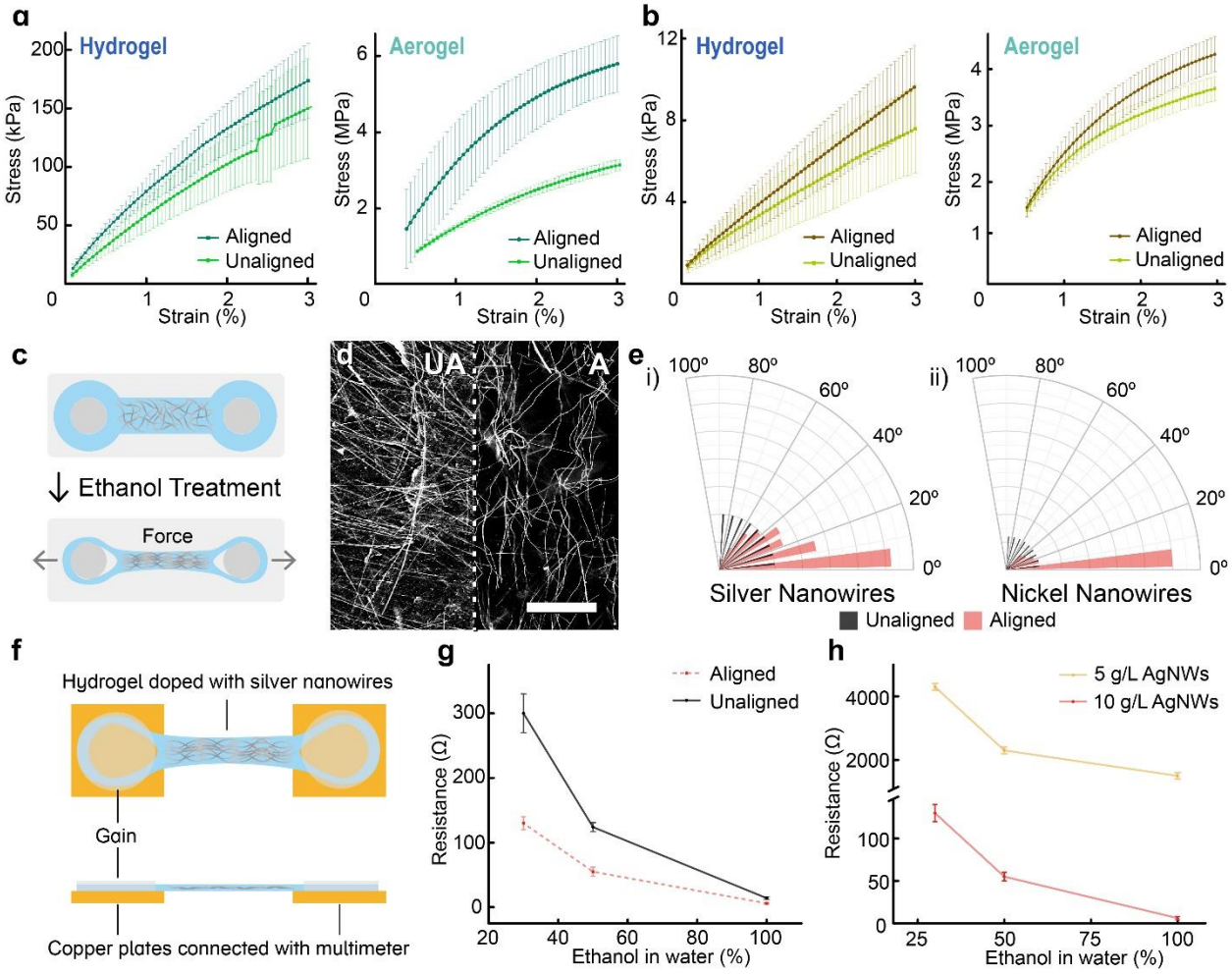

Figure 3.8 | Mechanical and Functional Characterization of Alginate and Cellulose Hydrogels/Aerogels. a) Partial stress versus strain data for unaligned and aligned alginate hydrogels/aerogels. b) Partial stress versus strain data for unaligned and aligned cellulose hydrogels/aerogels. c) Schematic detailing how dopants are aligned within a gel structure during the directed mechanical assembly process. d) SEM images comparing the alignment of silver nanowires within unaligned and aligned alginate gels (Scale Bar = 10 μm). e) Radial histograms comparing the normalized number of i. silver and ii. nickel nanowires in unaligned and aligned hydrogels by their angle relative to the strain direction. f) Schematic depicting how the resistance within nanowire-doped, alginate hydrogels were measured. g) Resistance in unaligned and aligned alginate hydrogels as a function of ethanol in water concentration. h) Resistance in aligned alginate hydrogels with two different silver nanowire concentrations as a function of ethanol in water concentration.

the application of external magnetic fields (Figure 3.8e). The alignment of silver nanowires within our synthesized materials yielded improvements in the conductivity of our constructs (Fig. 3.8g, h). In particular, the resistance of doped beam structures drops below 100 Ω when aligned, indicative of potential utility of our porous materials in electronic systems. Stretched materials nominally experience an increase in resistance due to the geometric piezoresistive

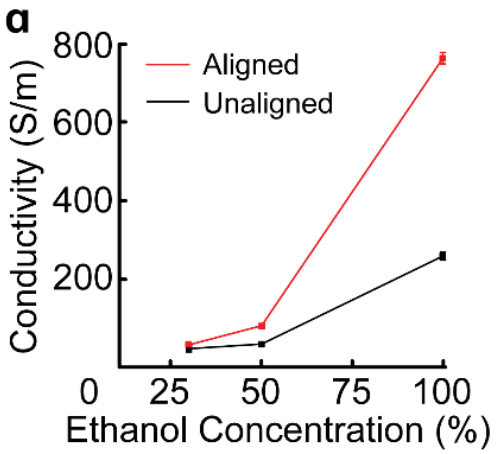

Figure 3.9 | Anisotropy-Dependent Conductivity. Conductivity measurements of aligned and unaligned alginate hydrogels as related to the initial ethanol

effect; however, we instead saw a stark reduction. This is indicative of a large increase in the conductivity of the aligned samples due to the silver nanowire alignment. Furthermore, we can tune the extent of the conductivity increase by modulating the initial ethanol concentration and the extent of nanowire alignment (Figure 3.9). These results highlight the versatility and potential utility of this approach, which may be used to create tightly regulated materials with varying physiochemical properties.

3.3 Multimodal Fabrication of 3D Anisotropic Gradients

Extending MDA as an optional post-processing step to FIA requires only slight processing changes to the techniques. After the gelation of a molded, 3D hydrogel, the gel can be subjected to solvent-mediated contraction to induce tunable mechanical stimuli on the construct prior to mold dissolution (Figure 3.10a). The sacrificial fluidic mold employed in FIA constrains the gel as it uniformly contracts, acting as 3D analogs to the open-faced silicone molds used prior. Once the desired contraction/anisotropy has been achieved, the hydrogel is released by the dissolution of the mold as described in Sections 2.1 and 2.2. Following dissolution, the resulting anisotropic hydrogel can be either placed in DI to recover from the previous processes or, optionally, it can be subjected to CPD and turned into a 3D aerogel (Figure 3.10b). Drying of the gels reveals clear birefringent patterns that indicate

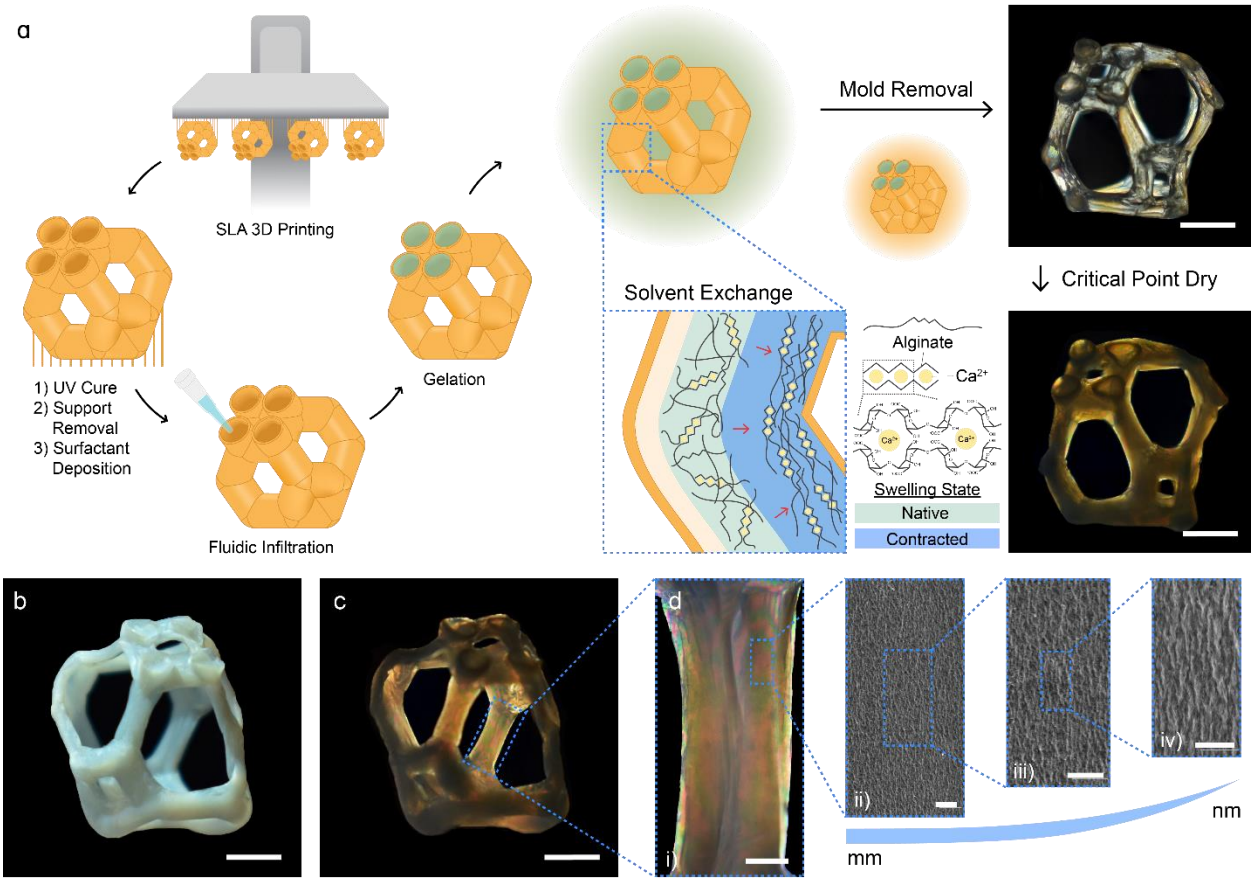

Figure 3.10 | Induction of 3D Anisotropic Gradients through Multimodal Assembly Techniques. a) Schematic detailing the initial infiltrative assembly process for alginate hydrogels followed by solvent-mediated, in situ contraction. After contraction, the mold is dissolved and either left in DI to recover or placed in 100% for complete dehydration prior to critical point drying. b) 3D structure and c) its corresponding birefringence. d) Close-up image of aa birefringent, structural beam and the anisotropy of the nanofibrillar architecture as shown by SEM. Scale Bars for a), b), and c) are 3 mm. Scale bars for d) i, ii and iii, and iv are 500 µm, 2 µm, and 1 µm, respectively.

successful induction of nanostructural anisotropy which can be further validated by SEM imaging (Figure 3.10c, di-iv).

To better visualize the anisotropy within these constructs, we created a three-winged structure, dubbed the "tri-wing", with defined anchor points and mold restrictions to induce planar anisotropies in 3D (Figure 3.11a). The structure was designed as a vertically-anchored, columnar body with three evenly-spaced, planar wings constrained by two anchors at the tips of each wing. During the MDA process, the anchors constraining the central body would induce alignment vertically while also acting as tertiary constraint for

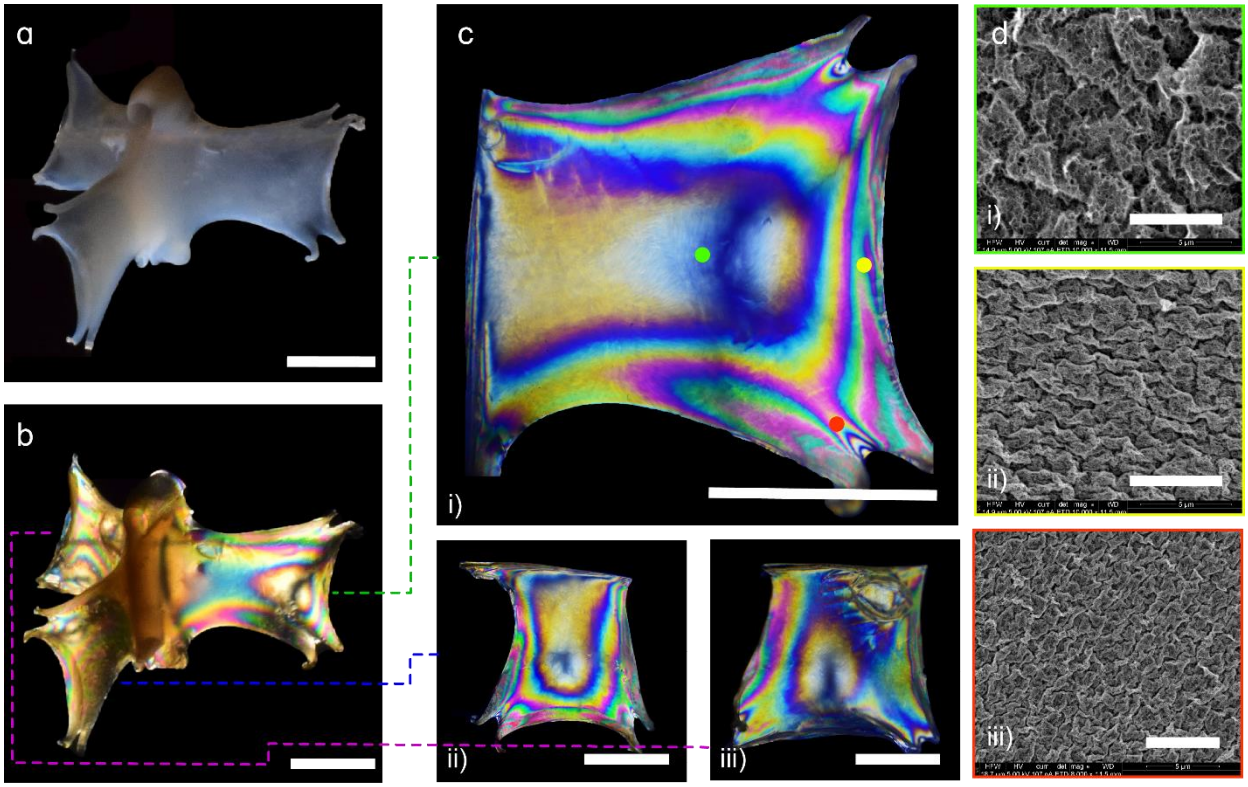

Figure 3.11 | Complex Planar Anisotropy in a 3D "Tri-wing" Aerogel. a) Tri-wing aerogel with broken anchors post-contracted and mold dissolution. b) Birefringence patterns present throughout the structure, captured using two visible light polarizers. c) i-iii) Birefringent patterns on each wing. d) i-iii) SEM images corresponding to three different locations on the gel shown in ci (e.g., green dot to green bounding box in di). Scale bars for a), b), and c) i-iii) are 5 mm. Scale bars for d) i-iii) are 5 μm.

each planar wing. The result is a highly birefringent, alginate aerogel with clearly defined 2D anisotropic gradients on the wings and in 3D overall (Figure 3.11b).

While the wings shared similarities in their birefringence patterns, the way these patterns manifest on each wing is unique, likely due to process inconsistencies resulting from the merging of the two techniques (Figure 3.11ci-iii). Despite these inconsistencies, we obtained visually stunning birefringent patterns on each wing and confirmed that the magnitude and order of the birefringence were a result of the architectural arrangement of the nanoporous network (Figure 3.11di-iii).

3.4 Concluding Remarks

Advantages provided by both mechanically-directed assembly and fluidic infiltrative assembly have enabled the generation of complex anisotropic gradients in porous scaffolds with few restrictions in biomaterial selection and accessibility. Our extensions have allowed us to explore how they can synergize to synthesize nanoporous biopolymers with engineered, nanostructural anisotropy and functionality. These expansions enable greater scalability in our technique, multidimensionality in control, and further adaptability to a wide range of biopolymers to facilitate tissue scaffold development.

CHAPTER 4

Insights into Future Work and Conclusions

In this dissertation, we have detailed the development of fluidic infiltrative assembly (FIA), a versatile fabrication technique that leverages coordinated injection molding strategies with indirect 3D printing to structure a wide assortment of biomaterials. Capitalizing on commercially-available equipment and reagents, FIA offers an alternative, cost-effective platform for tissue-specific, scaffold development. Furthermore, when combined with mechanically-directed assembly, FIA becomes an accessible, multimodal fabrication method capable of creating hierarchical structures with compositional and architectural gradients through flow-defined heterogeneity and multidimensional, indirect stress.

Despite these remarkable capabilities, FIA has inherited limitations associated with the dissolution of sacrificial material from indirect 3D printing. The use of stereolithography (SLA) 3D printing allowed for high-resolution, sacrificial molds whose features could easily transfer to gels as they undergo gelation. This light-based printing method creates a dense polymer network of covalent crosslinks upon exposure to light resulting in strong structures with high fidelity. Fidelity aside, this dense network of covalent crosslinks present in most commercial resins are difficult to degrade/dissolve and pose a problem for our "plug-and-play" approach of using commercial equipment/reagents for tissue scaffold development. The resin/solvent combination identified in this dissertation was more fortuitous than it was intentional as it was based on a misunderstanding encouraged by resin manufacturers'

propensity for likening new resin products to well-known thermoset polymers. Nevertheless, exploring alternative sacrificial materials for use with FIA is a viable means of addressing this limitation moving forward.

Integration with mechanically-directed assembly is a great step forward in the fabrication of complex, tissue-like structures; however, the solvent-mediated contraction of a material needs to be directly correlated with the resulting anisotropy to be properly programmable. This is particularly important as the technique extends into quasi-3D, 3D, or four-dimensional (4D) spaces where the variables that can affect a structure's anisotropy significantly increase. Open-mold, 2D characterization of a specific material may be sufficient to establish connections between the process and the result though it may also yield inconsistent results due to variances in ambient conditions or a user's process. The use of simple sacrificial molds could be a straightforward method for establishing these relations under more controlled conditions if the mold dissolution does not interfere with the resulting anisotropy, which, in the case of HFIP, it may.

At its core, FIA is not intended to be the solution to the long-term problem of tissue injury and disease, but it can be part of the solution and can aid in addressing limitations in access, costs, and biomaterial availability. FIA's likely compatibility with a wide range of biomaterials, additives, and porogens may need verification, but its potential may make it an ideal companion method to more advanced fabrication techniques, especially in the assembly of multi-component or modular scaffolds. Further investigation into FIA's capabilities, immediate in vitro/in vivo applications, and compatibility with other fabrication methods are necessary to draw clear conclusions about the viability of this technique;

however, we believe that FIA and its combination with mechanically-directed assembly are potent tools that we can and should leverage towards tissue scaffold development.

References

[1] G. Cossu *et al.*, "Lancet Commission: Stem cells and regenerative medicine," *Lancet*, vol. 391, no. 10123, pp. 883–910, Mar. 2018, doi: 10.1016/S0140-6736(17)31366-1.

[2] T. A. Mir, S. Iwanaga, T. Kurooka, H. Toda, S. Sakai, and M. Nakamura, "Biofabrication offers future hope for tackling various obstacles and challenges in tissue engineering and regenerative medicine: A Perspective," *Int J Bioprint*, vol. 5, no. 1, p. 153, Dec. 2018, doi: 10.18063/ijb.v5i1.153.

[3] F. Akter, "What is Tissue Engineering?," in *Tissue Engineering Made Easy*, Elsevier, 2016, pp. 1–2. doi: 10.1016/B978-0-12-805361-4.00001-1.

[4] F. J. O'Brien, "Biomaterials & scaffolds for tissue engineering," *Materials Today*, vol. 14, no. 3, pp. 88–95, Mar. 2011, doi: 10.1016/S1369-7021(11)70058-X.

[5] F. Akter, "Chapter 2 - Principles of Tissue Engineering," in *Tissue Engineering Made Easy*, F. Akter, Ed., Academic Press, 2016, pp. 3–16. doi: 10.1016/B978-0-12-805361-4.00002-3.

[6] N. Almouemen, H. M. Kelly, and C. O'Leary, "Tissue Engineering: Understanding the Role of Biomaterials and Biophysical Forces on Cell Functionality Through Computational and Structural Biotechnology Analytical Methods," *Computational and Structural Biotechnology Journal*, vol. 17, pp. 591–598, Jan. 2019, doi: 10.1016/j.csbj.2019.04.008.

[7] P. A. Katili, A. P. Karima, W. Azwani, R. D. Antarianto, and M. M. Djer, "Application of Human Induced Pluripotent Stem Cells for Tissue Engineered Cardiomyocyte Modelling," *Regen. Eng. Transl. Med.*, vol. 9, no. 4, pp. 431–446, Dec. 2023, doi: 10.1007/s40883-023-00294-1.

[8] B. P. Chan and K. W. Leong, "Scaffolding in tissue engineering: general approaches and tissue-specific considerations," *Eur Spine J*, vol. 17, no. 4, pp. 467–479, Dec. 2008, doi: 10.1007/s00586-008-0745-3.

[9] "10.3: Human Cells and Tissues," Biology LibreTexts. Accessed: May 18, 2024. [Online]. Available: https://bio.libretexts.org/Bookshelves/Human_Biology/Human_Biology_(Wakim_and_Grewal)/10%3A_Introduction_to_the_Human_Body/10.3%3A_Human_Cells_and_Tissues

[10] P. E. Neumann and E. E. Neumann, "General histological woes: Definition and classification of tissues," *Clinical Anatomy*, vol. 34, no. 5, pp. 794–801, 2021, doi: 10.1002/ca.23741.

[11] P. E. Neumann and E. E. Neumann, "General histological woes: Encore. Tissues, please," *Clinical Anatomy*, vol. 36, no. 5, pp. 782–786, 2023, doi: 10.1002/ca.24031.

[12] Z. Wang *et al.*, "Tissue-specific engineering: 3D bioprinting in regenerative medicine," *Journal of Controlled Release*, vol. 329, pp. 237–256, Jan. 2021, doi: 10.1016/j.jconrel.2020.11.044.

[13] A. D. Bradshaw, "Chapter 12 - Regulation of cell behavior by extracellular proteins," in *Principles of Tissue Engineering (Fifth Edition)*, R. Lanza, R. Langer, J. P. Vacanti, and A. Atala, Eds., Academic Press, 2020, pp. 205–215. doi: 10.1016/B978-0-12-818422-6.00013-7.

[14] C. Frantz, K. M. Stewart, and V. M. Weaver, “The extracellular matrix at a glance,” *Journal of Cell Science*, vol. 123, no. 24, pp. 4195–4200, Dec. 2010, doi: 10.1242/jcs.023820.

[15] J. K. Kular, S. Basu, and R. I. Sharma, “The extracellular matrix: Structure, composition, age-related differences, tools for analysis and applications for tissue engineering,” *Journal of Tissue Engineering*, Dec. 2014, doi: 10.1177/2041731414557112.

[16] A. Padhi and A. S. Nain, “ECM in Differentiation: A Review of Matrix Structure, Composition and Mechanical Properties,” *Ann Biomed Eng*, vol. 48, no. 3, pp. 1071–1089, Mar. 2020, doi: 10.1007/s10439-019-02337-7.

[17] A. D. Theocharis, S. S. Skandalis, C. Gialeli, and N. K. Karamanos, “Extracellular matrix structure,” *Advanced Drug Delivery Reviews*, vol. 97, pp. 4–27, Feb. 2016, doi: 10.1016/j.addr.2015.11.001.

[18] J. J. Bara and F. Guilak, “Chapter 10 - Engineering functional tissues: in vitro culture parameters,” in *Principles of Tissue Engineering (Fifth Edition)*, R. Lanza, R. Langer, J. P. Vacanti, and A. Atala, Eds., Academic Press, 2020, pp. 157–177. doi: 10.1016/B978-0-12-818422-6.00011-3.

[19] L. Roseti *et al.*, “Scaffolds for Bone Tissue Engineering: State of the art and new perspectives,” *Materials Science and Engineering: C*, vol. 78, pp. 1246–1262, Sep. 2017, doi: 10.1016/j.msec.2017.05.017.

[20] J. Xing, N. Liu, N. Xu, W. Chen, and D. Xing, “Engineering Complex Anisotropic Scaffolds beyond Simply Uniaxial Alignment for Tissue Engineering,” *Advanced Functional Materials*, vol. 32, no. 15, p. 2110676, 2022, doi: 10.1002/adfm.202110676.

[21] F. Zhang and M. W. King, “Biodegradable Polymers as the Pivotal Player in the Design of Tissue Engineering Scaffolds,” *Advanced Healthcare Materials*, vol. 9, no. 13, p. 1901358, 2020, doi: 10.1002/adhm.201901358.

[22] A. Jafari, S. Hassanajili, F. Ghaffari, and N. Azarpira, “Modulating the physico-mechanical properties of polyacrylamide/gelatin hydrogels for tissue engineering application,” *Polym. Bull.*, vol. 79, no. 3, pp. 1821–1842, Mar. 2022, doi: 10.1007/s00289-021-03592-2.

[23] C. Montoya, Y. Du, A. L. Gianforcaro, S. Orrego, M. Yang, and P. I. Lelkes, “On the road to smart biomaterials for bone research: definitions, concepts, advances, and outlook,” *Bone Res*, vol. 9, no. 1, pp. 1–16, Feb. 2021, doi: 10.1038/s41413-020-00131-z.

[24] S. Naahidi *et al.*, “Biocompatibility of hydrogel-based scaffolds for tissue engineering applications,” *Biotechnology Advances*, vol. 35, no. 5, pp. 530–544, Sep. 2017, doi: 10.1016/j.biotechadv.2017.05.006.

[25] U. G. K. Wegst, H. Bai, E. Saiz, A. P. Tomsia, and R. O. Ritchie, “Bioinspired structural materials,” *Nature Mater*, vol. 14, no. 1, pp. 23–36, Jan. 2015, doi: 10.1038/nmat4089.

[26] V. Gold, Ed., *The IUPAC Compendium of Chemical Terminology: The Gold Book*, 4th ed. Research Triangle Park, NC: International Union of Pure and Applied Chemistry (IUPAC), 2019. doi: 10.1351/goldbook.

[27] S. Ma, B. Yu, X. Pei, and F. Zhou, “Structural hydrogels,” *Polymer*, vol. 98, pp. 516–535, Aug. 2016, doi: 10.1016/j.polymer.2016.06.053.

[28] K. Sano, Y. Ishida, and T. Aida, “Synthesis of Anisotropic Hydrogels and Their Applications,” *Angewandte Chemie International Edition*, vol. 57, no. 10, pp. 2532–2543, 2018, doi: 10.1002/anie.201708196.

[29] S. Babu, F. Albertino, A. Omidinia Anarkoli, and L. De Laporte, “Controlling Structure with Injectable Biomaterials to Better Mimic Tissue Heterogeneity and Anisotropy,” *Advanced Healthcare Materials*, vol. 10, no. 11, p. 2002221, 2021, doi: 10.1002/adhm.202002221.

[30] P. P. Samant *et al.*, “Sampling interstitial fluid from human skin using a microneedle patch,” *Science Translational Medicine*, vol. 12, no. 571, p. eaaw0285, Nov. 2020, doi: 10.1126/scitranslmed.aaw0285.

[31] Z. Wu *et al.*, “Interstitial fluid-based wearable biosensors for minimally invasive healthcare and biomedical applications,” *Commun Mater*, vol. 5, no. 1, pp. 1–15, Mar. 2024, doi: 10.1038/s43246-024-00468-6.

[32] M. Oprea and S. I. Voicu, “Recent advances in composites based on cellulose derivatives for biomedical applications,” *Carbohydrate Polymers*, vol. 247, p. 116683, Nov. 2020, doi: 10.1016/j.carbpol.2020.116683.

[33] M. N. Uddin, M. S. I. Jamal, Md. Y. Ali, Md. A. Darda, and S. I. Mahedi, “Tissue engineering and the potential use of chitin,” *emergent mater.*, vol. 6, no. 3, pp. 827–839, Jun. 2023, doi: 10.1007/s42247-023-00486-z.

[34] B. Shiroud Heidari *et al.*, “Natural, synthetic and commercially-available biopolymers used to regenerate tendons and ligaments,” *Bioactive Materials*, vol. 19, pp. 179–197, Jan. 2023, doi: 10.1016/j.bioactmat.2022.04.003.

[35] S. Ullah and X. Chen, “Fabrication, applications and challenges of natural biomaterials in tissue engineering,” *Applied Materials Today*, vol. 20, p. 100656, Sep. 2020, doi: 10.1016/j.apmt.2020.100656.

[36] S. Liu *et al.*, “Biomimetic natural biomaterials for tissue engineering and regenerative medicine: new biosynthesis methods, recent advances, and emerging applications,” *Military Med Res*, vol. 10, no. 1, p. 16, Mar. 2023, doi: 10.1186/s40779-023-00448-w.

[37] S. Dhania *et al.*, “Scaffolds the backbone of tissue engineering: Advancements in use of polyhydroxyalkanoates (PHA),” *International Journal of Biological Macromolecules*, vol. 208, pp. 243–259, May 2022, doi: 10.1016/j.ijbiomac.2022.03.030.

[38] K. Da Silva, P. Kumar, Y. E. Choonara, L. C. du Toit, and V. Pillay, “Three-dimensional printing of extracellular matrix (ECM)-mimicking scaffolds: A critical review of the current ECM materials,” *Journal of Biomedical Materials Research Part A*, vol. 108, no. 12, pp. 2324–2350, 2020, doi: 10.1002/jbm.a.36981.

[39] S. Radhakrishnan, S. Nagarajan, M. Bechelany, and S. N. Kalkura, “Collagen Based Biomaterials for Tissue Engineering Applications: A Review,” in *Processes and Phenomena on the*

Boundary Between Biogenic and Abiogenic Nature, O. V. Frank-Kamenetskaya, D. Yu. Vlasov, E. G. Panova, and S. N. Lessovaia, Eds., Cham: Springer International Publishing, 2020, pp. 3–22. doi: 10.1007/978-3-030-21614-6_1.

[40] E. Rezvani Ghomi, N. Nourbakhsh, M. Akbari Kenari, M. Zare, and S. Ramakrishna, "Collagen-based biomaterials for biomedical applications," *Journal of Biomedical Materials Research Part B: Applied Biomaterials*, vol. 109, no. 12, pp. 1986–1999, 2021, doi: 10.1002/jbm.b.34881.

[41] Y. Wang, Z. Wang, and Y. Dong, "Collagen-Based Biomaterials for Tissue Engineering," *ACS Biomater. Sci. Eng.*, vol. 9, no. 3, pp. 1132–1150, Mar. 2023, doi: 10.1021/acsbiomaterials.2c00730.

[42] M. Hemshekhar, R. M. Thushara, S. Chandranayaka, L. S. Sherman, K. Kemparaju, and K. S. Girish, "Emerging roles of hyaluronic acid bioscaffolds in tissue engineering and regenerative medicine," *International Journal of Biological Macromolecules*, vol. 86, pp. 917–928, May 2016, doi: 10.1016/j.ijbiomac.2016.02.032.

[43] P. Zhai, X. Peng, B. Li, Y. Liu, H. Sun, and X. Li, "The application of hyaluronic acid in bone regeneration," *International Journal of Biological Macromolecules*, vol. 151, pp. 1224–1239, May 2020, doi: 10.1016/j.ijbiomac.2019.10.169.

[44] K. Saravanakumar *et al.*, "Application of hyaluronic acid in tissue engineering, regenerative medicine, and nanomedicine: A review," *International Journal of Biological Macromolecules*, vol. 222, pp. 2744–2760, Dec. 2022, doi: 10.1016/j.ijbiomac.2022.10.055.

[45] M. Nikkhah, M. Akbari, A. Paul, A. Memic, A. Dolatshahi-Pirouz, and A. Khademhosseini, "Gelatin-Based Biomaterials For Tissue Engineering And Stem Cell Bioengineering," in *Biomaterials from Nature for Advanced Devices and Therapies*, John Wiley & Sons, Ltd, 2016, pp. 37–62. doi: 10.1002/9781119126218.ch3.

[46] A. B. Bello, D. Kim, D. Kim, H. Park, and S.-H. Lee, "Engineering and Functionalization of Gelatin Biomaterials: From Cell Culture to Medical Applications," *Tissue Engineering Part B: Reviews*, vol. 26, no. 2, pp. 164–180, Apr. 2020, doi: 10.1089/ten.teb.2019.0256.

[47] M. C. Echave, L. S. Burgo, J. L. Pedraz, and G. Orive, "Gelatin as Biomaterial for Tissue Engineering," *CPD*, vol. 23, no. 24, Sep. 2017, doi: 10.2174/0929867324666170511123101.

[48] D. Umuhoza, F. Yang, D. Long, Z. Hao, J. Dai, and A. Zhao, "Strategies for Tuning the Biodegradation of Silk Fibroin-Based Materials for Tissue Engineering Applications," *ACS Biomater. Sci. Eng.*, vol. 6, no. 3, pp. 1290–1310, Mar. 2020, doi: 10.1021/acsbiomaterials.9b01781.

[49] D. Ma, Y. Wang, and W. Dai, "Silk fibroin-based biomaterials for musculoskeletal tissue engineering," *Materials Science and Engineering: C*, vol. 89, pp. 456–469, Aug. 2018, doi: 10.1016/j.msec.2018.04.062.

[50] S. U. D. Wani, S. P. Gautam, Z. L. Qadrie, and H. V. Gangadharappa, "Silk fibroin as a natural polymeric based bio-material for tissue engineering and drug delivery systems-A review," *International Journal of Biological Macromolecules*, vol. 163, pp. 2145–2161, Nov. 2020, doi: 10.1016/j.ijbiomac.2020.09.057.

[51] R. Tarrahi, A. Khataee, A. Karimi, and Y. Yoon, “The latest achievements in plant cellulose-based biomaterials for tissue engineering focusing on skin repair,” *Chemosphere*, vol. 288, p. 132529, Feb. 2022, doi: 10.1016/j.chemosphere.2021.132529.

[52] M. Janmohammadi *et al.*, “Cellulose-based composite scaffolds for bone tissue engineering and localized drug delivery,” *Bioactive Materials*, vol. 20, pp. 137–163, Feb. 2023, doi: 10.1016/j.bioactmat.2022.05.018.

[53] S. D. Dutta, D. K. Patel, and K.-T. Lim, “Functional cellulose-based hydrogels as extracellular matrices for tissue engineering,” *J Biol Eng*, vol. 13, no. 1, p. 55, Jun. 2019, doi: 10.1186/s13036-019-0177-0.

[54] N. Bar-Shai, O. Sharabani-Yosef, M. Zollmann, A. Lesman, and A. Golberg, “Seaweed cellulose scaffolds derived from green macroalgae for tissue engineering,” *Sci Rep*, vol. 11, no. 1, p. 11843, Jun. 2021, doi: 10.1038/s41598-021-90903-2.

[55] S. Hasan, V. M. Boddu, D. S. Viswanath, and T. K. Ghosh, “Polysaccharides: Chitin and Chitosan,” in *Chitin and Chitosan: Science and Engineering*, S. Hasan, V. M. Boddu, D. S. Viswanath, and T. K. Ghosh, Eds., Cham: Springer International Publishing, 2022, pp. 1–16. doi: 10.1007/978-3-031-01229-7_1.

[56] S. Islam, M. A. R. Bhuiyan, and M. N. Islam, “Chitin and Chitosan: Structure, Properties and Applications in Biomedical Engineering,” *J Polym Environ*, vol. 25, no. 3, pp. 854–866, Sep. 2017, doi: 10.1007/s10924-016-0865-5.

[57] X. Li, J. Ding, X. Zhuang, F. Chang, J. Wang, and X. Chen, “Chitosan-Based Scaffolds for Cartilage Regeneration,” in *Chitin and Chitosan for Regenerative Medicine*, P. K. Dutta, Ed., New Delhi: Springer India, 2016, pp. 61–82. doi: 10.1007/978-81-322-2511-9_3.

[58] A. Kostenko, S. Swioklo, and C. J. Connon, “Alginate in corneal tissue engineering,” *Biomed. Mater.*, vol. 17, no. 2, p. 022004, Feb. 2022, doi: 10.1088/1748-605X/ac4d7b.

[59] D. R. Sahoo and T. Biswal, “Alginate and its application to tissue engineering,” *SN Appl. Sci.*, vol. 3, no. 1, p. 30, Jan. 2021, doi: 10.1007/s42452-020-04096-w.

[60] L. Aguero, S. Alpdagtas, E. Ilhan, D. Zaldivar-Silva, and O. Gunduz, “Functional role of crosslinking in alginate scaffold for drug delivery and tissue engineering: A review,” *European Polymer Journal*, vol. 160, p. 110807, Nov. 2021, doi: 10.1016/j.eurpolymj.2021.110807.

[61] R. Silva *et al.*, “Soft-matrices based on silk fibroin and alginate for tissue engineering,” *International Journal of Biological Macromolecules*, vol. 93, pp. 1420–1431, Dec. 2016, doi: 10.1016/j.ijbiomac.2016.04.045.

[62] Z. Terzopoulou, A. Zamboulis, I. Koumentakou, G. Michailidou, M. J. Noordam, and D. N. Bikiaris, “Biocompatible Synthetic Polymers for Tissue Engineering Purposes,” *Biomacromolecules*, vol. 23, no. 5, pp. 1841–1863, May 2022, doi: 10.1021/acs.biomac.2c00047.

[63] D. Ozdil and H. M. Aydin, “Polymers for medical and tissue engineering applications,” *Journal of Chemical Technology & Biotechnology*, vol. 89, no. 12, pp. 1793–1810, 2014, doi: 10.1002/jctb.4505.

[64] M. U. A. Khan, M. A. Aslam, M. F. Bin Abdullah, A. Hasan, S. A. Shah, and G. M. Stojanović, "Recent perspective of polymeric biomaterial in tissue engineering– a review," *Materials Today Chemistry*, vol. 34, p. 101818, Dec. 2023, doi: 10.1016/j.mtchem.2023.101818.

[65] M. Scarritt, M. Murdock, and S. F. Badylak, "Chapter 35 - Biologic Scaffolds Composed of Extracellular Matrix for Regenerative Medicine," in *Principles of Regenerative Medicine (Third Edition)*, A. Atala, R. Lanza, A. G. Mikos, and R. Nerem, Eds., Boston: Academic Press, 2019, pp. 613–626. doi: 10.1016/B978-0-12-809880-6.00035-7.

[66] Y. Zhang *et al.*, "Evolution of biomimetic ECM scaffolds from decellularized tissue matrix for tissue engineering: A comprehensive review," *International Journal of Biological Macromolecules*, vol. 246, p. 125672, Aug. 2023, doi: 10.1016/j.ijbiomac.2023.125672.

[67] X. Zhang, X. Chen, H. Hong, R. Hu, J. Liu, and C. Liu, "Decellularized extracellular matrix scaffolds: Recent trends and emerging strategies in tissue engineering," *Bioactive Materials*, vol. 10, pp. 15–31, Apr. 2022, doi: 10.1016/j.bioactmat.2021.09.014.

[68] J. Jang, T. G. Kim, B. S. Kim, S.-W. Kim, S.-M. Kwon, and D.-W. Cho, "Tailoring mechanical properties of decellularized extracellular matrix bioink by vitamin B2-induced photo-crosslinking," *Acta Biomaterialia*, vol. 33, pp. 88–95, Mar. 2016, doi: 10.1016/j.actbio.2016.01.013.

[69] F. Pati *et al.*, "Printing three-dimensional tissue analogues with decellularized extracellular matrix bioink," *Nat Commun*, vol. 5, no. 1, p. 3935, Jun. 2014, doi: 10.1038/ncomms4935.

[70] K. Dave and V. G. Gomes, "Interactions at scaffold interfaces: Effect of surface chemistry, structural attributes and bioaffinity," *Materials Science and Engineering: C*, vol. 105, p. 110078, Dec. 2019, doi: 10.1016/j.msec.2019.110078.

[71] C. M. Murphy, F. O'Brien, D. G. Little, and A. Schindeler, "Cell-scaffold interactions in the bone tissue engineering triad.," Jan. 2013, doi: 10.22203/eCM.v026a09'].

[72] E. Altuntaş, B. Özkan, and G. Yener, "3 - Porous scaffolds," in *Nanobiomaterials Science, Development and Evaluation*, M. Razavi and A. Thakor, Eds., Woodhead Publishing, 2017, pp. 27–59. doi: 10.1016/B978-0-08-100963-5.00003-3.

[73] B. Zhang, J. Huang, and R. J. Narayan, "Gradient scaffolds for osteochondral tissue engineering and regeneration," *Journal of Materials Chemistry B*, vol. 8, no. 36, pp. 8149–8170, 2020, doi: 10.1039/D0TB00688B.

[74] A. Sainio and H. Järveläinen, "Extracellular matrix-cell interactions: Focus on therapeutic applications," *Cellular Signalling*, vol. 66, p. 109487, Feb. 2020, doi: 10.1016/j.cellsig.2019.109487.

[75] B. Yue, "Biology of the Extracellular Matrix: An Overview," *Journal of Glaucoma*, vol. 23, p. S20, Nov. 2014, doi: 10.1097/IJG.0000000000000108.

[76] M. Dibus, O. Joshi, and J. Ivaska, "Novel tools to study cell-ECM interactions, cell adhesion dynamics and migration," *Current Opinion in Cell Biology*, vol. 88, p. 102355, Jun. 2024, doi: 10.1016/j.ceb.2024.102355.

[77] C. Li, L. Ouyang, J. P. K. Armstrong, and M. M. Stevens, “Advances in the Fabrication of Biomaterials for Gradient Tissue Engineering,” *Trends in Biotechnology*, vol. 39, no. 2, pp. 150–164, Feb. 2021, doi: 10.1016/j.tibtech.2020.06.005.

[78] Z. Liu, Z. Zhang, and R. O. Ritchie, “Structural Orientation and Anisotropy in Biological Materials: Functional Designs and Mechanics,” *Advanced Functional Materials*, vol. 30, no. 10, p. 1908121, 2020, doi: 10.1002/adfm.201908121.

[79] N. Pan, “Exploring the significance of structural hierarchy in material systems—A review,” *Applied Physics Reviews*, vol. 1, no. 2, p. 021302, Apr. 2014, doi: 10.1063/1.4871365.

[80] X. Niu, N. Li, Z. Du, and X. Li, “Integrated gradient tissue-engineered osteochondral scaffolds: Challenges, current efforts and future perspectives,” *Bioactive Materials*, vol. 20, pp. 574–597, Feb. 2023, doi: 10.1016/j.bioactmat.2022.06.011.

[81] R. Sinha *et al.*, “A hybrid additive manufacturing platform to create bulk and surface composition gradients on scaffolds for tissue regeneration,” *Nat Commun*, vol. 12, no. 1, p. 500, Jan. 2021, doi: 10.1038/s41467-020-20865-y.

[82] Y. Hong, J. G. Zhou, and D. Yao, “Porogen Templating Processes: An Overview,” *Journal of Manufacturing Science and Engineering*, vol. 136, no. 031013, Mar. 2014, doi: 10.1115/1.4026899.

[83] M. S. Flores-Jiménez, A. Garcia-Gonzalez, and R. Q. Fuentes-Aguilar, “Review on Porous Scaffolds Generation Process: A Tissue Engineering Approach,” *ACS Appl. Bio Mater.*, vol. 6, no. 1, pp. 1–23, Jan. 2023, doi: 10.1021/acsabm.2c00740.

[84] A. Haider *et al.*, “Advances in the scaffolds fabrication techniques using biocompatible polymers and their biomedical application: A technical and statistical review,” *Journal of Saudi Chemical Society*, vol. 24, no. 2, pp. 186–215, Feb. 2020, doi: 10.1016/j.jscs.2020.01.002.

[85] A. A. M. Shimojo, I. C. P. Rodrigues, A. G. M. Perez, E. M. B. Souto, L. P. Gabriel, and T. Webster, “Scaffolds for Tissue Engineering: A State-of-the-Art Review Concerning Types, Properties, Materials, Processing, and Characterization,” in *Racing for the Surface: Antimicrobial and Interface Tissue Engineering*, B. Li, T. F. Moriarty, T. Webster, and M. Xing, Eds., Cham: Springer International Publishing, 2020, pp. 647–676. doi: 10.1007/978-3-030-34471-9_23.

[86] A. Koyyada and P. Orsu, “Recent Advancements and Associated Challenges of Scaffold Fabrication Techniques in Tissue Engineering Applications,” *Regen. Eng. Transl. Med.*, vol. 7, no. 2, pp. 147–159, Jun. 2021, doi: 10.1007/s40883-020-00166-y.

[87] M. L. Chinta, A. Velidandi, N. P. P. Pabbathi, S. Dahariya, and S. R. Parcha, “Assessment of properties, applications and limitations of scaffolds based on cellulose and its derivatives for cartilage tissue engineering: A review,” *International Journal of Biological Macromolecules*, vol. 175, pp. 495–515, Apr. 2021, doi: 10.1016/j.ijbiomac.2021.01.196.

[88] J. D. Obayemi *et al.*, “Degradable porous drug-loaded polymer scaffolds for localized cancer drug delivery and breast cell/tissue growth,” *Materials Science and Engineering: C*, vol. 112, p. 110794, Jul. 2020, doi: 10.1016/j.msec.2020.110794.

[89] A. Forget *et al.*, “Facile preparation of tissue engineering scaffolds with pore size gradients using the muesli effect and their application to cell spheroid encapsulation,” *Journal of Biomedical Materials Research Part B: Applied Biomaterials*, vol. 108, no. 6, pp. 2495–2504, 2020, doi: 10.1002/jbm.b.34581.

[90] B. A. Harley, A. Z. Hastings, I. V. Yannas, and A. Sannino, “Fabricating tubular scaffolds with a radial pore size gradient by a spinning technique,” *Biomaterials*, vol. 27, no. 6, pp. 866–874, Feb. 2006, doi: 10.1016/j.biomaterials.2005.07.012.

[91] F. R. Mansour, S. Waheed, B. Paull, and F. Maya, “Porogens and porogen selection in the preparation of porous polymer monoliths,” *Journal of Separation Science*, vol. 43, no. 1, pp. 56–69, 2020, doi: 10.1002/jssc.201900876.

[92] Q. L. Loh and C. Choong, “Three-Dimensional Scaffolds for Tissue Engineering Applications: Role of Porosity and Pore Size,” *Tissue Engineering Part B: Reviews*, vol. 19, no. 6, pp. 485–502, Dec. 2013, doi: 10.1089/ten.teb.2012.0437.

[93] W. S. Harley *et al.*, “Advances in biofabrication techniques towards functional bioprinted heterogeneous engineered tissues: A comprehensive review,” *Bioprinting*, vol. 23, p. e00147, Aug. 2021, doi: 10.1016/j.bprint.2021.e00147.

[94] N. Shahrubudin, T. C. Lee, and R. Ramlan, “An Overview on 3D Printing Technology: Technological, Materials, and Applications,” *Procedia Manufacturing*, vol. 35, pp. 1286–1296, Jan. 2019, doi: 10.1016/j.promfg.2019.06.089.

[95] J. Li, C. Wu, P. K. Chu, and M. Gelinsky, “3D printing of hydrogels: Rational design strategies and emerging biomedical applications,” *Materials Science and Engineering: R: Reports*, vol. 140, p. 100543, Apr. 2020, doi: 10.1016/j.mser.2020.100543.

[96] T. Billiet, M. Vandenhaute, J. Schelfhout, S. Van Vlierberghe, and P. Dubruel, “A review of trends and limitations in hydrogel-rapid prototyping for tissue engineering,” *Biomaterials*, vol. 33, no. 26, pp. 6020–6041, Sep. 2012, doi: 10.1016/j.biomaterials.2012.04.050.

[97] F. P. W. Melchels, M. A. N. Domingos, T. J. Klein, J. Malda, P. J. Bartolo, and D. W. Hutmacher, “Additive manufacturing of tissues and organs,” *Progress in Polymer Science*, vol. 37, no. 8, pp. 1079–1104, Aug. 2012, doi: 10.1016/j.progpolymsci.2011.11.007.

[98] M. Hospodiuk, M. Dey, D. Sosnoski, and I. T. Ozbolat, “The bioink: A comprehensive review on bioprintable materials,” *Biotechnology Advances*, vol. 35, no. 2, pp. 217–239, Mar. 2017, doi: 10.1016/j.biotechadv.2016.12.006.

[99] S. Derakhshanfar, R. Mbeleck, K. Xu, X. Zhang, W. Zhong, and M. Xing, “3D bioprinting for biomedical devices and tissue engineering: A review of recent trends and advances,” *Bioactive Materials*, vol. 3, no. 2, pp. 144–156, Jun. 2018, doi: 10.1016/j.bioactmat.2017.11.008.

[100] I. T. Ozbolat and M. Hospodiuk, “Current advances and future perspectives in extrusion-based bioprinting,” *Biomaterials*, vol. 76, pp. 321–343, Jan. 2016, doi: 10.1016/j.biomaterials.2015.10.076.

[101] D. M. Kirchmajer, R. G. Iii, and M. in het Panhuis, “An overview of the suitability of hydrogel-forming polymers for extrusion-based 3D-printing,” *Journal of Materials Chemistry B*, vol. 3, no. 20, pp. 4105–4117, 2015, doi: 10.1039/C5TB00393H.

[102] J. A. Lewis, “Direct Ink Writing of 3D Functional Materials,” *Advanced Functional Materials*, vol. 16, no. 17, pp. 2193–2204, 2006, doi: 10.1002/adfm.200600434.

[103] D. B. Kolesky, R. L. Truby, A. S. Gladman, T. A. Busbee, K. A. Homan, and J. A. Lewis, “3D Bioprinting of Vascularized, Heterogeneous Cell-Laden Tissue Constructs,” *Advanced Materials*, vol. 26, no. 19, pp. 3124–3130, May 2014, doi: 10.1002/adma.201305506.

[104] A. Sydney Gladman, E. A. Matsumoto, R. G. Nuzzo, L. Mahadevan, and J. A. Lewis, “Biomimetic 4D printing,” *Nature Mater*, vol. 15, no. 4, pp. 413–418, Apr. 2016, doi: 10.1038/nmat4544.

[105] H. Gudapati, M. Dey, and I. Ozbolat, “A comprehensive review on droplet-based bioprinting: Past, present and future,” *Biomaterials*, vol. 102, pp. 20–42, Sep. 2016, doi: 10.1016/j.biomaterials.2016.06.012.

[106] A. Rohani Shirvan, A. Nouri, and C. Wen, “12 - Structural polymer biomaterials,” in *Structural Biomaterials*, C. Wen, Ed., in Woodhead Publishing Series in Biomaterials. , Woodhead Publishing, 2021, pp. 395–439. doi: 10.1016/B978-0-12-818831-6.00010-0.

[107] N. Abbasi, S. Hamlet, R. M. Love, and N.-T. Nguyen, “Porous scaffolds for bone regeneration,” *Journal of Science: Advanced Materials and Devices*, vol. 5, no. 1, pp. 1–9, Mar. 2020, doi: 10.1016/j.jsamd.2020.01.007.

[108] R. J. Mondschein, A. Kanitkar, C. B. Williams, S. S. Verbridge, and T. E. Long, “Polymer structure-property requirements for stereolithographic 3D printing of soft tissue engineering scaffolds,” *Biomaterials*, vol. 140, pp. 170–188, Sep. 2017, doi: 10.1016/j.biomaterials.2017.06.005.

[109] H. Yin, Y. Ding, Y. Zhai, W. Tan, and X. Yin, “Orthogonal programming of heterogeneous micro-mechano-environments and geometries in three-dimensional bio-stereolithography,” *Nat Commun*, vol. 9, no. 1, p. 4096, Oct. 2018, doi: 10.1038/s41467-018-06685-1.

[110] M. B. Applegate *et al.*, “Laser-based three-dimensional multiscale micropatterning of biocompatible hydrogels for customized tissue engineering scaffolds,” *Proceedings of the National Academy of Sciences*, vol. 112, no. 39, pp. 12052–12057, Sep. 2015, doi: 10.1073/pnas.1509405112.

[111] A. A. Pawar *et al.*, “High-performance 3D printing of hydrogels by water-dispersible photoinitiator nanoparticles,” *Science Advances*, vol. 2, no. 4, p. e1501381, Apr. 2016, doi: 10.1126/sciadv.1501381.

[112] S. You, J. Li, W. Zhu, C. Yu, D. Mei, and S. Chen, “Nanoscale 3D printing of hydrogels for cellular tissue engineering,” *Journal of Materials Chemistry B*, vol. 6, no. 15, pp. 2187–2197, 2018, doi: 10.1039/C8TB00301G.

[113] P. Ambhorkar, R. H. Rakin, Z. Wang, H. Kumar, and K. Kim, “Biofabrication strategies for engineering heterogeneous artificial tissues,” *Additive Manufacturing*, vol. 36, p. 101459, Dec. 2020, doi: 10.1016/j.addma.2020.101459.

[114] A. McCormack, C. B. Highley, N. R. Leslie, and F. P. W. Melchels, “3D Printing in Suspension Baths: Keeping the Promises of Bioprinting Afloat,” *Trends in Biotechnology*, vol. 38, no. 6, pp. 584–593, Jun. 2020, doi: 10.1016/j.tibtech.2019.12.020.

[115] N. Khuu, S. Kheiri, and E. Kumacheva, “Structurally anisotropic hydrogels for tissue engineering,” *TRECHEM*, vol. 3, no. 12, pp. 1002–1026, Dec. 2021, doi: 10.1016/j.trechm.2021.09.009.

[116] X. Su, T. Wang, and S. Guo, “Applications of 3D printed bone tissue engineering scaffolds in the stem cell field,” *Regenerative Therapy*, vol. 16, pp. 63–72, Mar. 2021, doi: 10.1016/j.reth.2021.01.007.

[117] W. Wu, C. J. Hansen, A. M. Aragón, P. H. Geubelle, S. R. White, and J. A. Lewis, “Direct-write assembly of biomimetic microvascular networks for efficient fluid transport,” *Soft Matter*, vol. 6, no. 4, pp. 739–742, 2010, doi: 10.1039/B918436H.

[118] J. S. Miller *et al.*, “Rapid casting of patterned vascular networks for perfusable engineered three-dimensional tissues,” *Nature Mater*, vol. 11, no. 9, pp. 768–774, Sep. 2012, doi: 10.1038/nmat3357.

[119] J. G. Torres-Rendon *et al.*, “Bioactive Gyroid Scaffolds Formed by Sacrificial Templating of Nanocellulose and Nanochitin Hydrogels as Instructive Platforms for Biomimetic Tissue Engineering,” *Advanced Materials*, vol. 27, no. 19, pp. 2989–2995, 2015, doi: 10.1002/adma.201405873.

[120] S. Mohanty *et al.*, “Fabrication of scalable and structured tissue engineering scaffolds using water dissolvable sacrificial 3D printed moulds,” *Materials Science and Engineering: C*, vol. 55, pp. 569–578, Oct. 2015, doi: 10.1016/j.msec.2015.06.002.

[121] J. D. McNulty *et al.*, “Micro-injection molded, poly(vinyl alcohol)-calcium salt templates for precise customization of 3D hydrogel internal architecture,” *Acta Biomaterialia*, vol. 95, pp. 258–268, Sep. 2019, doi: 10.1016/j.actbio.2019.04.050.

[122] C. Wang and Y. Zhou, “Sacrificial biomaterials in 3D fabrication of scaffolds for tissue engineering applications,” *Journal of Biomedical Materials Research Part B: Applied Biomaterials*, vol. 112, no. 1, p. e35312, 2024, doi: 10.1002/jbm.b.35312.

[123] S. Vijayavenkataraman, “3D Bioprinting: Challenges in Commercialization and Clinical Translation,” *Journal of 3D Printing in Medicine*, vol. 7, no. 2, p. 3DP8, May 2023, doi: 10.2217/3dp-2022-0026.

[124] L. Faber, A. Yau, and Y. Chen, “Translational biomaterials of four-dimensional bioprinting for tissue regeneration,” *Biofabrication*, vol. 16, no. 1, p. 012001, Oct. 2023, doi: 10.1088/1758-5090/acfdd0.

[125] M. A. Cousin *et al.*, “The Value of Systematic Reviews in Estimating the Cost and Barriers to Translation in Tissue Engineering,” *Tissue Engineering Part B: Reviews*, vol. 22, no. 6, pp. 430–437, Dec. 2016, doi: 10.1089/ten.teb.2016.0060.

[126] S. J. Hollister and W. L. Murphy, “Scaffold Translation: Barriers Between Concept and Clinic,” *Tissue Engineering Part B: Reviews*, vol. 17, no. 6, pp. 459–474, Dec. 2011, doi: 10.1089/ten.teb.2011.0251.

[127] W. L. Niermeyer, C. Rodman, M. M. Li, and T. Chiang, “Tissue engineering applications in otolaryngology—The state of translation,” *Laryngoscope Investigative Otolaryngology*, vol. 5, no. 4, pp. 630–648, 2020, doi: 10.1002/lio2.416.

[128] Y. Li, M. Zhou, W. Zheng, J. Yang, and N. Jiang, “Scaffold-based tissue engineering strategies for soft–hard interface regeneration,” *Regenerative Biomaterials*, vol. 10, p. rbac091, Jan. 2023, doi: 10.1093/rb/rbac091.

[129] J. Z. Gul *et al.*, “3D printing for soft robotics - a review,” *Sci Technol Adv Mater*, vol. 19, no. 1, pp. 243–262, Mar. 2018, doi: 10.1080/14686996.2018.1431862.

[130] T. Distler and A. R. Boccaccini, “3D printing of electrically conductive hydrogels for tissue engineering and biosensors – A review,” *Acta Biomaterialia*, vol. 101, pp. 1–13, Jan. 2020, doi: 10.1016/j.actbio.2019.08.044.

[131] H. Banerjee, M. Suhail, and H. Ren, “Hydrogel Actuators and Sensors for Biomedical Soft Robots: Brief Overview with Impending Challenges,” *Biomimetics (Basel)*, vol. 3, no. 3, p. 15, Jul. 2018, doi: 10.3390/biomimetics3030015.

[132] K. J. De France, F. Xu, and T. Hoare, “Structured Macroporous Hydrogels: Progress, Challenges, and Opportunities,” *Advanced Healthcare Materials*, vol. 7, no. 1, Dec. 2017, doi: 10.1002/adhm.201700927.

[133] Y. S. Zhang and A. Khademhosseini, “Advances in engineering hydrogels,” *Science*, vol. 356, no. 6337, p. eaaf3627, May 2017, doi: 10.1126/science.aaf3627.

[134] C. Keplinger, J.-Y. Sun, C. C. Foo, P. Rothemund, G. M. Whitesides, and Z. Suo, “Stretchable, Transparent, Ionic Conductors,” *Science*, vol. 341, no. 6149, pp. 984–987, Aug. 2013, doi: 10.1126/science.1240228.

[135] H. Yuk, B. Lu, and X. Zhao, “Hydrogel bioelectronics,” *Chemical Society Reviews*, vol. 48, no. 6, pp. 1642–1667, 2019, doi: 10.1039/c8cs00595h.

[136] C. Yang and Z. Suo, “Hydrogel ionotronics,” *Nature Reviews Materials*, vol. 3, no. 6, pp. 125–142, May 2018, doi: 10.1038/s41578-018-0018-7.

[137] J. Malda *et al.*, “25th Anniversary Article: Engineering Hydrogels for Biofabrication,” *Advanced Materials*, vol. 25, no. 36, pp. 5011–5028, Aug. 2013, doi: 10.1002/adma.201302042.

[138] J. Saroia, W. Yanen, Q. Wei, K. Zhang, T. Lu, and B. Zhang, “A review on biocompatibility nature of hydrogels with 3D printing techniques, tissue engineering application and its future

prospective," *Bio-Design and Manufacturing*, vol. 1, no. 4, pp. 265–279, Nov. 2018, doi: 10.1007/s42242-018-0029-7.

[139] D. Chimene, K. K. Lennox, R. R. Kaunas, and A. K. Gaharwar, "Advanced Bioinks for 3D Printing: A Materials Science Perspective," *Annals of Biomedical Engineering*, vol. 44, no. 6, pp. 2090–2102, May 2016, doi: 10.1007/s10439-016-1638-y.

[140] L. R. Feksa, E. A. Troian, C. D. Muller, F. Viegas, A. B. Machado, and V. C. Rech, "Hydrogels for biomedical applications," *Nanostructures for the Engineering of Cells, Tissues and Organs*, pp. 403–438, 2018, doi: 10.1016/b978-0-12-813665-2.00011-9.

[141] P. Tseng *et al.*, "Directed assembly of bio-inspired hierarchical materials with controlled nanofibrillar architectures," *Nature Nanotechnology*, vol. 12, no. 5, pp. 474–480, Feb. 2017, doi: 10.1038/nnano.2017.4.

[142] H. S. Song, O. S. Kwon, J.-H. Kim, J. Conde, and N. Artzi, "3D hydrogel scaffold doped with 2D graphene materials for biosensors and bioelectronics," *Biosensors and Bioelectronics*, vol. 89, pp. 187–200, Mar. 2017, doi: 10.1016/j.bios.2016.03.045.

[143] M.-L. Xu, L.-Y. Guan, S.-K. Li, L. Chen, and Z. Chen, "Stable gold graphitic nanocapsule doped hydrogels for efficient photothermal antibacterial applications," *Chemical Communications*, vol. 55, no. 37, pp. 5359–5362, 2019, doi: 10.1039/c9cc01933b.

[144] L. Han *et al.*, "Tough, self-healable and tissue-adhesive hydrogel with tunable multifunctionality," *NPG Asia Materials*, vol. 9, no. 4, pp. e372–e372, Apr. 2017, doi: 10.1038/am.2017.33.

[145] Y. Jiang and Q. Wang, "Highly-stretchable 3D-architected Mechanical Metamaterials," *Sci Rep*, vol. 6, pp. 34147–34147, Sep. 2016, doi: 10.1038/srep34147.

[146] A. R. Escobar *et al.*, "Fluidic Infiltrative Assembly of 3D Hydrogel with Heterogeneous Composition and Function," *Adv Funct Materials*, vol. 31, no. 33, p. 2103288, Aug. 2021, doi: 10.1002/adfm.202103288.

[147] T. A. Pham, D. -P. Kim, T. -W. Lim, S. -H. Park, D. -Y. Yang, and K. -S. Lee, "Three-Dimensional SiCN Ceramic Microstructures via Nano-Stereolithography of Inorganic Polymer Photoresists," *Advanced Functional Materials*, vol. 16, no. 9, pp. 1235–1241, May 2006, doi: 10.1002/adfm.200600009.

[148] J. Z. Manapat, Q. Chen, P. Ye, and R. C. Advincula, "3D Printing of Polymer Nanocomposites via Stereolithography," *Macromolecular Materials and Engineering*, vol. 302, no. 9, May 2017, doi: 10.1002/mame.201600553.

[149] T. S. Demina *et al.*, "Two-Photon-Induced Microstereolithography of Chitosan-g-Oligolactides as a Function of Their Stereochemical Composition," *Polymers (Basel)*, vol. 9, no. 7, p. 302, Jul. 2017, doi: 10.3390/polym9070302.

[150] A. Mahler, M. Reches, M. Rechter, S. Cohen, and E. Gazit, "Rigid, Self-Assembled Hydrogel Composed of a Modified Aromatic Dipeptide," *Advanced Materials*, vol. 18, no. 11, pp. 1365–1370, Apr. 2006, doi: 10.1002/adma.200501765.

[151] B. B. Mandal, A. Grinberg, E. S. Gil, B. Panilaitis, and D. L. Kaplan, “High-strength silk protein scaffolds for bone repair,” *Proc Natl Acad Sci U S A*, vol. 109, no. 20, pp. 7699–7704, May 2012, doi: 10.1073/pnas.1119474109.

[152] S. Khorshidi and A. Karkhaneh, “Electrically conductive gel/fibers composite scaffold with graded properties,” *Materials Science and Engineering: C*, vol. 74, pp. 238–245, May 2017, doi: 10.1016/j.msec.2016.12.014.

[153] J. Hao, H. Cheng, P. Butler, L. Zhang, and C. C. Han, “Origin of cononsolvency, based on the structure of tetrahydrofuran-water mixture,” *The Journal of Chemical Physics*, vol. 132, no. 15, Apr. 2010, doi: 10.1063/1.3381177.

[154] M. S. Williams, K. J. Longmuir, and P. Yager, “A practical guide to the staggered herringbone mixer,” *Lab Chip*, vol. 8, no. 7, pp. 1121–1129, Jul. 2008, doi: 10.1039/b802562b.

[155] D. Huh *et al.*, “Gravity-driven microfluidic particle sorting device with hydrodynamic separation amplification,” *Anal Chem*, vol. 79, no. 4, pp. 1369–1376, Feb. 2007, doi: 10.1021/ac061542n.

[156] J. W. Gooch, “ASTM D638,” *Encyclopedic Dictionary of Polymers*, pp. 51–51, 2011, doi: 10.1007/978-1-4419-6247-8_856.

[157] M. A. Haq, Y. Su, and D. Wang, “Mechanical properties of PNIPAM based hydrogels: A review,” *Materials Science and Engineering: C*, vol. 70, pp. 842–855, Jan. 2017, doi: 10.1016/j.msec.2016.09.081.

[158] C. Zhao, Z. Ma, and X. X. Zhu, “Rational design of thermoresponsive polymers in aqueous solutions: A thermodynamics map,” *Progress in Polymer Science*, vol. 90, pp. 269–291, Mar. 2019, doi: 10.1016/j.progpolymsci.2019.01.001.

[159] V. S. Deshpande, N. A. Fleck, and M. F. Ashby, “Effective properties of the octet-truss lattice material,” *Journal of the Mechanics and Physics of Solids*, vol. 49, no. 8, pp. 1747–1769, Aug. 2001, doi: 10.1016/s0022-5096(01)00010-2.

[160] X. Y. Chen and H. F. Tan, “An effective length model for octet lattice,” *International Journal of Mechanical Sciences*, vol. 140, pp. 279–287, May 2018, doi: 10.1016/j.ijmecsci.2018.03.016.

[161] X. Zheng *et al.*, “Multiscale metallic metamaterials,” *Nature Materials*, vol. 15, no. 10, pp. 1100–1106, Jul. 2016, doi: 10.1038/nmat4694.

[162] T. A. Schaedler and W. B. Carter, “Architected Cellular Materials,” *Annual Review of Materials Research*, vol. 46, no. 1, pp. 187–210, Jul. 2016, doi: 10.1146/annurev-matsci-070115-031624.

[163] J. U. Surjadi *et al.*, “Mechanical Metamaterials and Their Engineering Applications,” *Advanced Engineering Materials*, vol. 21, no. 3, Jan. 2019, doi: 10.1002/adem.201800864.

[164] C. Ling, A. Cernicchi, M. D. Gilchrist, and P. Cardiff, “Mechanical behaviour of additively-manufactured polymeric octet-truss lattice structures under quasi-static and dynamic

compressive loading," *Materials & Design*, vol. 162, pp. 106–118, Jan. 2019, doi: 10.1016/j.matdes.2018.11.035.

[165] J.-Y. Sun *et al.*, "Highly stretchable and tough hydrogels," *Nature*, vol. 489, no. 7414, pp. 133–136, Sep. 2012, doi: 10.1038/nature11409.

[166] M. C. Darnell *et al.*, "Performance and biocompatibility of extremely tough alginate/polyacrylamide hydrogels," *Biomaterials*, vol. 34, no. 33, pp. 8042–8048, Nov. 2013, doi: 10.1016/j.biomaterials.2013.06.061.

[167] J. Li, W. R. K. Illeperuma, Z. Suo, and J. J. Vlassak, "Hybrid Hydrogels with Extremely High Stiffness and Toughness," *ACS Macro Letters*, vol. 3, no. 6, pp. 520–523, May 2014, doi: 10.1021/mz5002355.

[168] J. Wang, J. Wei, S. Su, J. Qiu, and S. Wang, "Ion-linked double-network hydrogel with high toughness and stiffness," *Journal of Materials Science*, vol. 50, no. 16, pp. 5458–5465, May 2015, doi: 10.1007/s10853-015-9091-0.

[169] P. Demianenko and B. Minisini, "Stiff IPN Hydrogels of Poly(Acrylamide) and Alginate: Influence of the Crosslinking Ion's Valence on Hydrogel's Final Properties," *Journal of Chemical Engineering & Process Technology*, vol. 07, no. 04, 2016, doi: 10.4172/2157-7048.1000304.

[170] W. Guo, M. Li, and J. Zhou, "Modeling programmable deformation of self-folding all-polymer structures with temperature-sensitive hydrogels," *Smart Materials and Structures*, vol. 22, no. 11, p. 115028, Oct. 2013, doi: 10.1088/0964-1726/22/11/115028.

[171] J. Abdolahi, M. Baghani, N. Arbabi, and H. Mazaheri, "Analytical and numerical analysis of swelling-induced large bending of thermally-activated hydrogel bilayers," *International Journal of Solids and Structures*, vol. 99, pp. 1–11, Nov. 2016, doi: 10.1016/j.ijsolstr.2016.08.017.

[172] X. Li, X. Cai, Y. Gao, and M. J. Serpe, "Reversible bidirectional bending of hydrogel-based bilayer actuators," *Journal of Materials Chemistry B*, vol. 5, no. 15, pp. 2804–2812, 2017, doi: 10.1039/c7tb00426e.

[173] J. Zheng *et al.*, "Mimosa inspired bilayer hydrogel actuator functioning in multi-environments," *Journal of Materials Chemistry C*, vol. 6, no. 6, pp. 1320–1327, 2018, doi: 10.1039/c7tc04879c.

[174] A. H. Nourian, A. Amiri, N. Moini, and M. Baghani, "Synthesis, test, calibration and modeling of a temperature-actuated hydrogel bilayer," *Smart Materials and Structures*, vol. 29, no. 10, p. 105001, Aug. 2020, doi: 10.1088/1361-665x/ab9f46.

[175] X. Zhao, "Multi-scale multi-mechanism design of tough hydrogels: building dissipation into stretchy networks," *Soft Matter*, vol. 10, no. 5, pp. 672–687, 2014, doi: 10.1039/C3SM52272E.

[176] G. Miklosic, S. J. Ferguson, and M. D'Este, "Engineering complex tissue-like microenvironments with biomaterials and biofabrication," *Trends in Biotechnology*, p. S0167779924000891, Apr. 2024, doi: 10.1016/j.tibtech.2024.03.008.

[177] P. Chansoria, S. Asif, N. Gupta, J. Piedrahita, and R. A. Shirwaiker, “Multiscale Anisotropic Tissue Biofabrication via Bulk Acoustic Patterning of Cells and Functional Additives in Hybrid Bioinks,” *Advanced Healthcare Materials*, vol. 11, no. 10, p. 2102351, 2022, doi: 10.1002/adhm.202102351.

[178] G.-X. Xu, P.-Y. Chen, X. Jiang, and C.-C. Huang, “Visualization of Human Skeletal Muscle Mechanical Anisotropy by Using Dual-Direction Shear Wave Imaging,” *IEEE Transactions on Biomedical Engineering*, vol. 69, no. 9, pp. 2745–2754, Sep. 2022, doi: 10.1109/TBME.2022.3152896.

[179] N. Tueni, J.-M. Allain, and M. Genet, “On the structural origin of the anisotropy in the myocardium: Multiscale modeling and analysis,” *Journal of the Mechanical Behavior of Biomedical Materials*, vol. 138, p. 105600, Feb. 2023, doi: 10.1016/j.jmbbm.2022.105600.

[180] Y. Chen *et al.*, “Bi-Layered Tubular Microfiber Scaffolds as Functional Templates for Engineering Human Intestinal Smooth Muscle Tissue,” *Advanced Functional Materials*, vol. 30, no. 17, p. 2000543, 2020, doi: 10.1002/adfm.202000543.

[181] L. Wang, Y. Wu, B. Guo, and P. X. Ma, “Nanofiber Yarn/Hydrogel Core–Shell Scaffolds Mimicking Native Skeletal Muscle Tissue for Guiding 3D Myoblast Alignment, Elongation, and Differentiation,” *ACS Nano*, vol. 9, no. 9, pp. 9167–9179, Sep. 2015, doi: 10.1021/acsnano.5b03644.

[182] M. J. Mondrinos *et al.*, “Surface-directed engineering of tissue anisotropy in microphysiological models of musculoskeletal tissue,” *Science Advances*, vol. 7, no. 11, p. eabe9446, Mar. 2021, doi: 10.1126/sciadv.abe9446.

[183] M. Hua *et al.*, “Strong tough hydrogels via the synergy of freeze-casting and salting out,” *Nature*, vol. 590, no. 7847, pp. 594–599, Feb. 2021, doi: 10.1038/s41586-021-03212-z.

[184] X. Dong, X. Guo, Q. Liu, Y. Zhao, H. Qi, and W. Zhai, “Strong and Tough Conductive Organo-Hydrogels via Freeze-Casting Assisted Solution Substitution,” *Adv Funct Materials*, vol. 32, no. 31, p. 2203610, Aug. 2022, doi: 10.1002/adfm.202203610.

[185] M. Barrow and H. Zhang, “Aligned porous stimuli-responsive hydrogels via directional freezing and frozen UV initiated polymerization,” *Soft Matter*, vol. 9, no. 9, p. 2723, 2013, doi: 10.1039/c2sm27722k.

[186] J. Luo *et al.*, “Fabrication of a High-Strength, Tough, Swelling-Resistant, Conductive Hydrogel via Ion Cross-Linking, Directional Freeze-Drying, and Rehydration,” *ACS Biomater. Sci. Eng.*, vol. 9, no. 5, pp. 2694–2705, May 2023, doi: 10.1021/acsbiomaterials.2c01520.

[187] A. Omidinia-Anarkoli, S. Boesveld, U. Tuvshindorj, J. C. Rose, T. Haraszti, and L. De Laporte, “An Injectable Hybrid Hydrogel with Oriented Short Fibers Induces Unidirectional Growth of Functional Nerve Cells,” *Small*, vol. 13, no. 36, p. 1702207, 2017, doi: 10.1002/smll.201702207.

[188] C. Wang, H. Yue, Q. Feng, B. Xu, L. Bian, and P. Shi, “Injectable Nanoreinforced Shape-Memory Hydrogel System for Regenerating Spinal Cord Tissue from Traumatic Injury,” *ACS Appl. Mater. Interfaces*, vol. 10, no. 35, pp. 29299–29307, Sep. 2018, doi: 10.1021/acsami.8b08929.

[189] X. Lin *et al.*, "Efficient fabrication of anisotropic regenerated cellulose films from bamboo via a facile wet extrusion strategy," *International Journal of Biological Macromolecules*, vol. 265, p. 130966, Apr. 2024, doi: 10.1016/j.ijbiomac.2024.130966.

[190] D. Ye *et al.*, "Ultrahigh Tough, Super Clear, and Highly Anisotropic Nanofiber-Structured Regenerated Cellulose Films," *ACS Nano*, vol. 13, no. 4, pp. 4843–4853, Apr. 2019, doi: 10.1021/acsnano.9b02081.

[191] Md. T. I. Mredha and I. Jeon, "Biomimetic anisotropic hydrogels: Advanced fabrication strategies, extraordinary functionalities, and broad applications," *Progress in Materials Science*, vol. 124, p. 100870, Feb. 2022, doi: 10.1016/j.pmatsci.2021.100870.

[192] H. Bai, Y. Chen, B. Delattre, A. P. Tomsia, and R. O. Ritchie, "Bioinspired large-scale aligned porous materials assembled with dual temperature gradients," *Science Advances*, Dec. 2015, doi: 10.1126/sciadv.1500849.

[193] S. Shan *et al.*, "Multistable Architected Materials for Trapping Elastic Strain Energy," *Advanced Materials*, vol. 27, no. 29, pp. 4296–4301, Aug. 2015, doi: 10.1002/adma.201501708.

[194] C.-C. Kuo, H. Qin, Y. Cheng, X. Jiang, and X. Shi, "An integrated manufacturing strategy to fabricate delivery system using gelatin/alginate hybrid hydrogels: 3D printing and freeze-drying," *Food Hydrocolloids*, vol. 111, p. 106262, Feb. 2021, doi: 10.1016/j.foodhyd.2020.106262.

[195] J. Bauer, L. R. Meza, T. A. Schaedler, R. Schwaiger, X. Zheng, and L. Valdevit, "Nanolattices: An Emerging Class of Mechanical Metamaterials," *Advanced Materials*, vol. 29, no. 40, p. 1701850, Oct. 2017, doi: 10.1002/adma.201701850.

[196] C. Viney, "Self-assembly as a route to fibrous materials: concepts, opportunities and challenges," *Current Opinion in Solid State and Materials Science*, vol. 8, no. 2, pp. 95–101, Mar. 2004, doi: 10.1016/j.cossms.2004.04.001.

[197] L. Li *et al.*, "Mechanically-directed assembly of nanostructured biopolymer with tunable anisotropy, hierarchy, and functionality," *Next Materials*, vol. 2, p. 100140, Jan. 2024, doi: 10.1016/j.nxmate.2024.100140.

[198] Q. Ge *et al.*, "Projection micro stereolithography based 3D printing and its applications," *Int. J. Extrem. Manuf.*, vol. 2, no. 2, p. 022004, Jun. 2020, doi: 10.1088/2631-7990/ab8d9a.

[199] B. Venzac *et al.*, "PDMS Curing Inhibition on 3D-Printed Molds: Why? Also, How to Avoid It?," *Anal. Chem.*, vol. 93, no. 19, pp. 7180–7187, May 2021, doi: 10.1021/acs.analchem.0c04944.

[200] S. Hong *et al.*, "3D Printing of Highly Stretchable and Tough Hydrogels into Complex, Cellularized Structures," *Advanced Materials*, vol. 27, no. 27, pp. 4035–4040, Jul. 2015, doi: 10.1002/adma.201501099.

[201] S. Li, D. Qi, and J. Huang, "Natural cellulose based self-assembly towards designed functionalities," *Current Opinion in Colloid & Interface Science*, vol. 35, pp. 1–8, May 2018, doi: 10.1016/j.cocis.2017.12.008.

[202] I. P. S. Fernando, W. Lee, E. J. Han, and G. Ahn, “Alginate-based nanomaterials: Fabrication techniques, properties, and applications,” *Chemical Engineering Journal*, vol. 391, p. 123823, Jul. 2020, doi: 10.1016/j.cej.2019.123823.

[203] S. Moeinzadeh, D. Barati, S. K. Sarvestani, O. Karaman, and E. Jabbari, “Nanostructure Formation and Transition from Surface to Bulk Degradation in Polyethylene Glycol Gels Chain-Extended with Short Hydroxy Acid Segments,” *Biomacromolecules*, vol. 14, no. 8, pp. 2917–2928, Aug. 2013, doi: 10.1021/bm4008315.

[204] S. Saber-Samandari and M. Gazi, “Pullulan based porous semi-IPN hydrogel: Synthesis, characterization and its application in the removal of mercury from aqueous solution,” *Journal of the Taiwan Institute of Chemical Engineers*, vol. 51, pp. 143–151, Jun. 2015, doi: 10.1016/j.jtice.2015.01.013.

[205] A. Ali and S. Ahmed, “Recent Advances in Edible Polymer Based Hydrogels as a Sustainable Alternative to Conventional Polymers,” *J. Agric. Food Chem.*, vol. 66, no. 27, pp. 6940–6967, Jul. 2018, doi: 10.1021/acs.jafc.8b01052.

[206] Y. Yuan, M. Yin, L. Chen, F. Liu, M. Chen, and F. Zhong, “Effect of calcium ions on the freeze-drying survival of probiotic encapsulated in sodium alginate,” *Food Hydrocolloids*, vol. 130, p. 107668, Sep. 2022, doi: 10.1016/j.foodhyd.2022.107668.

[207] C. Hu, W. Lu, A. Mata, K. Nishinari, and Y. Fang, “Ions-induced gelation of alginate: Mechanisms and applications,” *International Journal of Biological Macromolecules*, vol. 177, pp. 578–588, Apr. 2021, doi: 10.1016/j.ijbiomac.2021.02.086.

[208] P. Gurikov and I. Smirnova, “Non-Conventional Methods for Gelation of Alginate,” *Gels*, vol. 4, no. 1, p. 14, Feb. 2018, doi: 10.3390/gels4010014.

[209] J. Kurowiak, A. Mackiewicz, T. Klekiel, and R. Będziński, “Evaluation of Selected Properties of Sodium Alginate-Based Hydrogel Material—Mechanical Strength, μDIC Analysis and Degradation,” *Materials*, vol. 15, no. 3, p. 1225, Feb. 2022, doi: 10.3390/ma15031225.

[210] A. Mori, T. Kaito, H. Furukawa, M. Yamato, and K. Takahashi, “Birefringence of silica hydrogels prepared under high magnetic fields reinvestigated,” *Mater. Res. Express*, vol. 1, no. 4, p. 045202, Oct. 2014, doi: 10.1088/2053-1591/1/4/045202.

[211] B. Ding *et al.*, “A 2D material–based transparent hydrogel with engineerable interference colours,” *Nat Commun*, vol. 13, no. 1, p. 1212, Mar. 2022, doi: 10.1038/s41467-021-26587-z.

[212] H. Fan *et al.*, “Laser-Inscribed Stress-Induced Birefringence of Sapphire,” *Nanomaterials*, vol. 9, no. 10, p. 1414, Oct. 2019, doi: 10.3390/nano9101414.

[213] H. Shim *et al.*, “Stretchable elastic synaptic transistors for neurologically integrated soft engineering systems,” *Sci. Adv.*, vol. 5, no. 10, p. eaax4961, Oct. 2019, doi: 10.1126/sciadv.aax4961.